AD-A065 924 NEW MEXICO UNIV ALBUQUERQUE BUREAU OF ENGINEERING R--ETC F/G 11/1
HYDRODYNAMIC LUBRICATION WITH WEAR AND ASPERITY CONTACT IN MECH--ETC(U)
JAN 79 A O LEBECK, J L TEALE, R E PIERCE N00014-76-C-0071

UNCLASSIFIED ME-95(79)ONR-414-1 NL

1 OF 2

AD A065924

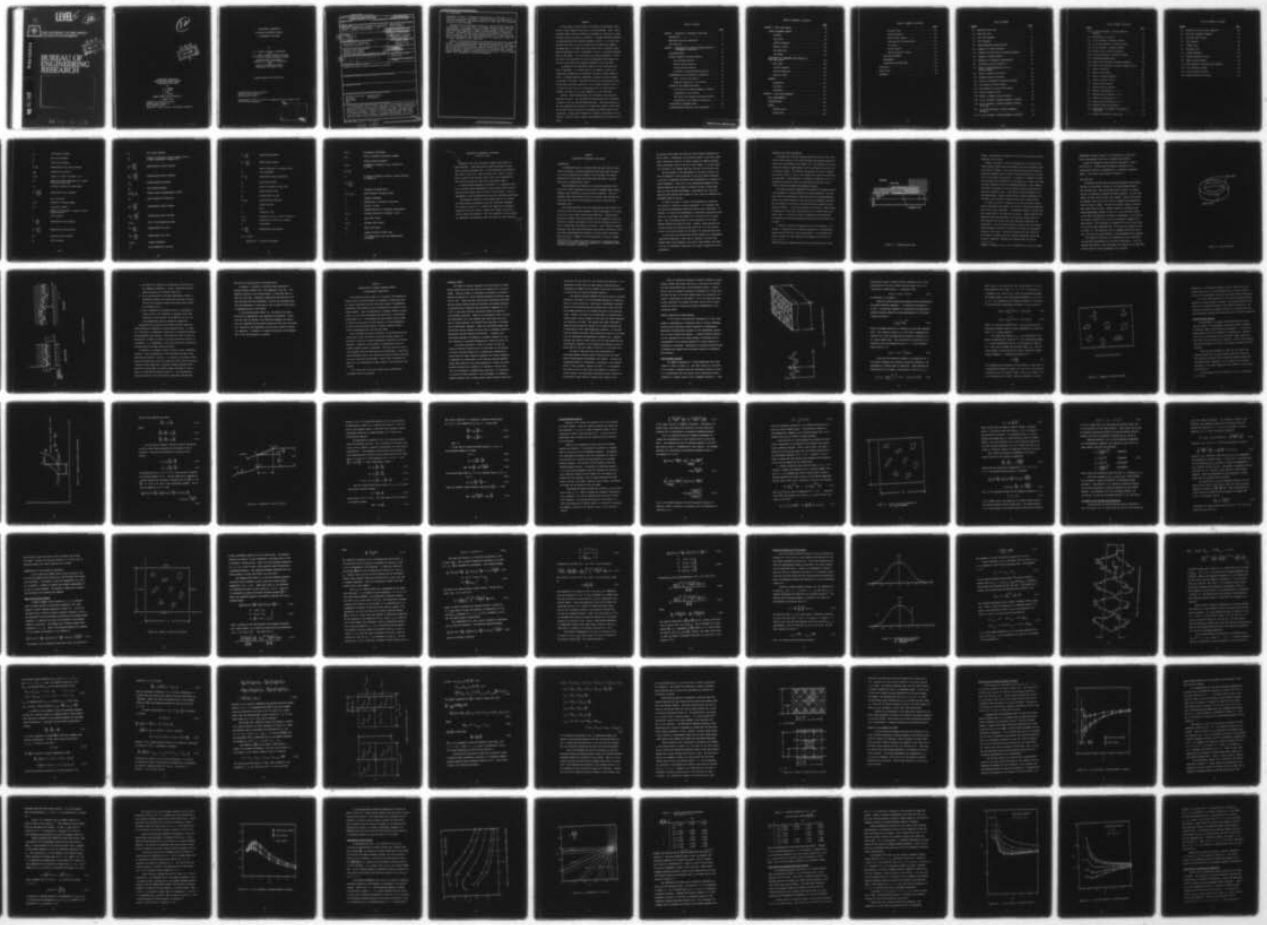

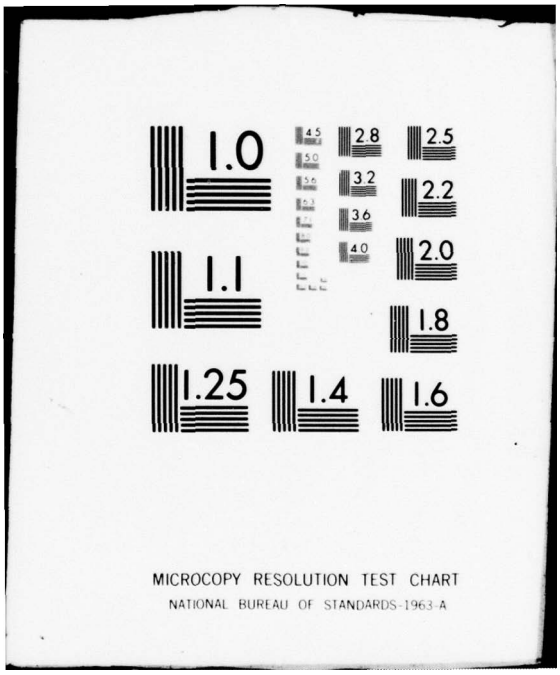
1.0
1.1
1.25
1.4
1.6
1.8
2.0
2.2
2.5
2.8
3.2
3.6
4.0
4.5
5.0
5.6
MICROCOPY RESOLUTION TEST CHART
NATIONAL BUREAU OF STANDARDS-1963-A

LEVEL II

12

THE UNIVERSITY OF NEW MEXICO
COLLEGE OF ENGINEERING

BUREAU OF ENGINEERING RESEARCH

79 03 15 057

(12)

HYDRODYNAMIC LUBRICATION WITH WEAR AND ASPERITY CONTACT IN MECHANICAL FACE SEALS

by

A. O. Lebeck
J. L. Teale,
and
R. E. Pierce

SUMMARY REPORT ME-95(79)ONR-414-1

January 1979

Prepared for the Office of Naval Research under contract no. ONR N 00014-76-C-0071
Approved for public release; distribution unlimited.

HYDRODYNAMIC LUBRICATION

WITH WEAR AND ASPERITY CONTACT

IN MECHANICAL FACE SEALS

by

A. O. Lebeck, Principal Investigator
and
J. L. Teale, Graduate Research Assistant
R. E. Pierce, Graduate Research Assistant

The University of New Mexico
Department of Mechanical Engineering
and
Bureau of Engineering Research
Albuquerque, New Mexico 87131

Summary Report ME-95(79)ONR-414-1

Prepared for the Office of Naval Research under contract no. ONR N 00014-76-C-0071

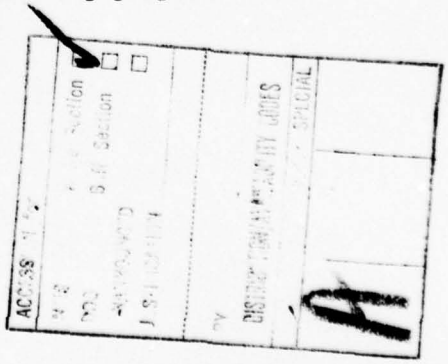

UNRESTRICTED

SECURITY CLASSIFICATION OF THIS PAGE (When Data Entered)

REPORT DOCUMENTATION PAGE

READ INSTRUCTIONS BEFORE COMPLETING FORM

1. REPORT NUMBER (6)

2. GOVT ACCESSION NO.

3. RECIPIENT'S CATALOG NUMBER

4. TITLE (and Subtitle)
HYDRODYNAMIC LUBRICATION WITH WEAR AND ASPERITY CONTACT IN MECHANICAL FACE SEALS

5. TYPE OF REPORT & PERIOD COVERED
SUMMARY REPORT
12/1/77-11/30-78

6. PERFORMING ORG. REPORT NUMBER (14)
ME-95(79)ONR-414-1

7. AUTHOR(s) (10)
A. O. Lebeck
J. L. Teale
R. E. Pierce

8. CONTRACT OR GRANT NUMBER(s) (15)
ONR N00014-76-C-0071

9. PERFORMING ORGANIZATION NAME AND ADDRESS
The University of New Mexico
Albuquerque, New Mexico 87131

10. PROGRAM ELEMENT, PROJECT, TASK AREA & WORK UNIT NUMBERS (12)
190p.

11. CONTROLLING OFFICE NAME AND ADDRESS (11)
Director, Power Program
Department of the Navy
Office of Naval Research, Arlington, Va. 22217

12. REPORT DATE
Jan[illegible]979

13. NUMBER OF PAGES
169

14. MONITORING AGENCY NAME & ADDRESS(if different from Controlling Office) (9)
Summary Rept. 1 Dec 70 - 30 Nov 78,

15. SECURITY CLASS. (of this report)
Unclassified

15a. DECLASSIFICATION/DOWNGRADING SCHEDULE

16. DISTRIBUTION STATEMENT (of this Report)
Approved for public release; distribution unlimited

17. DISTRIBUTION STATEMENT (of the abstract entered in Block 20, if different from Report)

18. SUPPLEMENTARY NOTES

19. KEY WORDS (Continue on reverse side if necessary and identify by block number)

Mechanical Face Seals
Face Seals
Lubrication
Wear
Asperity Contact
Hydrodynamic

20. ABSTRACT (Continue on reverse side if necessary and identify by block number)

In this report a brief review of the theory of hydrodynamic lubrication in wavy contacting face seals is first presented. Then a review of models which predict the effects of roughness on lubrication is made. The work of Patir and Cheng is evaluated. A slightly different approach is developed which gives somewhat different results. It is shown that the shear flow factor ϕ_s may not exist for some practical roughness configurations. It is shown that flow factors take on different values when two-directional flow is

(over)

DD FORM 1 JAN 73 1473 EDITION OF 1 NOV 65 IS OBSOLETE

JOB

SECURITY CLASSIFICATION OF THIS PAGE (When Data Entered)

256 085

20. (continued)

considered. Finally, a truncated roughness model is developed. It is shown that the results published in a previous report are conservative in that the hydrodynamic load support predicted is lower than can be expected according to this new model.

The method for the theoretical design of a wavy contacting face seal is developed. It is shown that at low numbers of waves, seal instability problems may be encountered, whereas at higher numbers of waves, it becomes physically impossible to impose the desired amount of waviness on the seal. The method shows how to optimize seal design with these and other constraints. For the example problem solved, it is shown that wear rate for a hydrodynamic seal can theoretically be reduced by a factor of 17:1 when compared to a flat faced seal.

Finally, a detailed description of a mechanical face seal test apparatus is given. This apparatus has been designed and constructed in order to test the theories mentioned above. The unique features of the test apparatus are the ability to elastically impose a moving wave on the seal ring and the ability to measure the torque acting on the single seal. Speed, water temperature, pressure, and waviness are controlled. Friction torque, leakage, face temperature, and wear are measured.

ABSTRACT

In this report a brief review of the theory of hydrodynamic lubrication in wavy contacting face seals is first presented. Then a review of models which predict the effects of roughness on lubrication is made. The work of Patir and Cheng is evaluated. A slightly different approach is developed which gives somewhat different results. It is shown that the shear flow factor ϕ_s may not exist for some practical roughness configurations. It is shown that flow factors take on different values when two-directional flow is considered. Finally, a truncated roughness model is developed. It is shown that the results published in a previous report are conservative in that the hydrodynamic load support predicted is lower than can be expected according to this new model.

The method for the theoretical design of a wavy contacting face seal is developed. It is shown that at low numbers of waves, seal instability problems may be encountered, whereas at higher numbers of waves, it becomes physically impossible to impose the desired amount of waviness on the seal. The method shows how to optimize seal design within these and other constraints. For the example problem solved, it is shown that wear rate for a hydrodynamic seal can theoretically be reduced by a factor of 17:1 when compared to a flat faced seal.

Finally, a detailed description of a mechanical face seal test apparatus is given. This apparatus has been designed and constructed in order to test the theories mentioned above. The unique features of the test apparatus are the ability to elastically impose a moving wave on the seal ring and the ability to measure the torque acting on the single seal. Speed, water temperature, pressure, and waviness are controlled. Friction torque, leakage, face temperature, and wear are measured.

TABLE OF CONTENTS

TABLE OF CONTENTS (continued)

TABLE OF CONTENTS (concluded)

LIST OF FIGURES

LIST OF FIGURES (continued)

LIST OF FIGURES (concluded)

LIST OF TABLES

LIST OF SYMBOLS

a	amplitude of wave on waviness generating mechanism
$A = \frac{EJ_x}{GJ}$	stiffness ratio
A	area of bearing segment
b_h, $\bar{b}_h$	fraction of seal width subject to fluid pressure
$B = \frac{r_b^2 - r_i^2}{r_o^2 - r_i^2}$	balance ratio for an outside pressurized seal
c	one half maximum roughness height
d	thickness of seal ring
E	Young's modulus
$E( )$	expectancy operator
$f(h_s)$	roughness distribution function
f, f_g	density function
G	shear modulus
h	nominal film thickness
$\bar{h} = \frac{h}{c}$	dimensionless film thickness
$\bar{h}_\sigma = \frac{h}{\sigma}$	dimensionless film thickness
h_d, h_{da_j}, h_{db_j}	film thickness variation due to elastic distortion and Fourier coefficients for same
h_i	total initial waviness amplitude of the nth harmonic
h_{ia_j}, h_{ib_j}	film thickness variation due to initial waviness and wear and Fourier coefficients for same

h_n	nth harmonic waviness
h_o	mean film thickness
H	total film thickness
$\bar{H} = \frac{H}{c}$	dimensionless total film thickness
H_{min}	minimum film thickness
H_1, H_2	height to a point on surface 1 or 2
J_x	moment of inertia equivalent for a curved beam about radial axis
J_θ	torsional constant for curved beam
$\bar{K} = \frac{J_x c^3 E}{r_o^4 r_c^3 \omega\eta}$	dimensionless ring stiffness
ℓ	seal ring width
L_x, L_y	dimension of bearing segment
m,n	correlation lengths
n	number of the harmonic or number of waves around seal face
p	fluid pressure
$\bar{p} = \frac{pc^2}{r_o^2 \omega\eta}$	dimensionless fluid pressure
$\bar{p}_\sigma = \frac{p\sigma^2}{r_o^2 \omega\eta}$	dimensionless fluid pressure
p_b	pressure causing waviness
p_c	cavity pressure

p_i	seal inside pressure
p_m	pressure at asperity contact--equals yield or ultimate compressive strength--F/L^2
$\bar{p}_m = \frac{p_m c^2}{r_o^2 \omega \eta}$	dimensionless contact pressure
$\bar{p}_{m_\sigma} = \frac{p_m \sigma^2}{r_o^2 \omega \eta}$	dimensionless contact pressure
p_{m_a}	average asperity pressure
p_o	seal outside pressure
$\bar{p}_\theta, \bar{p}_{a_j}, \bar{p}_{b_j}$	Fourier series representation of $\bar{p}(\theta)$
p_s	shear strength of asperities
$\bar{p}_s = \frac{p_s c^2}{r_o^2 \omega \eta}$	dimensionless shear strength
$\bar{p}_{s_\sigma} = \frac{p_s \sigma^2}{r_o^2 \omega \eta}$	dimensionless shear strength
q_r, q_θ	flow in two dimensional model
$\bar{q} = \frac{q}{r_o^2 \omega c}$	dimensionless unit flow
$\bar{q}_\sigma = \frac{q}{r_o^2 \omega \sigma}$	dimensionless unit flow
q_x, q_y	leakage components
Q	total leakage for the seal

$\bar{Q} = \frac{Q}{r_o^2 \omega c}$	dimensionless leakage
$\bar{Q}_\sigma = \frac{Q}{r_o^2 \omega \sigma}$	dimensionless leakage
r	radial coordinate or truncation level
$r\theta$	seal coordinates
$\bar{r} = \frac{r}{r_o}$	dimensionless radial coordinate
r_b	seal balance radius
r_c	radius to centroid of seal ring
r_i	inside radius of seal
r_o	cutside radius of seal
R, R_x, R_y	autocorrelation functions
S	surface function
t	time
t_r	truncation level
u,v,w	velocities in the x, y and z direction
U,V,W	velocities of a point on a surface
W	load support
$\bar{W} = \frac{Wc^2}{r_o^4 \omega \eta}$	dimensionless load support
$\bar{W}^* = \pi(1-\bar{r}_i^2) \times [\bar{p}_o B + \bar{p}_i (1-B)]$	required load support

x,y,z	rectangular coordinates
$Z_{i,j}$	array of Gaussian distributed numbers
γ	surface pattern parameter
δ_1,δ_2	roughness of surfaces 1 and 2 relative to h_1 and h_2
$\bar{\delta}_\sigma = \frac{\delta}{\sigma}$	
Δ	a factor to provide a bound on viscous friction or change of
$\bar{\Delta} = \frac{c}{\bar{p}_s r_o}$	
η	viscosity of sealed fluid
$\lambda_x,\lambda_y,\lambda_{0.5}$	delay lengths, 50% delay length
θ	angular coordinate
μ	coefficient of friction on seal face
ρ	density of fluid
σ	standard deviation of Gaussian distribution
σ_1,σ_2	standard deviation of surfaces 1 and 2
ϕ_s	shear flow factor
ϕ_x,ϕ_y	pressure flow factors
Φ_s	shear flow factor
ω	angular velocity of seal ring
-	all symbols with a bar are dimensionless as defined

APPLICATION OF RESEARCH TO THE NEEDS OF THE U.S. NAVY

Mechanical face seals are used in numerous applications in Naval machinery. These applications range from propeller shaft seals to boiler feed pump seals. In such equipment the mechanical seal plays a vital role. When such seals fail, repair is costly both in terms of lost time and direct cost, so any improvement in seal life and reliability would be of significant benefit.

As more advanced equipment is designed, it is sometimes difficult to achieve desired performance in more severe service environments with the present state of the art of seal design. Thus, an improvement in seal technology would serve this important application.

The immediate objective of the research herein is to further the understanding of mechanical face seal lubrication phenomena. The ultimate objective is to develop the capability of designing contacting face seals having a longer life, greater reliability, and for extreme environments. Thus, the objectives of this research are compatible with mechanical face seal needs for Naval machinery.

CHAPTER 1

LUBRICATION IN MECHANICAL FACE SEALS

INTRODUCTION

In applications where a rotating shaft must pass from one fluid region to another, contacting mechanical face seals* play the essential role of minimizing the transfer of fluid between the regions. Applications of face seals range from water pump seals to process pump seals to propeller shaft seals.

The performance and reliability of contacting mechanical face seals are of great importance for any type of equipment where minimal leakage, high reliability, and long life are necessary. Even for equipment where these factors are not so critical, seal failures and short seal life lead to high operating cost due to down time and maintenance cost.

Even though mechanical face seal technology has been steadily improving over the past several decades, further improvement in the state of the art of seal design would be most beneficial. Although seals having an acceptable life and reliability can be designed for many applications, further improvement in seal life and reliability would result in significant cost savings to the user. Also, there are numerous mechanical face seal applications where seal loading, reliability, life, and leakage requirements are difficult to achieve within the present state of the art. Examples of such applications are seals for pumps

*The class of low leakage face seals where there is definite contact and wear of the faces as opposed to hydrostatic or hydrodynamic where a definite clearance is maintained.

for nuclear power plants and seals for large diameter submarine propeller shafts. Additionally, the friction losses in face seals represent a significant fraction of energy consumed for pumping purposes. Within the present state of the art of seal design, it is very difficult to design a low leakage seal that also has a low friction loss.

The main barrier to the advancement of the state of the art is that the mechanics of seal operation are not well enough understood to be able to reasonably anticipate seal performance as a function of design parameters. There are no well established fundamental theoretical bases that can be used to indicate the type of seal design that will give improved performance. Improvements that have been made have been brought about largely by trial and error combined with elementary sealing theories.

In order to be able to predict the performance of contacting face seals as a function of design parameters, it is essential that the lubrication mechanisms between the faces be well understood. At present it is known that hydrodynamic or hydrostatic lubrication plays some role in providing load support for oil seals as well as water seals. But, the precise nature of this lubrication is not known. Several theories have been put forth. However, these theories have not been verified for contacting face seals, and it is not possible as yet to use these theories for the design of contacting face seals.

In this work, the results from further research into hydrodynamic lubrication mechanisms in face seals is reported. Much has been learned about these mechanisms, and there is some promise that effective use of hydrodynamic mechanisms can be made to improve face seal performance.

MECHANICAL FACE SEAL LUBRICATION

The mechanical face seal consists basically of two annular rings which rotate relative to each other and which are pressed together by spring and fluid pressures (see Figure 1-1). The surfaces that rub together are generally manufactured as flat as possible initially so as to minimize leakage. The effective gap between the faces is ideally quite small (order of 1 μm) so that leakage flow across the faces will be quite small. The difficulty in designing a mechanical seal is in maintaining the gap at a very low value while at the same time providing a definite lubricant film between the faces.

The load that must be supported at the faces of a mechanical seal is due primarily to loading caused by the sealed pressure. The unit face load can be expressed as some fraction B of the sealed pressure where B can be made greater or less than unity by geometry selection. The load support at the faces is derived from fluid pressure and mechanical pressure. If the fluid pressure at the faces is large enough to support all of the load, then there will be no contact and no adhesive wear.* If none of the load is supported by fluid pressure, the load must be carried by mechanical contact and the wear rate will be large.

In practice, seals often operate at one of two extremes. At one extreme, a large gap will be created by hydrostatic or hydrodynamic effects and the seal will leak a large amount. At the opposite extreme, the gap will close completely and leakage will be very low.

---

*There may still be abrasive wear even if the surfaces do not touch.

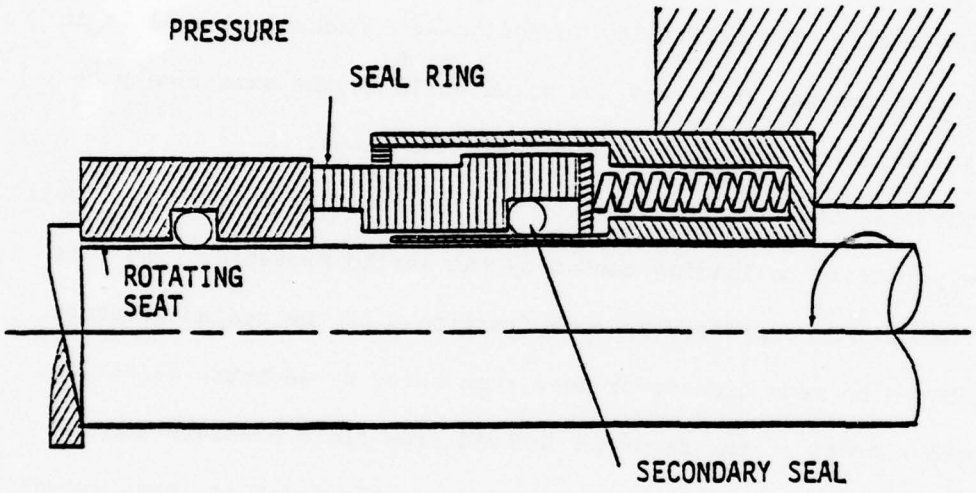

Figure 1-1. Mechanical Face Seal

However, the beneficial lubricant film will be lost,and wear and heat generation will increase.

Based on the above, it can be concluded that an effective seal should operate between these two extremes--having both adequate lubrication and low leakage. To do this requires that any fluid pressure generation mechanism used to provide lift and lubrication to the seal must be very carefully controlled. At present, in commercial contacting face seals this lubrication is left primarily to chance, and often such seals operate at one of the extremes mentioned. Quite commonly such seals will operate in the low leakage condition where wear progresses at a definite rate. Such seals are quite satisfactory for many applications. However, when pressure or speed requirements are increased, then this mode of operation may lead to rapid failure.

In order to be able to design into the seal the proper balance between lubrication and leakage, the origin of lubrication mechanisms must first be fully understood. A considerable amount of research has been accomplished in this area over the years. Various theories have emerged and have been described in the previous annual report [1]*. These theories fall roughly into two categories, hydrostatic and hydrodynamic. In this research program, attention has been directed toward studying the effects of waviness as a source of hydrodynamic pressure in face seals. Particular attention has been focused on the effects of roughness and low viscosity applications where some touching is expected. Waviness was selected among the various

---

*Numbers in brackets refer to List of References at the end of report.

hydrodynamic theories because it is controllable in seals and a better understanding could lead to improved seal designs.

Sources of waviness in seals have been described in detail previously [1]. Waviness may be produced accidentally as an uncontrolled variable or intentionally in a precisely controlled manner. A wavy seal ring is shown in Figure 1-2.

WAVY FACE SEAL

To describe the wavy seal lubricating mechanism in more detail, consider the ring shown in Figure 1-2 as being pressed against a flat rotating ring. Then the problem shown in Figure 1-3 results. The seal is subjected to outside and inside pressure. The wavy face (shown) is fixed, while the flat face rotates. Given the two waves, for example, there will be two points of minimum film thickness between the faces as shown. The seal may actually contact in regions near these points as shown. Angular rotation of the mating face causes hydrodynamic pressure to build up in the converging regions as the point of minimum film thickness is approached. In the diverging regions, cavitation will occur as the pressure attempts to become negative. This cavitation is essential for a net lifting force, and for an outside pressurized seal, the cavity will appear as shown in Figure 1-3. The fluid will flow in streamers across the cavity, and a full film will again develop at the downstream cavity boundary.

The problem to be solved is to determine the fluid and mechanical pressure distributions for the given configuration. Given the pressure distribution, then load support and leakage can be calculated and the effect of various parameters can be studied.

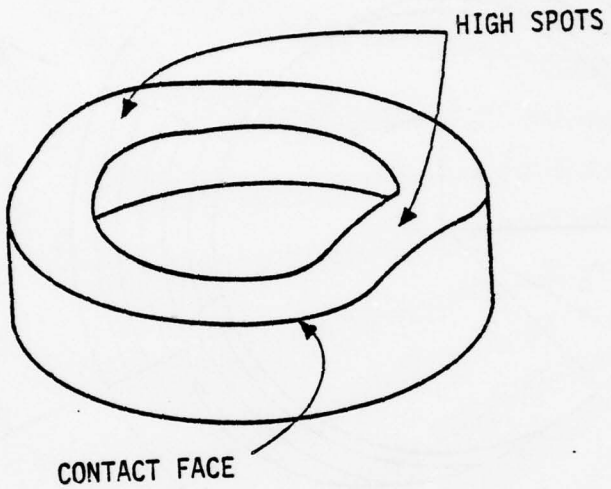

Figure 1-2. Wavy Seal Ring

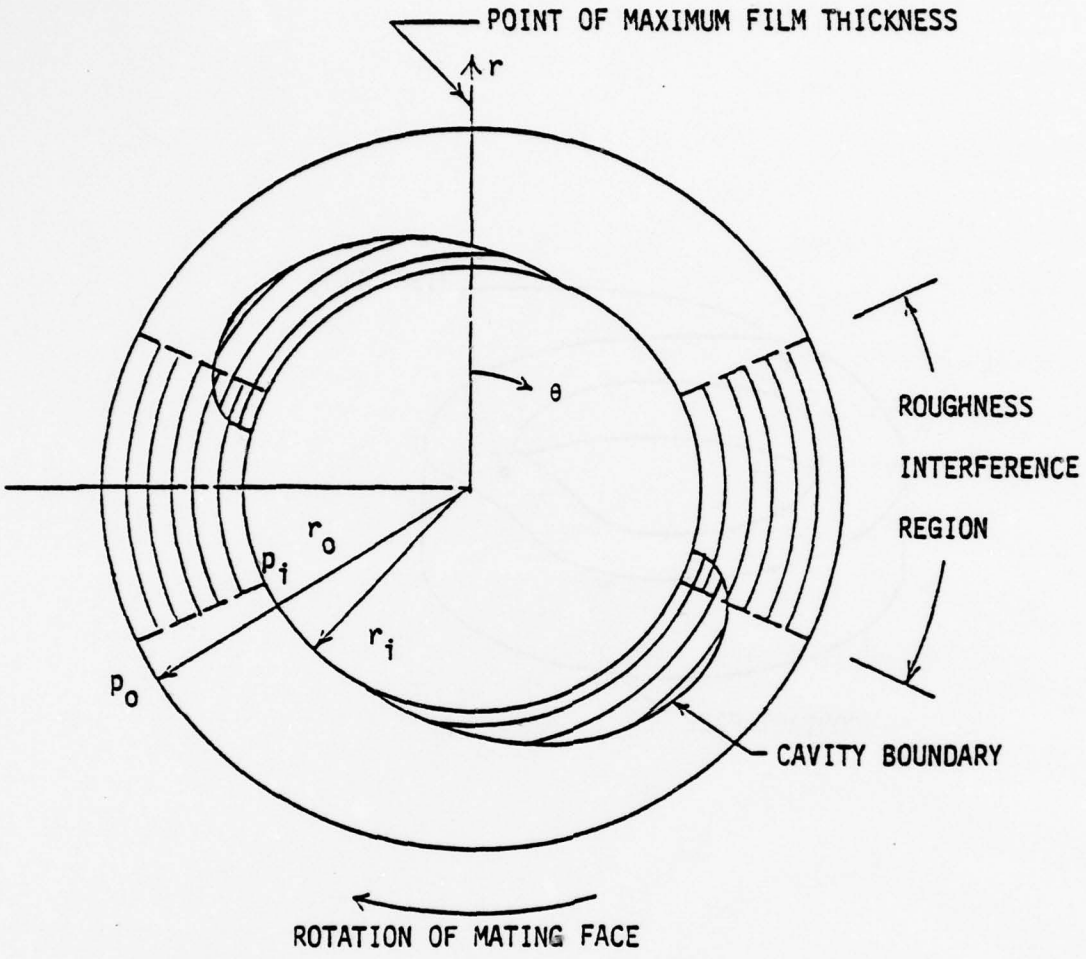

$$h = h_o + h_a \cos n\theta$$

Figure 1-3. Wavy Seal Geometry

The hydrodynamic pressure distribution for this problem has been solved by various methods by Findlay [2], Pape [3], and Stanghan-Batch and Iny [4] for perfectly smooth faces. These results show that even a small waviness produces sufficient load support for complete liftoff. However, heavily loaded or low viscosity seals do not operate with full hydrodynamic load support and complete separation. A definite wear results. Surfaces of such seals contact during operation, and hydrodynamic pressure is affected by interactions with surface roughness (See Figure 1-4). Seals of this type operate in a mixed friction regime. Hydrodynamic load support due to waviness continues to provide a significant fraction of the load support, but asperity contact must provide the balance. Thus these important effects must be included in a wavy seal lubrication model.

In the first annual report for this project, reference [5], the above problem was solved using a one dimensional theory. In the second annual report, [1], the much more complex two dimensional solution to the above problem was solved. The effects of waviness, roughness, asperity contact, wear, cavitation, and elastic deflection were included in the model. Using this model predictions were made for the relative wear rate, friction, and leakage as a function of roughness, waviness, speed, size, pressure, viscosity, and material.

A number of conclusions were reached based on the studies reported in reference [1]. Those having impact on this present work are:

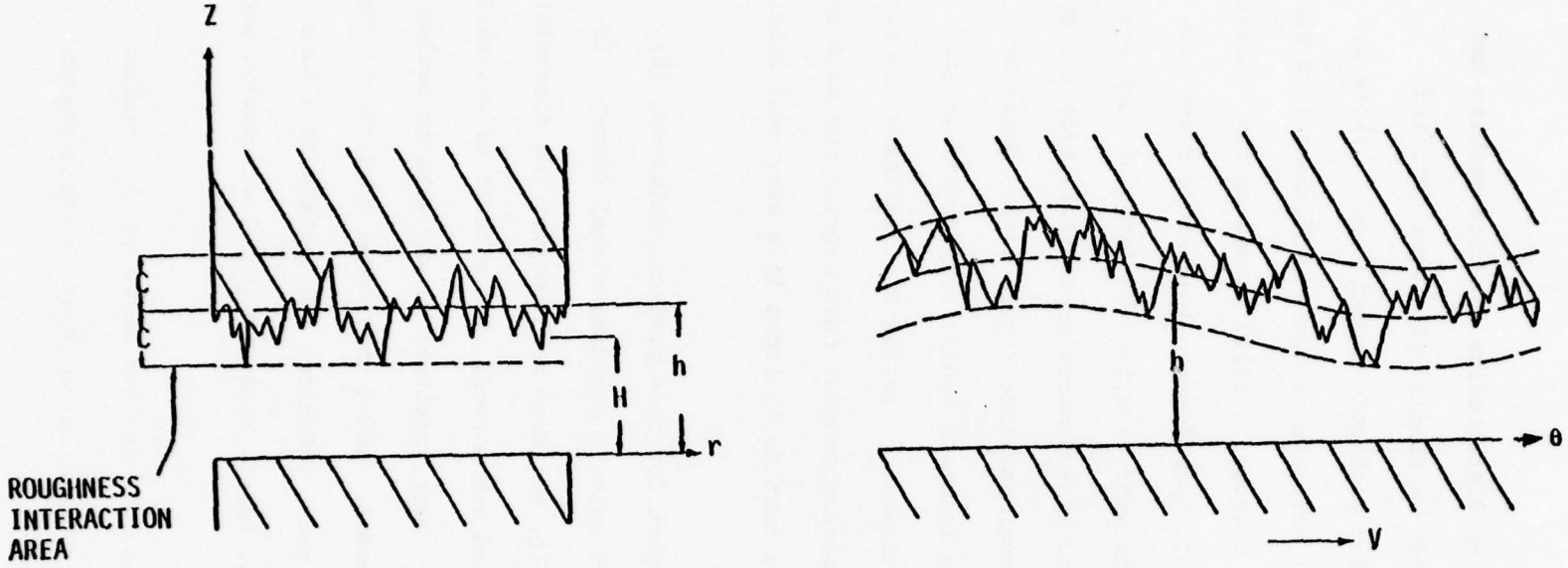

Figure 1-4. Seal Roughness

1) The effects of roughness on hydrodynamic lubrication are not completely understood. Certain fundamental questions remain concerning the rcughness model used.

2) As to the potential of utilizing hydrodynamic effects to advantage by design, the results show that wear rate and friction can be greatly reduced while maintaining leakage at acceptable levels.

3) While a comparison of predicted results to experimental results given in the literature is generally good, data contained in the literature are incomplete, so more complete experimental data are needed for comparison.

The present year's activities have been directed toward providing additional information on these important topics. In Chapter 2 the effect of roughness on lubrication is reviewed and several new developments are presented. This particular topic is being investigated by a number of people, and certain questions have yet to be answered. As a consequence, a seal model based upon a particular roughness model can become suddenly obsolete.

In Chapter 2, an attempt is made to resolve certain fundamental questions. While contributions to the knowledge were made, other questions were raised in doing so. The question of roughness effects remains unsettled and a final seal model must await these conclusions. In spite of this limitation, a different surface roughness interpretation has been made, and results compare favorably in some respects to those from the previous model [1]. The interpretation made also points out the strong need for additional experimental

work which is being pursued as discussed below.

In Chapter 3, attention is directed toward developing a rational design procedure for a wavy mechanical face seal. The parameter studies of the previous report [1] have been used as a basis for this work. Additional studies have been made and a design procedure has been established. Results are presented which show the advantages of a wavy seal as well as some of the pitfalls of implementing such a seal design.

In the previous annual report [1], the design of the main portion of an experimental test apparatus was described. During this past year the design of the auxiliary equipment for the machine was completed and the entire machine has been built and tested out. Mechanical seal experiments are now being carried out using this apparatus. In Chapter 4 a complete description and documentation of the test apparatus is provided.

CHAPTER 2

REEVALUATION OF SURFACE ROUGHNESS EFFECTS IN HYDRODYNAMIC LUBRICATIONS

In the previous annual report [1], discussion was presented indicating that the precise effects of roughness on lubrication were not clearly understood and that the correct method of mathematical treatment of the problem was still developing and a subject of continuing debate. Given the importance of roughness effects on lubrication in a wavy seal configuration as pointed out in the previous annual report [1], it was decided that some attempt should be made to resolve the question as to the validity of various approaches, so that the best available models of surface roughness effects could be incorporated into the wavy seal model.

After reviewing the latest literature, it was decided that the recent work of Patir and Cheng [6] held the greatest promise of providing a useful yet accurate mathematical description of surface roughness. Therefore in this chapter a comprehensive review of surface roughness theory is presented. The Patir Cheng [6] work is then evaluated using the theoretical basis established. Using techniques developed herein, the limitations and uncertainties concerning the Patir Cheng work are developed. Finally some conclusions are made as to the significance of these results on the rough wavy seal problem.

As a first step to place the recent work in perspective, a literature survey is presented.

LITERATURE SURVEY

The effect of surface roughness on the lubrication of hydrodynamic bearings has been the subject of research only in the past decade. Tzeng and Saibel [7] developed the concepts of stochastic modeling as applied to a slider bearing possessing transverse roughness in 1967. During the next several years Christensen and Tonder derived average Reynolds equations governing the expected pressure in bearings having transverse and longitudinal roughness [8], [9]. In all of this work classical lubrication theory was applied to rough surface situations. Based on the experimental work of Ostvik and Christensen [10] it was observed that after some run-in and wear in roller bearings, the surfaces often exhibited a two-dimensional longitudinal roughness. Hence the Christensen-Tonder work was oriented toward surfaces with this type of roughness having an approximate Gaussian frequency distribution. Ultimately the Christensen approach was extended to isotropic surfaces [11] and this treatment is considered mathematically invalid by Elrod [12].

In another publication, Elrod [13] points out that the classical Reynolds equation may not be applicable in the analysis of surface roughness effects due to dimensional considerations. Elrod coined the terms "Reynolds roughness" and "Stokes roughness" to emphasize the restrictions on the classical Reynolds equation. Second order effects of the Stokes equations to account for large surface curvature were included in an analysis by Sun and Chen [14], but the method is mathematically laborious. An alternative to the use of Stokes equations is the development of a modified Reynolds equation which includes rough surface functions explicitly.

Both Elrod [12] and Godet [15] have derived such equations. It is emphasized by Godet that the total surface roughness may not necessarily be lumped onto one surface as was done by Christensen in accord with the classical Reynolds equation.

The special Reynolds equation was used to derive an average equation in the spirit of the Christensen equations by Cheng and Patir [6] and by Elrod [16]. Elrod used a perturbation technique applied to the modified Reynolds equation which solves for both the average pressure and the standard deviation of the pressure value. However, the result is not applicable to bearings where contact occurs, and an estimate of the error for closely approaching surfaces is not made. The average flow model developed by Cheng and Patir allows for contact of the bearing surfaces and is applicable to real three-dimensional surfaces. It was found that the average flow model yields consistent results in the limit with the Christensen two-dimensional roughness work. Gaussian surfaces were used for these results and the autocorrelation and non-isotropic character of the surfaces were imposed by use of a method based on the joint ideas of Peklenik [17] and Patir [18].

The work of Cheng and Patir also discredited the Christensen-Tonder isotropic model by showing that the latter results underestimated hydrodynamic load support. Although the longitudinal model of Christensen is considered a close approximation to real surfaces, research by Lebeck [1] on mechanical face seals points out that since side leakage is prevented in contact regions, the Christensen longitudinal model predicts unrealistically large values of pressure when contact occurs.

While the preferred treatment of surface roughness in hydrodynamic systems when contact may occur is definitely not decided, the Patir Cheng Method does hold considerable promise. However, results from the average flow model are presented as a unique solution and the user is not given warning about the limitations, accuracy or correctness of the method. It will be shown that under certain conditions the average flow model results are not reproducible due solely to subjective physical interpretation of the lubrication model.

REYNOLDS EQUATION FOR ROUGH SURFACES

In this Section the qualitative appearance of a real rough surface is described and a functional form of the film thickness resulting from significant surface roughness is hypothesized. Statistical characteristics relevant to the hydrodynamic lubrication of rough surfaces are defined. A general Reynolds equation for the lubrication of two rough surfaces is developed and the interpretation of the general equation for various bearing configurations is discussed. Techniques for obtaining average values of pressure and leakage from the general equation are presented and discussed.

Film Thickness Function

The general appearance of a three-dimensional real rough surface is shown in Figure 2-1. The total height H of any point on the surface is measured from the arbitrarily placed x-y plane. It is hypothesized that this height can be considered as being composed of a nominal height h and a roughness deviation δ. Then

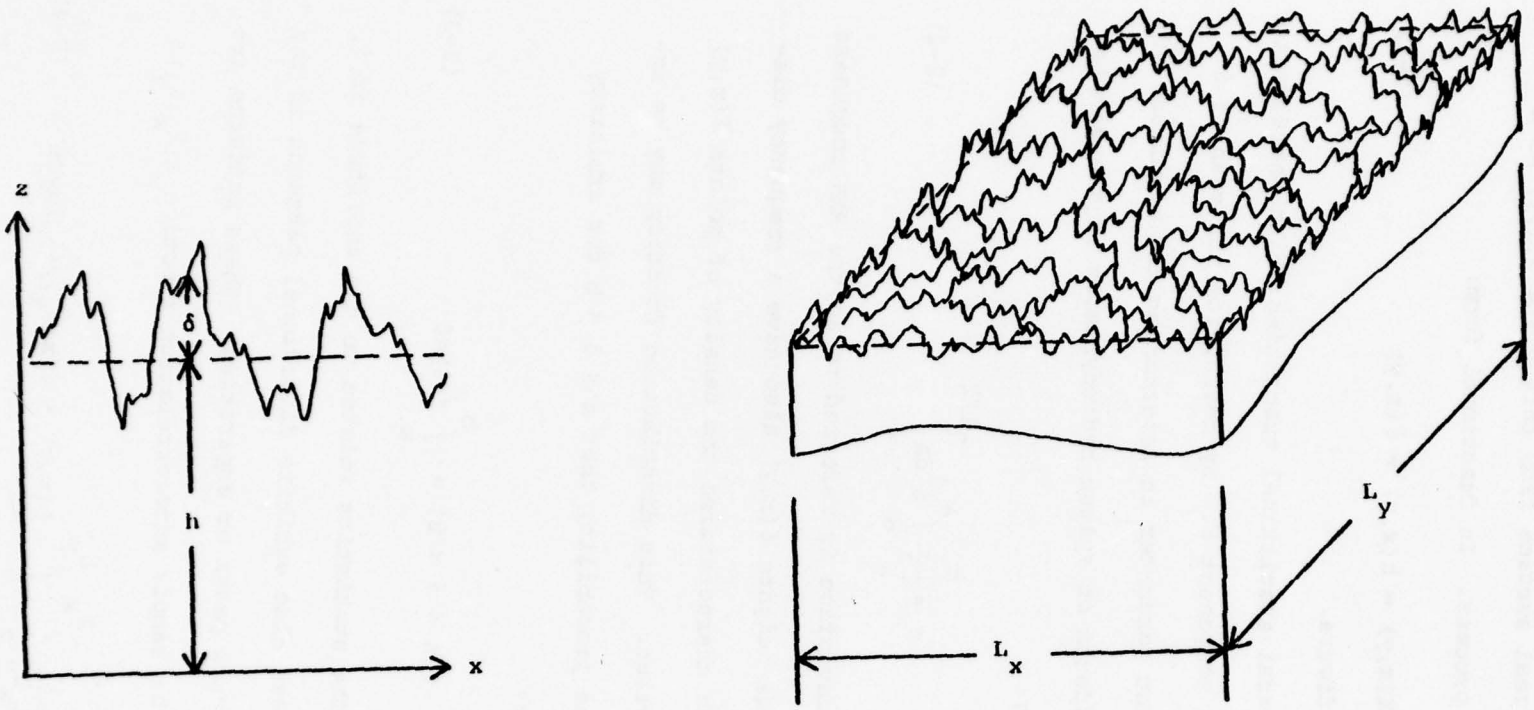

Figure 2-1. Three-Dimensional Rough Surface

there exists a mean x-y plane precisely defined by $h(x,y)$ while the deviation of the real surface from this plane $\delta(x,y)$ is a statistically random process. In functional form:

$$H(x,y) = h(x,y) + \delta(x,y) \tag{2-1}$$

as indicated in the figure.

There are several statistical quantities which characterize the random roughness component δ. By definition the mean of δ is zero. An important parameter in determining the magnitude of surface roughness effects on system hydrodynamics is the sample standard deviation σ:

$$\sigma = \left[\frac{1}{A}\int_{o}^{A}\delta^2 dA\right]^{1/2} \tag{2-2}$$

Often the standard deviation is referred to as the RMS roughness value. The roughness heights $\delta(x,y)$ also have a frequency distribution $f(\delta)$ which characterizes the density of points $\delta(x,y)$ at a given height value. This distribution function may be integrated to give the probability that $a < \delta < b$ for arbitrary height values $a < b$:

$$P[a < \delta < b] = \int_{a}^{b} f(\delta)\,d\delta \tag{2-3}$$

Aside from the statistics related to the amplitude of δ, the surface roughness also exhibits directional patterns in the arrangement of surface peaks or asperities. These patterns are characterized by the sample autocorrelation function $R(\lambda_x,\lambda_y)$:

$$R(\lambda_x,\lambda_y) = \frac{1}{L_x L_y}\int_{o}^{L_x}\int_{o}^{L_y} \delta(x,y)\cdot\delta(x+\lambda_x,y+\lambda_y)\,dydx \tag{2-4}$$

where λ_x and λ_y are called the x and y delay lengths. If δ has been normalized with respect to σ, i.e., if δ is replaced by σ/o in Equation (2-4), then $R(\lambda_x,\lambda_y)$ gives the correlation between the surface heights at any two points separated by λ_x in x and λ_y in y. For experimental and numerical purposes, it is easier to use the profile correlation functions in x and y given by:

$$R_x(\lambda_x) = \frac{1}{L_x}\int_o^{L_x} \delta(x,y) \cdot \delta(x+\lambda_x,y)\,dx \qquad (2\text{-}5)$$

$$R_y(\lambda_y) = \frac{1}{L_y}\int_o^{L_y} \delta(x,y) \cdot \delta(x,y+\lambda_y)\,dy \qquad (2\text{-}6)$$

Again, if δ has been normalized by σ, then R_x and R_y give the correlation between heights at points separated by λ_x along constant y or λ_y along constant x.

For large delay lengths $\lambda_{x \text{ or } y}$, the correlation is expected to approach zero, while at $\lambda = 0$ the correlation becomes 1. At some intermediate value of λ, the correlation drops to 0.5. This value is termed the 50% delay length $\lambda_{0.5}$. The 50% delay lengths in each direction are used to define the surface pattern parameter γ, introduced by Peklenik [17]:

$$\gamma = \frac{\lambda_{0.5x}}{\lambda_{0.5y}} \qquad (2\text{-}7)$$

This parameter may be thought of as the length to width ratio of a representative asperity (Figure 2-2), but this is only partial information about the asperity shape. There are a variety of asperity geometries for a given γ such as rectangular, circular,

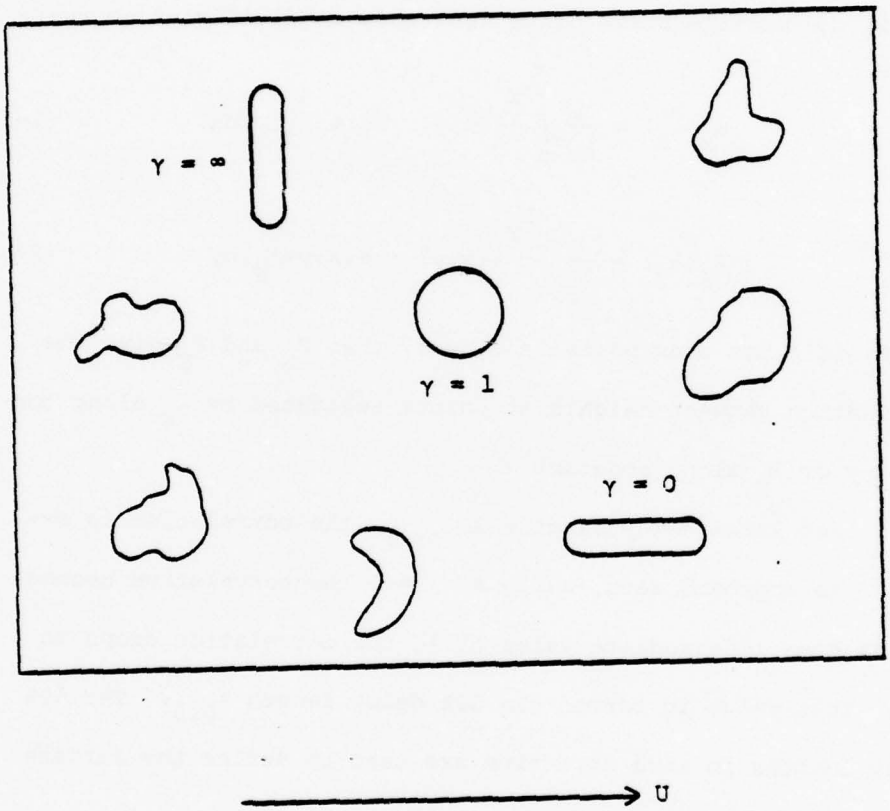

Figure 2-2. Examples of Surface Patterns

diamond, etc. The asperity geometry is also a function of the numerical selection of a finite difference grid, and this selection can alter the hydrodynamic results for the rough surface lubrication.

It is with these statistics in mind that the general Reynolds equation for rough surfaces is derived. The resulting equation must allow the two surfaces involved to have different statistics. The solution for pressure and leakage from any such equations must also have statistical characteristics derivable from the surface statistics.

General Reynolds Equation

The development of a general governing equation for pressure and leakage in a hydrodynamic system where surface roughness is important employs some simplifying assumptions. It is usual to assume laminar flow due to dimensional considerations. Related to this point is the assumed validity of Newton's shear stress law. Body forces and fluid inertia are neglected. Finally, the pressure, viscosity and density are taken to be invariant throughout the film thickness.

Given the above assumptions, Godet [15] has derived the Reynolds equation for two rough surfaces from first principles. This formulation differs from the classical approach because the individual surface roughnesses are not lumped onto one surface. The details of the Godet formulation were reviewed in the previous annual report [1].

For the geometry shown in Figures 2-3 and 2-4, expressions for flow are:

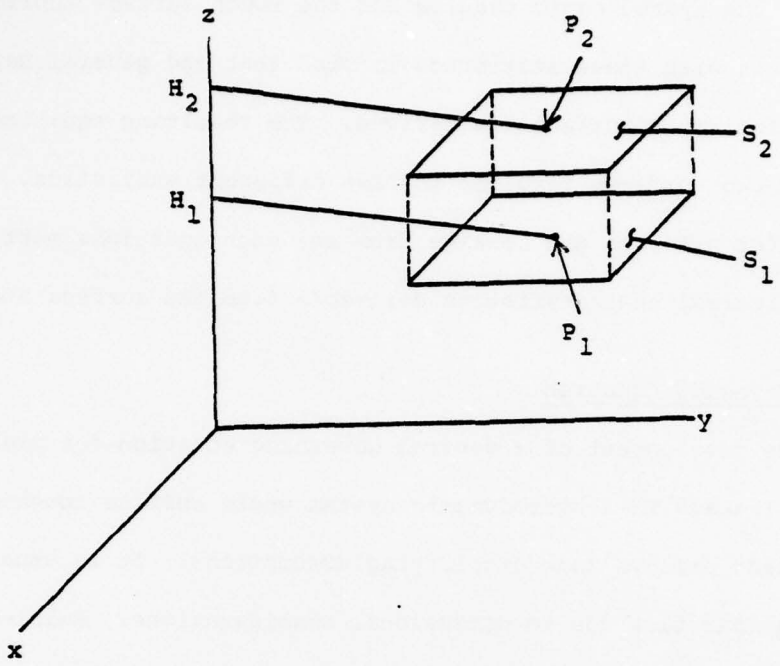

Figure 2-3. Geometry for Derivation of Reynolds Equation

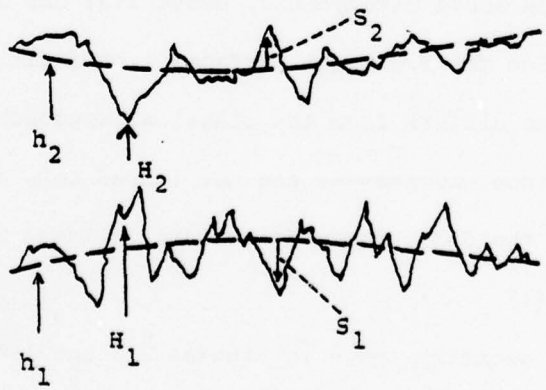

Figure 2-4. Geometry of Rough Surfaces

$$q_x = \frac{\rho}{2}(U_1+U_2)(H_2-H_1) - \frac{\rho}{12\eta}\frac{\partial p}{\partial x}(H_2-H_1)^3 \qquad (2\text{-}8)$$

$$q_y = \frac{\rho}{2}(V_1+V_2)(H_2-H_1) - \frac{\rho}{12\eta}\frac{\partial p}{\partial x}(H_2-H_1)^3 \qquad (2\text{-}9)$$

Assuming density and viscosity are constant, $V_1 = V_2 = 0$ and U_1, U_2 are constant. The final result is

$$\frac{\partial}{\partial x}\left[(H_2-H_1)^3\frac{\partial p}{\partial x}\right] + \frac{\partial}{\partial y}\left[(H_2-H_1)^3\frac{\partial p}{\partial y}\right] = 6\eta(U_1-U_2)\frac{\partial(H_1+H_2)}{\partial x}$$

$$+ 12\eta\left[\left(W_2 - \frac{\partial H_2}{\partial t}\right) - \left(W_1 - \frac{\partial H_1}{\partial t}\right)\right] + 12\eta\frac{\partial}{\partial t}(H_2-H_1) \qquad (2\text{-}10)$$

Because of the appearance of the quantity (H_1+H_2) in (2-10), Godet [15] has pointed out that the Reynolds equation for the rough surfaces agrees with the classical equation only if $H_1 = 0$. This is equivalent to lumping the surface profile H_1 onto H_2 as was done by Christensen, which clearly is not correct if the surfaces have different statistics.

For surfaces having roughness, it has been hypothesized that the total surface height H can be considered as being composed of a nominal height h and a roughness deviation δ. Referring to Figure 2-4, the surfaces S_1 and S_2 are now defined by:

$$H_1 = h_1 - \delta_1 \ , \ H_2 = h_2 + \delta_2 \qquad (2\text{-}11)$$

It is acceptable to lump the nominal film functions:

$$h = h_2 - h_1 \Rightarrow H = H_2 - H_1 = h + \delta_1 + \delta_2 \qquad (2\text{-}12)$$

The time derivatives of H_1,H_2 are evaluated with the aid of Figure 2-5. An Eulerian coordinate transformation is assumed to be

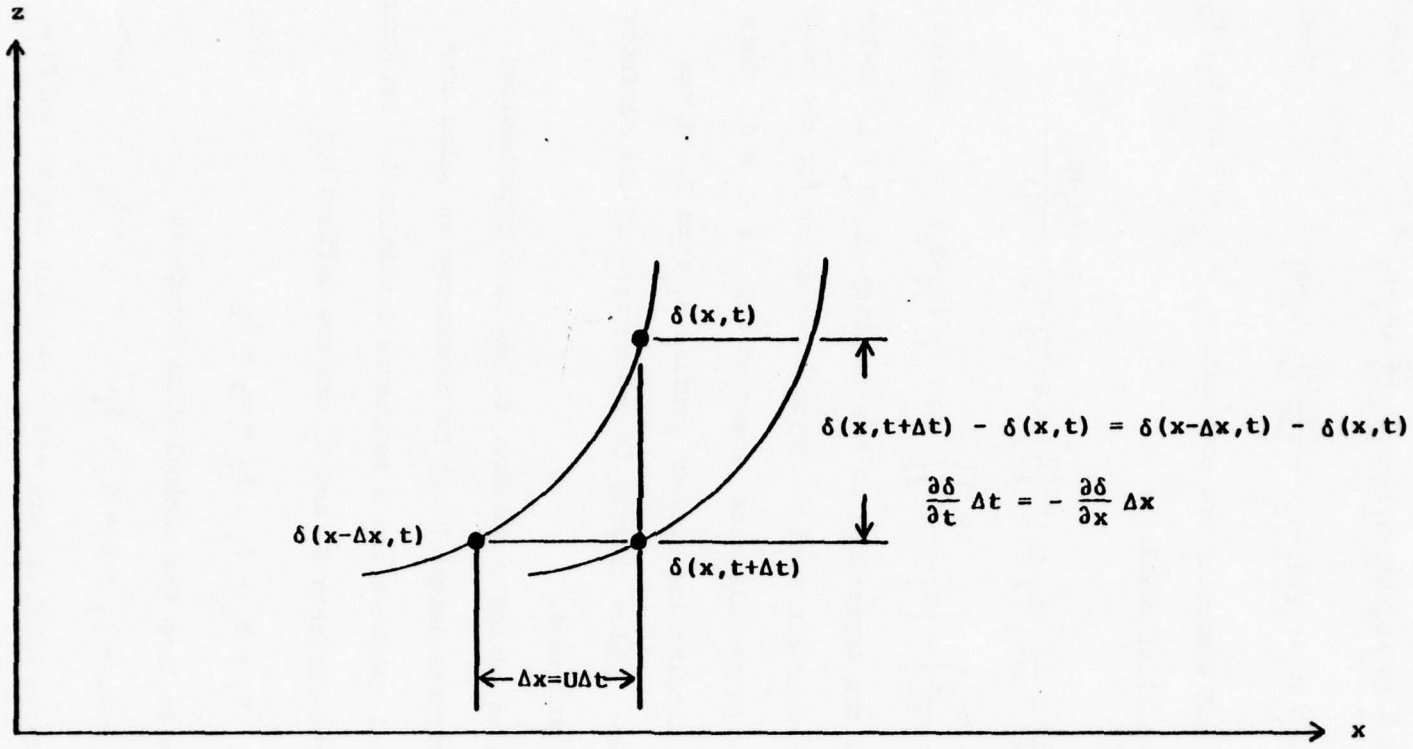

Figure 2-5. Geometry of Coordinate Transformation

valid for the roughness functions:

$$\frac{\partial \delta_i}{\partial t} = -U_i \frac{\partial \delta_i}{\partial x} . \tag{2-13}$$

Hence:

$$\frac{\partial H_1}{\partial t} = \frac{\partial h_1}{\partial t} + U_1 \frac{\partial \delta_1}{\partial x} \tag{2-14}$$

$$\frac{\partial H_2}{\partial t} = \frac{\partial h_2}{\partial t} - U_2 \frac{\partial \delta_2}{\partial x} \tag{2-15}$$

For the case of interest, the point vertical velocities W_1 and W_2 result from the motion of the surfaces in the x-direction. With the aid of Figure 2-6, W_1 and W_2 can be written:

$$W_1 = U_1 \frac{\partial H_1}{\partial x} + \frac{\partial H_1}{\partial t} \tag{2-16}$$

$$W_2 = U_2 \frac{\partial H_2}{\partial x} + \frac{\partial H_2}{\partial t} \tag{2-17}$$

The equations given in (2-11) to (2-17) may be used to simplify the Reynolds Equation (2-10). Without great loss of generality, a steady nominal film thickness is assumed such that $\frac{\partial h_1}{\partial t} = 0$ and $\frac{\partial h_2}{\partial t} = 0$. This is the case in most lubrication systems. The result for Equation (2-10) is then:

$$\frac{\partial}{\partial x}\left[(h+\delta_1+\delta_2)^3 \frac{\partial p}{\partial x}\right] + \frac{\partial}{\partial y}\left[(h+\delta_1+\delta_2)^3 \frac{\partial p}{\partial y}\right] = 6\eta(U_1+U_2) \frac{\partial h}{\partial x} + 6\eta(U_2-U_1) \frac{\partial(\delta_1-\delta_2)}{\partial x} \tag{2-18}$$

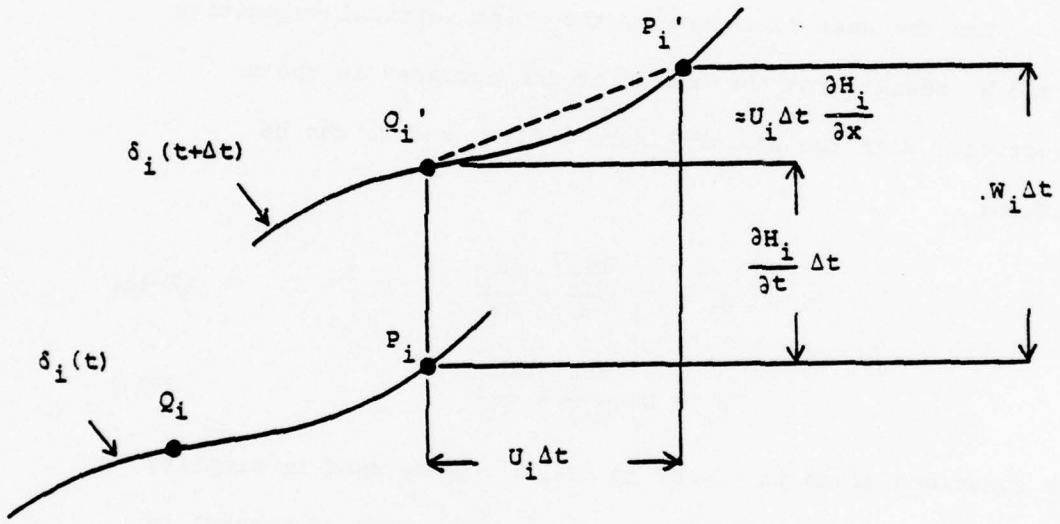

Figure 2-6. Evaluation of Point Velocity W

Equation (2-18) is the Reynolds equation for two rough surfaces as agreed upon by Godet [15], Elrod [12] and Cheng [6]. The last term in this equation makes it clear that the individual surface roughnesses should not be lumped together, as is done in the usual Reynolds equation.

The application of Equation (2-18) to a physical problem should be performed carefully. This is because the vertical velocities W_1 and W_2 require a specific interpretation for each bearing configuration. A few examples of this problem are discussed by first simplifying the vertical velocity expressions given by Equations (2-16) and (2-17) with Equations (2-11) to (2-15). With $\frac{\partial h_1}{\partial t} = 0$ and $\frac{\partial h_2}{\partial t} = 0$, these relationships become:

$$W_1 = U_1 \frac{\partial h_1}{\partial x} + \frac{\partial h_1}{\partial t} \tag{2-19}$$

$$W_2 = U_2 \frac{\partial h_2}{\partial x} + \frac{\partial h_2}{\partial t} \tag{2-20}$$

$$W = W_2 - W_1 = U_2 \frac{\partial h_2}{\partial x} - U_1 \frac{\partial h_1}{\partial x} + \frac{\partial h}{\partial t} \tag{2-21}$$

Now for a case of pure rolling where $U_1 = U_2 = U$, the relative vertical velocity becomes:

$$W = U \frac{\partial h}{\partial x} + \frac{\partial h}{\partial t} \tag{2-22}$$

Using either (2-10) or (2-18), the right hand side of the governing equation becomes:

$$RHS = 12\eta U \frac{\partial h}{\partial x} \tag{2-23}$$

This case is compared to a situation of parallel plates where $U_1 = U_2 = U$, but necessarily $W_1 = W_2 = 0$. In this case:

$$\frac{\partial h_1}{\partial t} = -U_1 \frac{\partial h_1}{\partial x} = 0 \tag{2-24}$$

$$\frac{\partial h_2}{\partial t} = -U_2 \frac{\partial h_2}{\partial x} = 0 \tag{2-25}$$

RHS = 0.

In the case of sliding cylinders where $U_1 = 0$, $U_2 = U$, the governing equation is solved:

$$W_1 = 0 \tag{2-26}$$

$$W_2 = U_2 \frac{\partial h_2}{\partial x} + \frac{\partial h_2}{\partial t} \tag{2-27}$$

$$\text{RHS} = 6\eta U \frac{\partial h}{\partial x} + 6\eta U \frac{\partial (\delta_1 - \delta_2)}{\partial x} \tag{2-28}$$

For sliding plates where $U_1 = 0$, it is required that $W_1 = W_2 = 0$.

$$W_1 = 0 \tag{2-29}$$

$$W_2 = U_2 \frac{\partial h_2}{\partial x} + \frac{\partial h_2}{\partial t} = 0 \tag{2-30}$$

which for constant nominal geometry implies that $\frac{\partial h_1}{\partial x} = 0$. Then

$$\text{RHS} = 6\eta U_2 \frac{\partial (\delta_1 - \delta_2)}{\partial x} + 6\eta U_2 \frac{\partial h_1}{\partial x} \tag{2-31}$$

Average Reynolds Equation

Equation (2-18) governs the pressure of the fluid between two rough surfaces. Since the equation contains the random surface deviation δ, it is not a useful expression unless δ can be eliminated in favor of the statistics of δ. If this can be accomplished, then a solution for the expected value of pressure can be obtained.

There are two techniques by which results for average pressure are obtained. In one method the equation is averaged prior to solution by use of expectancy operators. The expectation expressions containing δ are then interpreted in terms of the statistics of δ and the resulting equation is an average Reynolds equation. The solution of this equation yields the average pressure directly. Alternately the governing equation (2-18) may be solved numerous times for different but statistically identical surfaces and the results for load support and leakage flow are averaged. Both of these techniques have been used in the past, the former largely by Tzeng, Saibel, Christensen and Tonder and the latter by Patir and Cheng.

Christensen and Tonder assumed that surface S_1 has no roughness so that $\delta_1 = 0$. Then by assuming the frequency distribution of δ_2, Equation (2-18) can be averaged directly by use of expectancy operators. The problem encountered in this method is in taking the expectancy of product terms if the terms are correlated. For example, considering the expected value of the y-direction leakage,

$$E\left[-\frac{(h+\delta_1+\delta_2)^3}{12\eta}\frac{\partial p}{\partial y}\right] \neq E\left[-\frac{(h+\delta_1+\delta_2)^3}{12\eta}\right]E\left[\frac{\partial p}{\partial y}\right] \qquad (2\text{-}32)$$

if the terms $(h+\delta_1+\delta_2)^3$ and $\frac{\partial p}{\partial y}$ are correlated. Christensen and Tonder found a way around this difficulty by using simplified surfaces such as longitudinal or transverse roughness patterns.

Now in a preferred direction roughness arrangement the leakage flow perpendicular to that direction does not vary randomly. This assumption allows the Reynolds equation to be averaged term by term in a mathematically valid fashion. The averaged equations for longitudinal and transverse roughness given by Christensen [8, 11] are:

$$\frac{\partial}{\partial x}\left[E(h+\delta_2)^3\frac{\partial E(p)}{\partial x}\right] + \frac{\partial}{\partial y}\left[\frac{1}{E\left(\frac{1}{h+\delta_2}\right)^3}\frac{\partial E(p)}{\partial y}\right] = 6\eta U_2\frac{\partial E(h+\delta_2)}{\partial x} \qquad (2\text{-}33)$$

$$\frac{\partial}{\partial x}\left[\frac{1}{E\left(\frac{1}{h+\delta_2}\right)^3}\frac{\partial E(p)}{\partial x}\right] + \frac{\partial}{\partial y}\left[E(h+\delta_2)^3\frac{\partial E(p)}{\partial y}\right] = 6\eta U_2\frac{\partial}{\partial x}\left[\frac{E\left(\frac{1}{h+\delta_2}\right)^2}{E\left(\frac{1}{h+\delta_2}\right)^3}\right] \qquad (2\text{-}34)$$

E(p) is the average pressure, and the expectancy function of a quantity χ above is defined in conjunction with the frequency distribution f of χ:

$$E(\chi) = \int_{-\infty}^{\infty} (\chi) f(\chi) d\chi \qquad (2\text{-}35)$$

Given the frequency distribution f the expected pressure can be found for these roughness cases. The Christensen approach to three-dimensional roughness is not accepted because both x and y leakage flows are not treated as random variables.

Cheng and Patir [6] have developed the average flow model which is applicable to any generally non-isotropic three-dimensional roughness structure. Much to their credit, the model is practical and the results agree with the limiting cases given by the Christensen Equations (2-33), (2-34). However, it is not clear how Cheng and Patir derived their expected flow expression for $\bar{q}_x$, and the method will be reviewed here.

A control volume with base $\Delta x \Delta y$ and height $H = H_2 - H_1$ is selected to analyze the expected flow in a bearing segment (Figure 2-7). It is assumed that $\Delta x \Delta y$ is large enough to contain numerous asperities but small relative to the bearing dimensions. The unit flow in the x and y directions is given by the averages:

$$\bar{q}_x = \frac{1}{\Delta y} \int_{y}^{y+\Delta y} q_x dy \quad ; \quad \bar{q}_y = \frac{1}{\Delta x} \int_{x}^{x+\Delta x} q_y dx \qquad (2\text{-}36)$$

where q_x and q_y are given by Equations (2-8), (2-9). Cheng and Patir define the pressure flow factors ϕ_x, ϕ_y and the shear flow factor ϕ_s such that

$$\bar{q}_x = \frac{\rho}{2} (U_1+U_2) \overline{(H_2-H_1)} - \rho \phi_x \frac{h^3}{12\eta} \frac{\partial \bar{p}}{\partial x} + \frac{\rho}{2} (U_1-U_2) \sigma \phi_s \qquad (2\text{-}37)$$

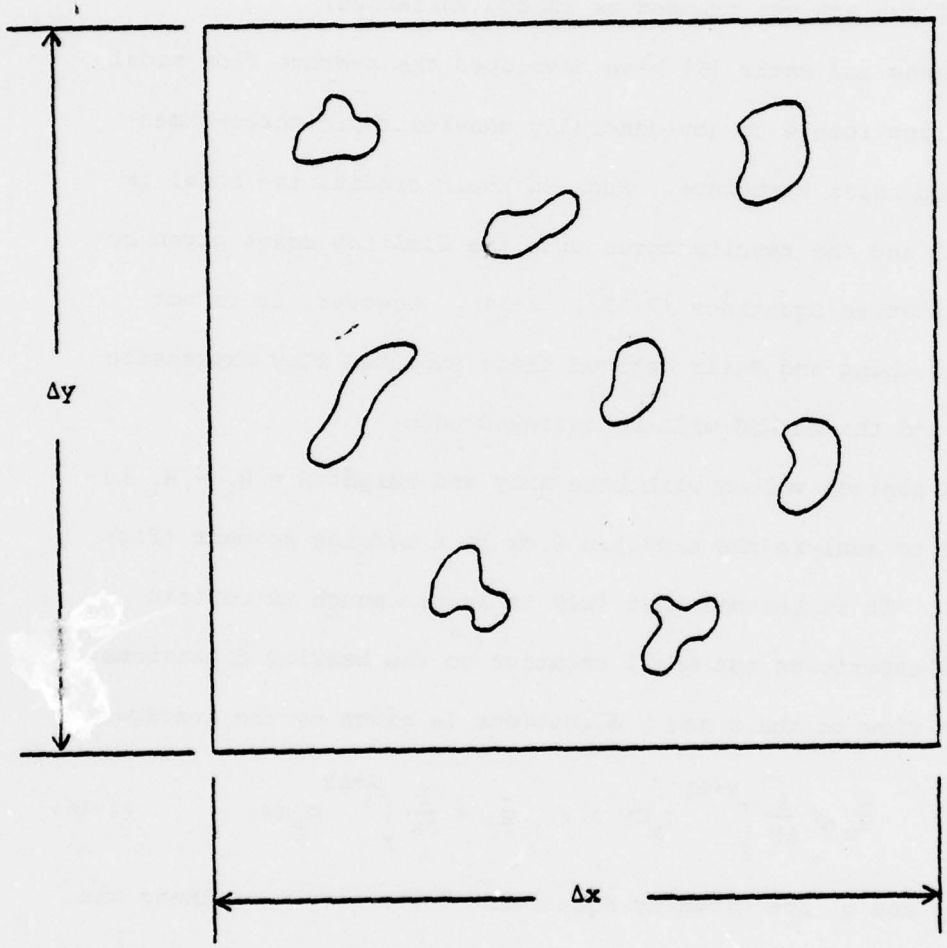

Figure 2-7. Model to Analyze Expected Flow in a Bearing Segment

$$\bar{q}_y = -\rho\phi_y \frac{h^3}{12\eta} \frac{\partial \bar{p}}{\partial y} \tag{2-38}$$

where the bars over the symbols indicate average or expected values. It should be noted that $E(H_2-H_1) = E(H) \neq h$ because of the possibility of contact. As presented by Patir, ϕ_x and ϕ_y compare the average flow in a rough bearing to that of a smooth bearing. The term containing the ϕ_s factor does not seem to result from rigorous evaluation of (2-36), rather this term is included to intuitively account for additional flow due to sliding.

Next a mean flow balance is performed on the control volume resulting in the continuity expression:

$$\frac{\partial \bar{q}_x}{\partial x} + \frac{\partial \bar{q}_y}{\partial y} = -\rho \frac{\partial (\overline{H_2-H_1})}{\partial t} \tag{2-39}$$

Substituting the average flow expressions (2-37), (2-38) into (2-39), the average Reynolds equation is obtained:

$$\frac{\partial}{\partial x}\left[\phi_x h^3 \frac{\partial \bar{p}}{\partial x}\right] + \frac{\partial}{\partial y}\left[\phi_y h^3 \frac{\partial \bar{p}}{\partial y}\right] = 6\eta(U_1+U_2) \frac{\partial (\overline{H_2-H_1})}{\partial x}$$

$$+ 6\eta(U_1-U_2)\sigma \frac{\partial \phi_s}{\partial x} + 12\eta \frac{\partial (\overline{H_2-H_1})}{\partial t} \tag{2-40}$$

Now σ is the standard deviation of the combined roughness $\delta_1 + \delta_2$:

$$\sigma^2 = \sigma_1^2 + \sigma_2^2 \tag{2-41}$$

As h/σ becomes large, the probability of contact becomes minimal and surface roughness effects become small. This means Equation (2-40) should reduce to the smooth bearing equation which requires:

$$\phi_x, \phi y \to 1, \quad \phi_s \to 0 \quad \text{as} \quad \frac{h}{\sigma} \to \infty \tag{2-42}$$

As will be shown later, the flow factors as defined depend only on the statistics of the rough surfaces. These factors are solved by generating artificial surfaces to solve the general Reynolds equation and then by averaging the results for ϕ_x, ϕ_y and ϕ_s.

Comparing Equation (2-40) to the Christensen expressions for two-dimensional roughness, the limits on ϕ_x and ϕ_y for extreme surface conditions are predicted:

$$\phi_x = \left[E\left(\frac{1}{H^3}\right) h^3 \right]^{-1} \qquad \text{Transverse}$$

$$\phi_y = E(H^3)/h^3 \qquad \text{Transverse} \tag{2-43}$$

$$\phi_x = E(H^3)/h^3 \qquad \text{Longitudinal}$$

$$\phi_y = \left[E\left(\frac{1}{H^3}\right) h^3 \right]^{-1} \qquad \text{Longitudinal}$$

These limits were verified by Cheng and Patir [6], assuming $U_1 = U_2$.

Given the evaluation of ϕ_x, ϕ_y and ϕ_s for a given nominal film thickness h, height distribution f and surface pattern parameter γ, then Equation (2-40) governs the expected pressure and is widely applicable to bearing problems with real surface geometry. The advantages over the Christensen approach are significant, so that the Christensen approach is not used herein.

Discussion of the Average Reynolds Equation

When obtaining the average Reynolds equation proposed by Patir and Cheng (2-40), it was pointed out that the term containing

ϕ_s was not rigorously defined. In an attempt to define ϕ_s more precisely, the assumptions made by Patir and Cheng about the average flow Equations (2-37, 2-38) may be restated. Writing Equation (2-36) in terms of expectancy operators:

$$\bar{q}_x = E(q_x) = \frac{\rho}{2}(U_1+U_2)E(H_2-H_1) - E\left[\frac{\rho(H_2-H_1)^3}{12\eta}\frac{\partial p}{\partial x}\right] \qquad (2\text{-}44)$$

Comparing (2-44) and (2-37), the following hypothesis results:

$$E\left[-\frac{(H_2-H_1)^3}{12\eta}\frac{\partial p}{\partial x}\right] = -\phi_x\frac{h^3}{12\eta}\frac{\partial \bar{p}}{\partial x} + \frac{1}{2}(U_1-U_2)\sigma\phi_s \qquad (2\text{-}45)$$

Equation (2-45) implicitly states that ϕ_x and ϕ_s are independent. This assumption is checked later. In this form it is evident that the term containing ϕ_s is included to relieve the dependence of ϕ_x on relative velocity (U_1-U_2). The problem of expanding the left hand side of (2-45) has been a major barrier to rough surface analysis. Hence the significance of this hypothesis is fundamental, and its validity must be verified.

The derivative of ϕ_s can be expressed explicitly for the case of pure sliding $(U_1=-U_2=-\frac{1}{2}U_s)$ where the nominal pressure gradients are made zero $\left(\frac{\partial \bar{p}}{\partial x} = \frac{\partial \bar{p}}{\partial y} = 0\right)$. Using these simplifications to write the general Reynolds equation in average form (2-18) the following results:

$$\frac{\partial \phi_s}{\partial x} = \frac{1}{\sigma}\frac{\partial E(\delta_1-\delta_2)}{\partial x} \qquad (2\text{-}46)$$

Alternately the average equation given by Patir (2-40) may be reduced using the same case:

$$\frac{\partial \phi_s}{\partial x} = \frac{2}{U_s \sigma} \frac{\partial E(H_2 - H_1)}{\partial t} \qquad (2\text{-}47)$$

Equations (2-46) and (2-47) are mathematically equivalent assuming that $\frac{\partial \delta}{\partial t} = -U \frac{\partial \delta}{\partial x}$ holds.

Assuming that ϕ_s is independent as stated above, some insight into the significance of ϕ_s in relation to surface roughness may be obtained by closely examining Equation (2-46). It may be assumed that the roughness functions are truncated by asperity shear so that $E(\delta_1) \neq 0$ and $E(\delta_2) \neq 0$, assuming also that elastic deformation is negligible. If both surfaces are moving, the surface statistics are constant because it is expected that δ_1 and δ_2 will change only very slowly in time with wear. Hence $E(\delta_1)$ and $E(\delta_2)$ are constant, meaning that $\frac{\partial \phi_s}{\partial x} = 0$. Then the only term on the right hand side of the average Reynolds equation that has significance is $\frac{\partial h}{\partial x}$.

In the Patir-Cheng work, a different assumption appears to have been made. It appears that asperities are allowed to spring back after passing through contact. Thus the essential relationship $\frac{\partial \delta}{\partial t} = -U \frac{\partial \delta}{\partial x}$ would not be correct because of an additional $\delta(t)$ due to elastic deformation. The statistics of δ_1 and δ_2 also become unclear. For two moving surfaces $\frac{\partial \phi_s}{\partial x}$ may exist rather than become zero as in the case above. Clearly, more work needs to be done on this aspect of the problem.

Assuming the truncation model above, some of the physical implications may be illustrated by considering a few examples.

In the case of two rotating cylinders, one would expect that the roughness functions would take on fixed characteristics which would change only slowly with the progression of wear as above. Hence the term $E(\delta_1-\delta_2)$ is constant with x and the average equation for this case becomes:

$$\frac{\partial}{\partial x}\left[\phi_x h^3 E\left(\frac{\partial p}{\partial x}\right)\right] + \frac{\partial}{\partial y}\left[\phi_y h^3 E\left(\frac{\partial p}{\partial y}\right)\right] = 6\eta(U_1+U_2)\ \frac{\partial h}{\partial x} \qquad (2\text{-}48)$$

This case is compared to the case of two parallel plates both of which are moving. The nominal film thickness h is constant and the vertical velocities W_1, W_2 are zero. Then the average equation becomes

$$\frac{\partial}{\partial x}\left[\phi_x h^3 E\left(\frac{\partial p}{\partial x}\right)\right] + \frac{\partial}{\partial y}\left[\phi_y h^3 E\left(\frac{\partial p}{\partial y}\right)\right] = 0 \qquad (2\text{-}49)$$

Considering the case of one rotating and one fixed cylinder, it is physically reasonable to assume that the moving surface must take on fixed roughness characteristics. The fixed surface may have $E(\delta_1) = f(h)$, but not a function of time, if $U_1 = 0$. Hence the average equation becomes:

$$\frac{\partial}{\partial x}\left[\phi_x h^3 E\left(\frac{\partial p}{\partial x}\right)\right] + \frac{\partial}{\partial y}\left[\phi_y h^3 E\left(\frac{\partial p}{\partial y}\right)\right] = 6\eta U_2\ \frac{\partial h}{\partial x} + 6\eta U_2\ \frac{\partial E(\delta_1)}{\partial x} \qquad (2\text{-}50)$$

The basic debate which is highlighted in this discussion concerns the physical existence of ϕ_s. It has been argued that for some cases $\frac{\partial \phi_s}{\partial x}$ is zero and hence it should not appear in the average Reynolds equation. However, it does seem that ϕ_s is a necessary term for evaluating flow in a bearing segment. From

these results, great care must be used in applying the average flow model. Certainly the precise character of δ_1 and δ_2 must be understood before the correct equation can be chosen.

DETERMINATION OF FLOW FACTORS BY SIMULATION

In this section the models used by Patir and Cheng [6,18] to solve the pressure flow factors ϕ_x, ϕ_y and the shear flow factor ϕ_s are reviewed. A procedure to test the independence of ϕ_x and ϕ_s is detailed. A model for testing the boundary independence of ϕ_x and ϕ_y is also proposed. Two methods to numerically simulate the flow models are discussed and compared.

Model to Solve Flow Factors

A bearing segment having dimensions $L_x \times L_y$ is selected which is small relative to the bearing dimensions, yet large enough to contain numerous asperities (Figure 2-8). As will be described later, artificial surface roughness functions δ_1 and δ_2 are generated with known frequency distribution and surface pattern parameter γ to describe the total film thickness in the bearing segment at each point. The segment has a constant nominal film thickness $h = h_2 - h_1$. Hence, the governing equation for pressure in this segment from Equation (2-18) appears as:

$$\frac{\partial}{\partial x}\left[(h+\delta_1+\delta_2)^3 \frac{\partial p}{\partial x}\right] + \frac{\partial}{\partial y}\left[(h+\delta_1+\delta_2)^3 \frac{\partial p}{\partial y}\right] = 6\eta(U_2-U_1) \frac{\partial(\delta_1-\delta_2)}{\partial x} . \quad (2\text{-}51)$$

This equation can be formulated numerically given the selection of

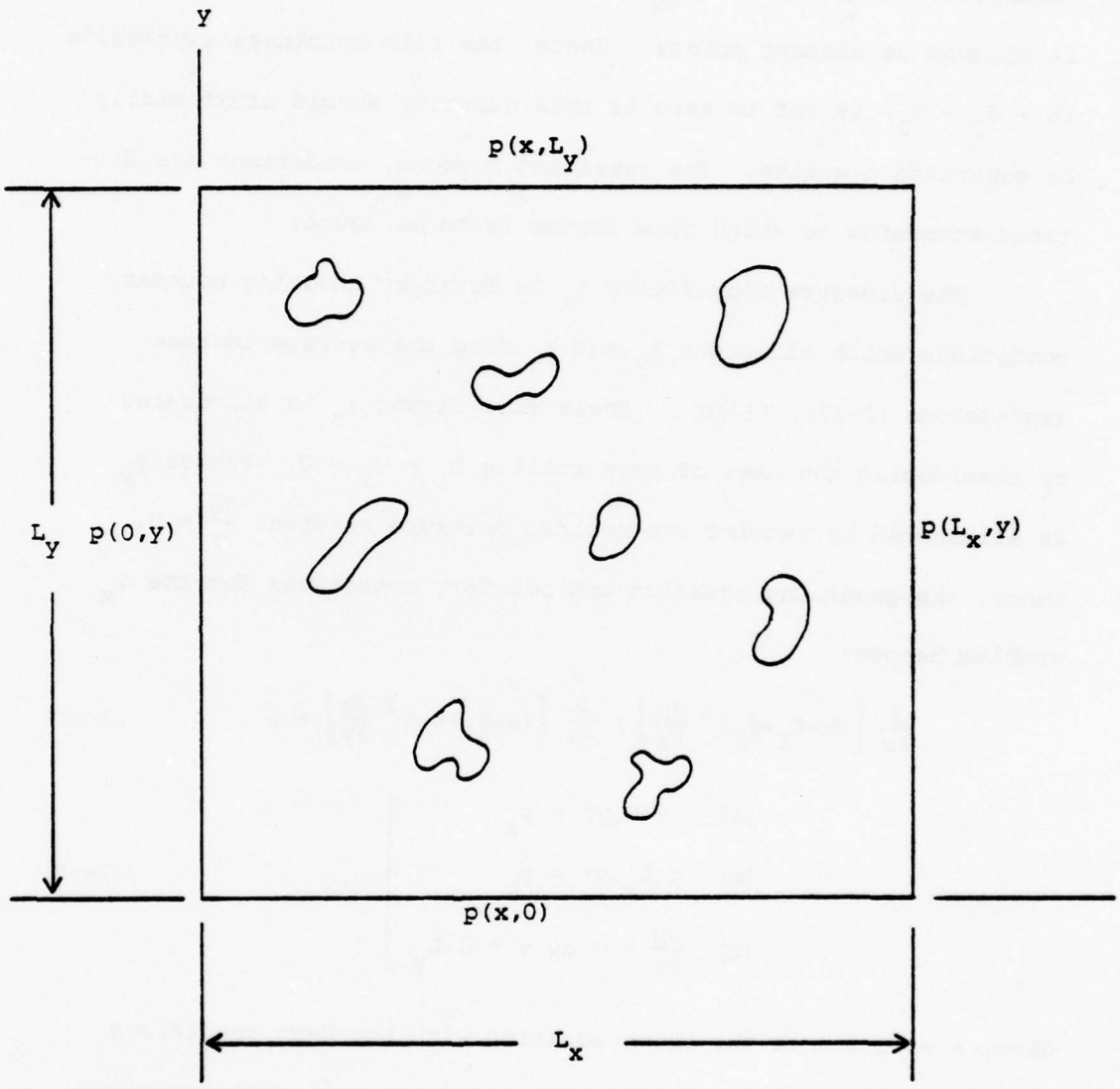

Figure 2-8. Model to Analyze Flow Factors

a finite difference network as will be shown later. One boundary condition is implicit in this formulation, that being that no flow is allowed at contact points. Hence, the film thickness expression $(h + \delta_1 + \delta_2)$ is set to zero if this quantity should artificially be generated negative. The remaining boundary conditions are dictated according to which flow factor is to be found.

The pressure flow factor ϕ_x is found by choosing boundary conditions which eliminate ϕ_y and ϕ_s from the average leakage expressions (2-37), (2-38). Shear flow factor ϕ_s is eliminated by considering the case of pure rolling $U_1 = U_2 = U$. Factor ϕ_y is eliminated by setting the nominal pressure gradient $\frac{\partial \bar{p}}{\partial y} = 0$. Hence, the governing equation and boundary conditions for the ϕ_x problem become:

$$\frac{\partial}{\partial x}\left[(h+\delta_1+\delta_2)^3 \frac{\partial p}{\partial x}\right] + \frac{\partial}{\partial y}\left[(h+\delta_1+\delta_2)^3 \frac{\partial p}{\partial y}\right] = 0 \ . \qquad (2\text{-}52)$$

$$\left.\begin{array}{ll} \text{(a)} & p(0,y) = p_a \\ \text{(b)} & p(L_x,y) = p_b \\ \text{(c)} & \frac{\partial p}{\partial y} = 0 \text{ at } y = 0, L_y \end{array}\right\} \ . \qquad (2\text{-}53)$$

Given a solution to the above equation with boundary conditions for a given surface, ϕ_x is found by eliminating $\bar{q}_x$ from Equations (2-8), (2-37) and (2-38). The result for ϕ_x:

$$\phi_x = \frac{E\left[\frac{-(h+\delta_1+\delta_2)^3}{12\eta} \frac{\partial p}{\partial x}\right]}{\frac{-h^3}{12\eta} \frac{\partial \bar{p}}{\partial x}} = \frac{\frac{-1}{L_y}\int_0^{L_y} \frac{(h+\delta_1+\delta_2)^3}{12\eta} \frac{\partial p}{\partial x}\, dy}{\frac{-h^3}{12\eta} \frac{\partial \bar{p}}{\partial x}} \ , \qquad (2\text{-}54)$$

where:

$$\frac{\partial \bar{p}}{\partial x} = \frac{p_b - p_a}{L_x} \quad . \tag{2-55}$$

The numerator of Equation (2-54) is evaluated from the solution to (2-52) and only one line integral is necessary to find $E(q_x)$ since y flow is suppressed at the boundaries. It should be noted that the gradient $\frac{\partial \bar{p}}{\partial y}$ could also be made zero by using $p(x,0) = p(x,L_y) = p_c$. However, Patir did not use this condition and the difference between these boundary conditions indicates that ϕ_x and ϕ_y may have a boundary dependence. This can be checked by a model to be described later in this chapter.

Since ϕ_x is a random variable as a consequence of the roughness functions, it is necessary to solve Equations (2-52)-(2-54) several times using different, but statistically identical surfaces. The value of ϕ_x is then taken to be $E(\phi_x)$, and statistical inference concerning the range of ϕ_x can be made. It is observed that ϕ_x is independent of velocity U since this factor does not appear in the formulation, and that the value of the nominal pressure gradient $\frac{\partial \bar{p}}{\partial x}$ is also not a factor since the pressure is effectively normalized by this quantity in the expression for ϕ_x. Hence, ϕ_x is a function only of the nominal film thickness h and the roughness statistics. Also, since the quantity $(\delta_1 - \delta_2)$ is eliminated from the governing equation, only one surface is required so that $\phi_x = \phi_x(h/\sigma,\gamma)$. Finally, it is noted that since the method of solving ϕ_y would be identical to that for ϕ_x, it is unnecessary to solve ϕ_y. The difference here is that y-flow sees a different surface pattern than ϕ_x:

$$\phi_y(h/\sigma,\gamma) = \phi_x(h/\sigma,1/\gamma) \quad . \tag{2-56}$$

The shear flow factor ϕ_s is solved by eliminating ϕ_x and ϕ_y from (2-40). The ϕ_s term is retained by selecting $U_1 \neq U_2$ and $U_1 = -U_2 = \frac{U_s}{2}$ is selected for convenience. This problem becomes:

$$\frac{\partial}{\partial x}\left(h+\delta_1+\delta_2\right)^3 \frac{\partial p}{\partial x} + \frac{\partial}{\partial y}\left(h+\delta_1+\delta_2\right)^3 \frac{\partial p}{\partial y} = 6\eta\, U_s \frac{\partial(\delta_1-\delta_2)}{\partial x} \quad . \tag{2-57}$$

$$\left.\begin{aligned} &\text{(a)}\quad p(0,y) = p(L_x,y) = p_a \\ &\text{(b)}\quad \left.\frac{\partial p}{\partial y}\right|_{y=0,L_y} = 0 \end{aligned}\right\}, \tag{2-58}$$

and there is no flow allowed at contact points. Solving for ϕ_s from (2-8), (2-37) and (2-38):

$$\phi_s = \frac{2}{U_s \sigma L_x L_y} \int_0^{L_x} \int_0^{L_y} \frac{-\left(h+\delta_1+\delta_2\right)^3}{12\eta} \frac{\partial p}{\partial x}\, dy\, dx \quad . \tag{2-59}$$

Again, ϕ_s must be averaged over several solutions to obtain $\bar{\phi}_s$. It is seen from (2-57) that the pressure is proportional to $\eta\, U_s$, and hence, ϕ_s depends on h, γ_1, γ_2, σ_1 and σ_2 assuming δ_1 and δ_2 have the same frequency distributions.

The independence of ϕ_x and ϕ_s may be checked by eliminating only ϕ_y from the simulation. The governing equation becomes:

$$\frac{\partial}{\partial x}\left[\left(h+\delta_1+\delta_2\right)^3 \frac{\partial p}{\partial x}\right] + \frac{\partial}{\partial y}\left[\left(h+\delta_1+\delta_2\right)^3 \frac{\partial p}{\partial y}\right] = 6\eta(U_2-U_1) \frac{\partial(\delta_1-\delta_2)}{\partial x} \quad . \tag{2-60}$$

subject to boundary conditions:

$$\left.\begin{aligned} &\text{(a)} \quad p(0,y) = p_a \\ &\text{(b)} \quad p(L_x,y) = p_b \\ &\text{(c)} \quad \left.\frac{\partial p}{\partial y}\right|_{y=0,L_y} = 0 \end{aligned}\right\} . \tag{2-61}$$

Elimination of $\bar{q}_x$ from (2-8), (2-37) and (2-38) now becomes:

$$\left(\frac{U_s \sigma}{2}\right)\phi_s - \left(\frac{h^3}{12\eta}\frac{\partial \bar{p}}{\partial x}\right)\phi_x = \frac{-1}{L_x L_y}\int_o^{L_x}\int_o^{L_y} \frac{(h+\delta_1+\delta_2)^3}{12\eta}\frac{\partial p}{\partial x}\, dy\, dx \; . \tag{2-62}$$

The solution of (2-60)-(2-62) will yield a line with slope f given by:

$$f = \frac{h^3}{6\eta\, U_s \sigma}\frac{\partial \bar{p}}{\partial x} \; . \tag{2-63}$$

The hypothesis to be tested is that if ϕ_x and ϕ_s are independent then all solutions of (2-62) for any f intersect in a common point. This point should be the solutions for ϕ_x and ϕ_s predicted by the previous models. Since the quantities ϕ_x and ϕ_s are random, the right-hand side of (2-62) actually has upper and lower limits given by the confidence interval on this quantity derived from its mean and standard deviation. Hence, the lines given by (2-62) are averaged over several solutions and actually plot as regions bounded by two parallel lines. Hence, a more precise hypothesis of independence requires that there exist a region in the ϕ_x-ϕ_s space that is a subset of all regions of solution to (2-62).

The boundary independence of ϕ_x and ϕ_y is tested by using the model to solve ϕ_x for pure rolling, only by not eliminating the pressure gradient $\frac{\partial \bar{p}}{\partial y}$. This problem appears as:

$$\frac{\partial}{\partial x}\left[(h+\delta_1+\delta_2)^3\,\frac{\partial p}{\partial x}\right]+\frac{\partial}{\partial y}\left[(h+\delta_1+\delta_2)^3\,\frac{\partial p}{\partial y}\right]=0\ . \tag{2-64}$$

$$\left.\begin{array}{ll}(a) & p(0,0)=p_1\\ (b) & p(0,L_y)=p_2\\ (c) & p(L_x,0)=p_4\\ (d) & p(L_x,L_y)=p_3\end{array}\right\}\ . \tag{2-65}$$

Eliminating $\bar{q}_x$ and $\bar{q}_y$ from Equations (2-8), (2-37) and (2-38):

$$\phi_x=\frac{\dfrac{-1}{L_xL_y}\displaystyle\int_o^{L_x}\int_o^{L_y}\frac{(h+\delta_1+\delta_2)^3}{12}\,\frac{\partial p}{\partial x}\,dy\,dx}{\dfrac{-h^3}{12}\,\dfrac{\partial\bar{p}}{\partial x}}\ , \tag{2-66}$$

$$\phi_y=\frac{\dfrac{-1}{L_xL_y}\displaystyle\int_o^{L_y}\int_o^{L_x}\frac{(h+\delta_1+\delta_2)^3}{12}\,\frac{\partial p}{\partial y}\,dx\,dy}{\dfrac{-h^3}{12}\,\dfrac{\partial\bar{p}}{\partial y}}\ , \tag{2-67}$$

where:

$$\frac{\partial\bar{p}}{\partial x}=\frac{p_3+p_4-p_1-p_2}{2\,L_x}\ ,\quad \frac{\partial\bar{p}}{\partial y}=\frac{p_2+p_3-p_1-p_4}{2\,L_y}\ . \tag{2-68}$$

The relative magnitudes of $\frac{\partial\bar{p}}{\partial x}$ and $\frac{\partial\bar{p}}{\partial y}$ are not a factor in the solution of (2-64)-(2-66) for ϕ_x and ϕ_y. This is because for a given nominal $\frac{\partial\bar{p}}{\partial y}$, ϕ_x is independent of $\frac{\partial\bar{p}}{\partial x}$ because it is a linear effect. The same is true of ϕ_y given $\frac{\partial\bar{p}}{\partial x}$. However, this model can be used to check the effect of boundary conditions on ϕ_x and also to test Equation (2-56).

Numerical Formulation of Flow Models

All of the models mentioned require artificial surface generations of δ_1 and δ_2 with a given frequency distribution and surface pattern parameter and mean zero. Since many engineering surfaces are approximately Gaussian distributed, only these surfaces will be considered herein. However, the phenomenon of asperity shear can lead to a truncated distribution at a significant height level and this would change the flow characteristics significantly. Hence, the Gaussian-truncated distributions will also be considered (Figure 2-9).

Artificial surface generation begins with the generation of an array $Z_{i,j}$ for $i = 1,\ldots,n_x$ and $j = 1,\ldots,n_y$ such that $Z_{i,j}$ is normally distributed with mean zero and standard deviation σ. The desired surface pattern parameter is imposed on the array by a transformation provided by Patir [18].

$$\delta_{i,j} = \frac{1}{nm} \sum_{k=1}^{n} \sum_{\ell=1}^{m} Z_{i+k,j+\ell} \cdot \qquad (2\text{-}69)$$

The resulting array $\delta_{i,j}$ has linear profile correlation functions R_x and R_y such that $R_x(0) = R_y(0) = \sigma^2$, $R_x(n\Delta x) = 0$, $R_y(m\Delta y) = 0$ where Δx and Δy are the grid spacings over which the array $\delta_{i,j}$ is superimposed. Since the functions R_x and R_y are linear, the 50% delay lengths are given by:

$$\lambda_{0.5\ x} = \frac{n\Delta x}{2}, \quad \lambda_{0.5\ y} = \frac{m\Delta y}{2} \cdot \qquad (2\text{-}70)$$

Hence, the surface pattern parameter becomes:

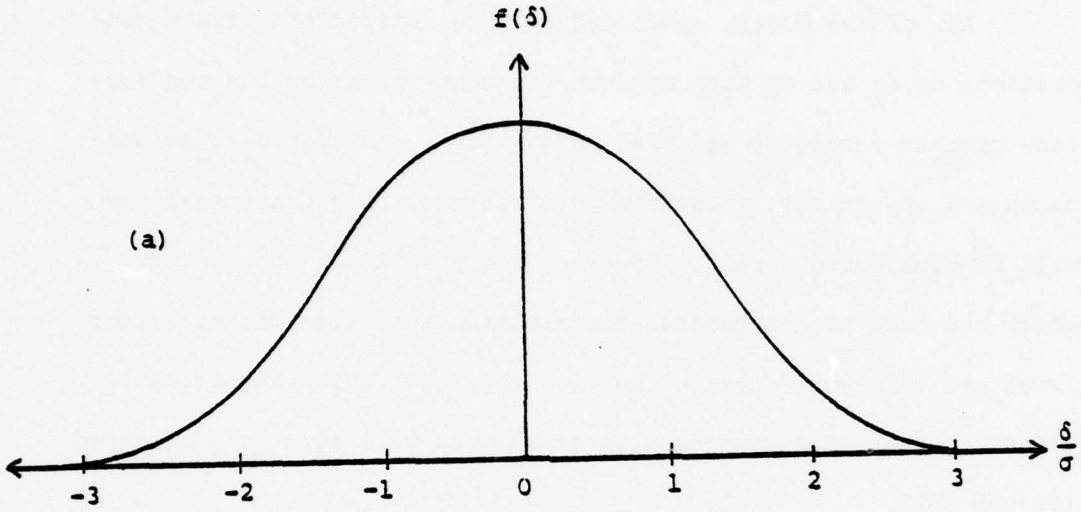

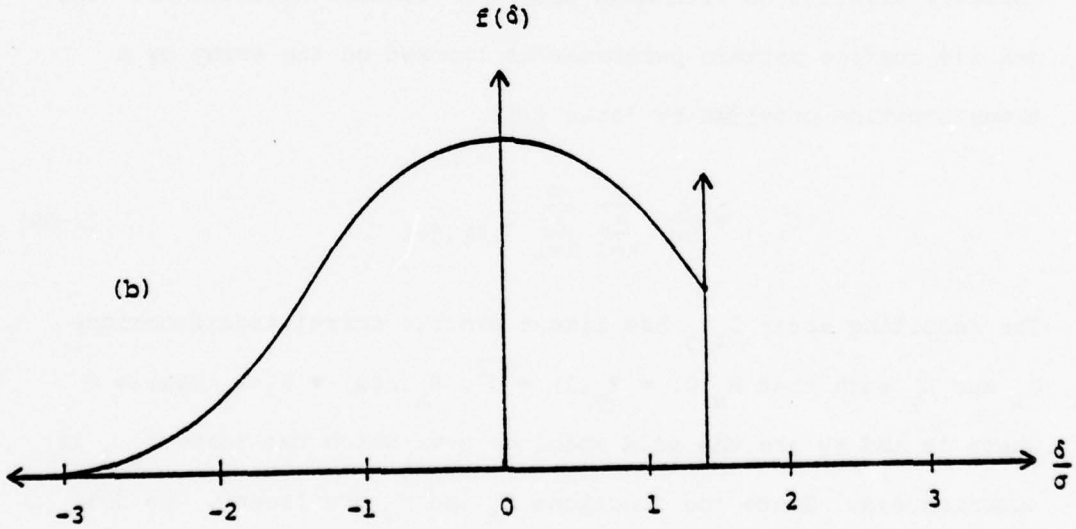

Figure 2-9. Roughness Density Functions
(a) Gaussian-symmetric
(b) Truncated

$$\gamma = \frac{\lambda_{0.5\ x}}{\lambda_{0.5\ y}} = \frac{n}{m}\frac{\Delta x}{\Delta y} \ . \tag{2-71}$$

The parameter γ is then controlled by selection of n and m.

Having generated δ_1 and δ_2 discreetly over the grid $N_x \times N_y$ it is necessary to form the film thickness array. From Equation (2-11):

$$H_{i,j} = h + \delta_{1_{i,j}} + \delta_{2_{i,j}} \ . \tag{2-72}$$

For the Gaussian-symmetric distribution the contact condition implies that if $H_{i,j} < 0$, set $H_{i,j} = H_{min}$ where H_{min} is some minimum possible film thickness greater than zero. The probability of contact can be found using the Gaussian density function $f_g(\delta)$:

$$P[H_{i,j} < 0] = \int_{-\infty}^{-h/\sigma} f_g\left(\frac{\delta}{\sigma}\right)\, d\,\frac{\delta}{\sigma} \ . \tag{2-73}$$

The truncated distribution has a slightly different contact condition. First, a level of truncation rh is selected (Figure (2-10) Based on the directions in which δ_1 and δ_2 are defined in the sketch, δ_1 and δ_2 are first truncated according to:

$$\begin{aligned} &\text{If } \delta_{1_{i,j}} < -rh \quad \text{set } \delta_{1_{i,j}} = -rh + \tfrac{1}{2} H_{min} \ ; \\ &\text{If } \delta_{2_{i,j}} < -(1-r)h \text{ set } \delta_{2_{i,j}} = -(1-r)h + \tfrac{1}{2} H_{min} \ . \end{aligned} \tag{2-74}$$

$H_{i,j}$ is then formed according to (2-72) and the minimum value of $H_{i,j}$ will be H_{min}. Now the probability of contact is the product of two probabilities:

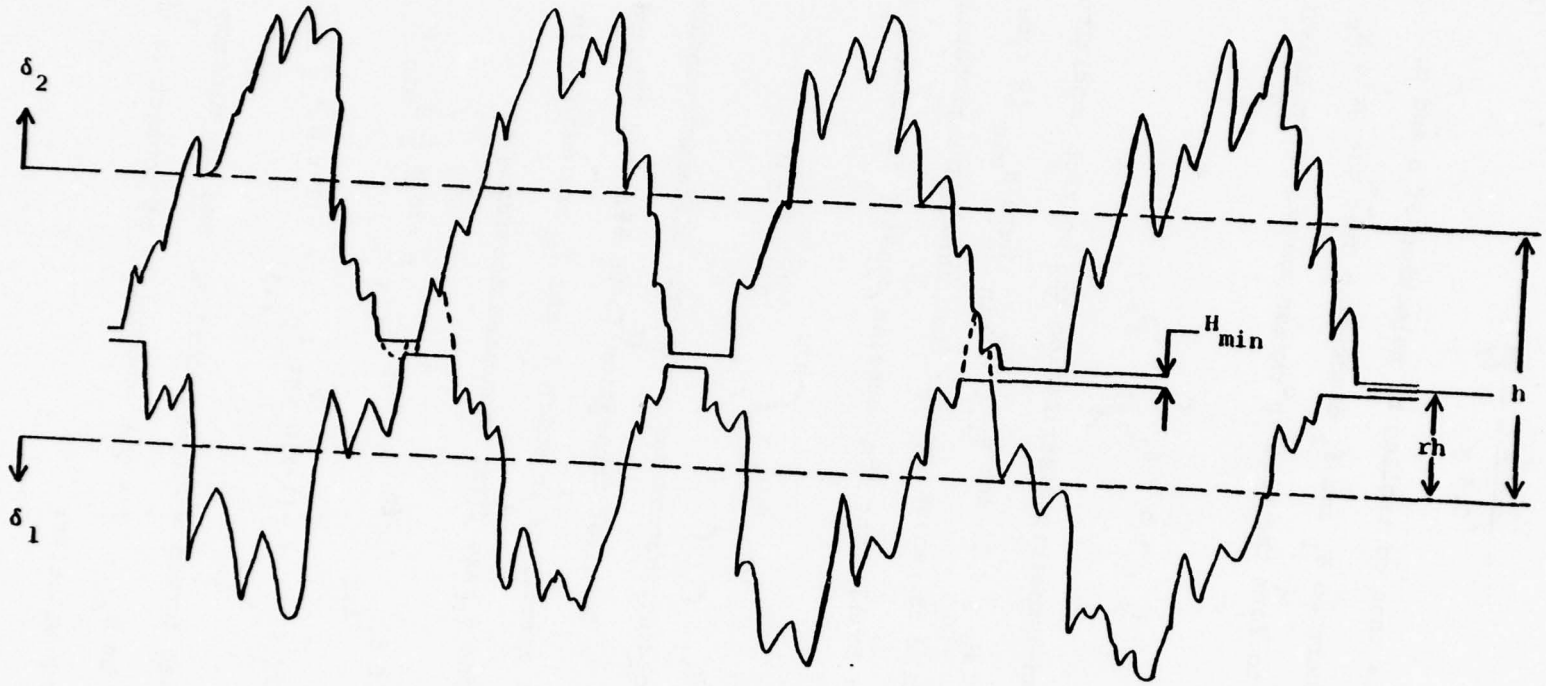

Figure 2-10. Profile of Truncated Distribution Surface

$$P\left[H_{i,j} = H_{min}\right] = P\left[\delta_{1_{i,j}} < -rh\right] P\left[\delta_{2_{i,j}} < -(1-r)h\right]$$

$$= \left[\int_{-\infty}^{-rh/\sigma} f_g\left(\frac{\delta_1}{\sigma_1}\right) d\,\frac{\delta_1}{\sigma_1}\right]\left[\int_{-\infty}^{-(1-r)h/\sigma} f_g\left(\frac{\delta_2}{\sigma_2}\right) d\,\frac{\delta_2}{\sigma_2}\right]. \tag{2-75}$$

It should be noted that a value of r = 1 reduces the area of contact by $P\left[\delta_{2_{i,j}} < 0\right]$ or 0.5 of the value for the Gaussian-symmetric distribution. Hence, the truncated distribution will be characterized by less contact than the symmetric distribution. It is also true that for a given h/σ, the value r = 0.5 produces the most contact and contact decreases with increasing or decreasing r from 0.5. This situation of less contact in the truncated case is illustrated in Figure 2-10. The dotted lines which have been truncated would have otherwise produced contact in some cases for a symmetric distribution.

The next step in numerical formulation of the model involves the selection of a grid network to serve as a basis for finite difference equations. Two such networks are shown in Figures 2-11 and 2-12. Figure 2-11 uses diagonal elements which are believed to be the ones selected by Patir [18] for his work. The next figure depicts rectangular elements which form the basis for the work herein. Each of these element selections have a valid physical interpretation and will be discussed separately.

Patir's method places the pressures in a rectangular grid $P_{i,j}$ for $i = 1,\ldots,N_x - 1$ and $j = 1,\ldots,N_y - 1$. The film thickness function is generated at both the pressure or grid points and at

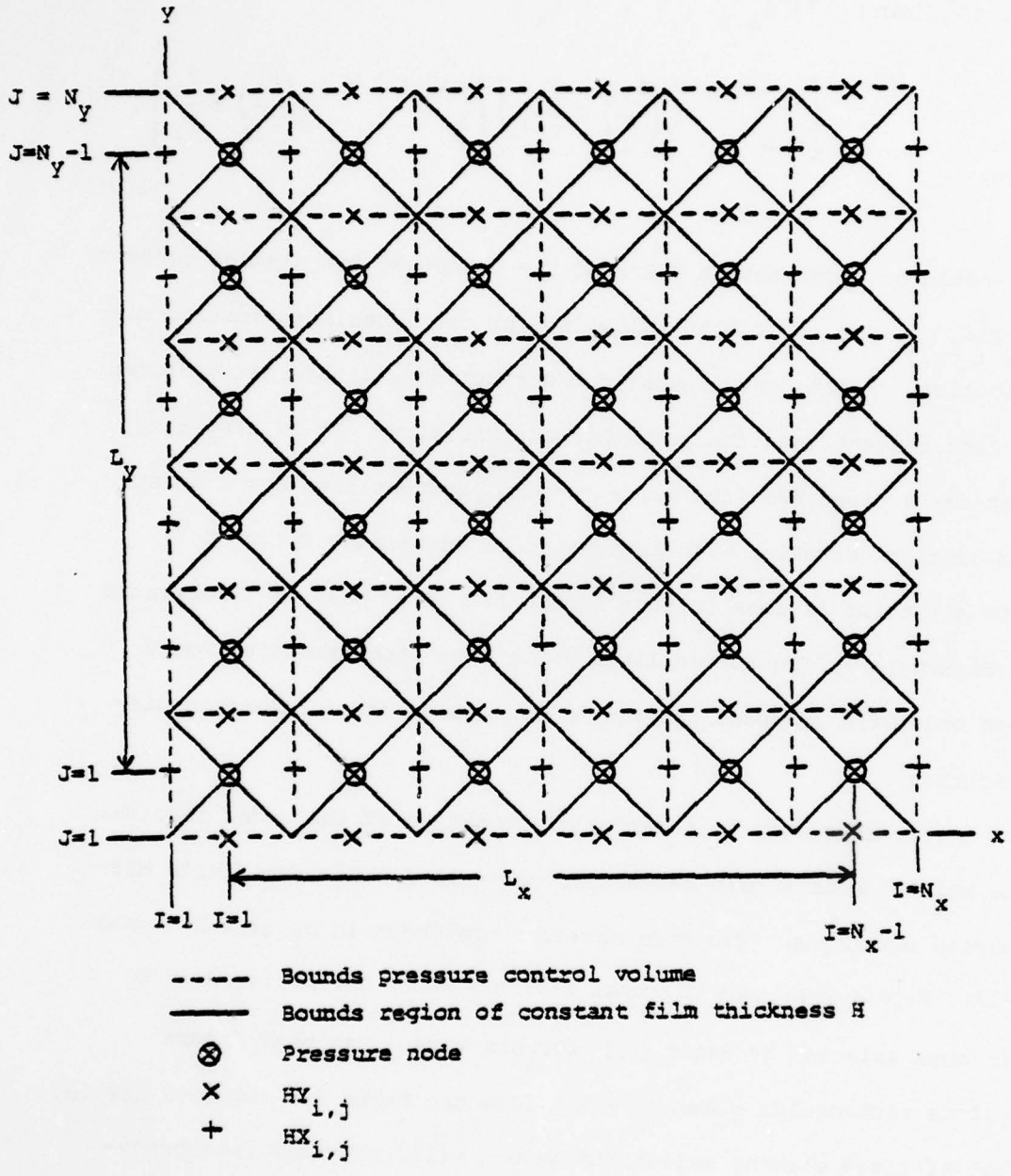

Figure 2-11. Grid Network for Patir Method

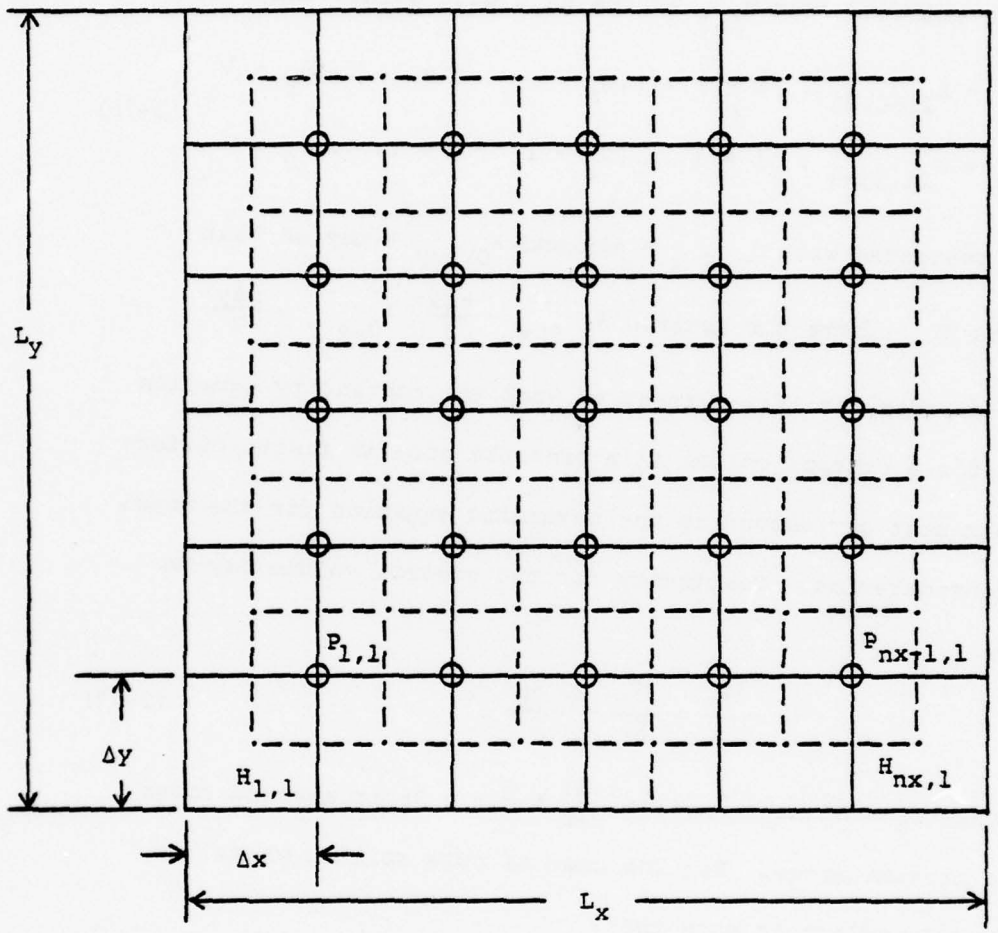

Bounds pressure control volume

Bounds region of constant film thickness H

Pressure node

$H_{i,j}$

Figure 2-12. Grid Network for Corner Point Method

the half-grid points resulting in $H_{i,j}$ for $i = 1,\ldots,2\,N_x - 1$ and $j = 1,\ldots,2\,N_y - 1$. Next, two separate arrays $HX_{i,j}$ and $HY_{i,j}$ are selected from $H_{i,j}$ at the half grid points only:

$$\begin{aligned} HX_{i,j} &= H_{2i-1,2j}\,, \quad i = 1,\ldots,N_x \qquad j = 1,\ldots,N_y - 1 \\ HY_{i,j} &= H_{2i,2j-1}\,, \quad i = 1,\ldots,N_x - 1 \quad j = 1,\ldots,N_y\,. \end{aligned} \tag{2-76}$$

$H_{i,j}$ is generated with $\lambda_{0.5\,x} = n\Delta x$ and $\lambda_{0.5\,y} = m\Delta y$ so that $HX_{i,j}$ and $HY_{i,j}$ have the desired $\lambda_{0.5\,x} = \frac{n\Delta x}{2}$, $\lambda_{0.5\,y} = \frac{m\Delta y}{2}$.

In order for this element to work the continuity equation written for a control volume at a pressure node in finite difference form must correspond to the governing equation for the model under consideration. Continuity for the control volume may be written:

$$\frac{\partial q_x}{\partial x} + \frac{\partial q_y}{\partial y} = -\frac{\partial H}{\partial t}\,. \tag{2-77}$$

It is only convenient to analyze $\frac{\partial H}{\partial t}$ for the Patir element under certain circumstances. For the case of pure rolling where $U_1 = U_2 = U$, select Δt such that:

$$\Delta x = U\Delta t\,. \tag{2-78}$$

Then $\frac{\partial H}{\partial t}$ is solved by a central difference in time:

$$\begin{aligned} \frac{\partial H}{\partial t} &= \frac{1}{\Delta t}\left[H(x,y,t + \tfrac{1}{2}\Delta t) - H(x,y,t - \tfrac{1}{2}\Delta t)\right] \\ &= \frac{U}{\Delta x}\left[H(x - \tfrac{1}{2}\Delta x,y,t) - H(x + \tfrac{1}{2}\Delta x,y,t)\right]\,. \end{aligned} \tag{2-79}$$

Since both surfaces are moving in the same direction, the

expression in (2-79) becomes

$$\left.\frac{\partial H}{\partial t}\right|_{i,j} = \frac{U}{\Delta x}\left[HX_{i,j} - HX_{i+1,j}\right] . \qquad (2\text{-}80)$$

When the remainder of Equation (2-77) is finite differenced, it is found that the velocity flow terms on the left side cancel the $-\frac{\partial H}{\partial t}$ terms. Hence, the right side becomes zero so this element correctly models the governing equation for pure rolling given in (2-64).

For pure sliding where $U_1 = -U_2 = -\frac{1}{2} U_s$, $\frac{\partial H}{\partial t}$ is evaluated as follows:

$$\Delta x = \frac{1}{2} U_s \Delta t . \qquad (2\text{-}81)$$

$$\frac{\partial H}{\partial t} = \frac{1}{\Delta t}\left[H(t + \frac{\Delta t}{2}, x, y) - H(t - \frac{1}{2}\Delta t, x, y)\right]$$

$$= \frac{U_s}{2\Delta x}\left\{\left[h + \delta_1(t, x + \frac{1}{2}\Delta x, y) + \delta_2(t, x - \frac{1}{2}\Delta x, y)\right]\right.$$

$$\left. - \left[h + \delta_1(t, x - \frac{1}{2}\Delta x, y) + \delta_2(t, x + \frac{1}{2}\Delta x, \Delta y)\right]\right\} . \qquad (2\text{-}82)$$

Equation (2-82) assumes surface 2 moving in the positive x-direction as implied by (2-81). Converting to indices:

$$\frac{\partial H}{\partial t} = \frac{U_s}{2\Delta x}\left[\left(h + \delta_{1_{i+1,j}} + \delta_{2_{i,j}}\right) - \left(h + \delta_{1_{i,j}} + \delta_{2_{i+1,j}}\right)\right] . \qquad (2\text{-}83)$$

Although the h terms in (2-83) could be cancelled, it is easier to enforce the contact conditions if the expressions in parenthesis are stored in separate arrays Hx^+ and Hx^-. The result of Equation (2-77) for pure sliding:

$$- \frac{HX^3_{i,j}}{12}\left(\frac{P_{i,j}-P_{i-1,j}}{\Delta x}\right)\Delta y - \frac{HY^3_{i,j}}{12}\left(\frac{P_{i,j}-P_{i,j-1}}{\Delta y}\right)\Delta x$$

$$+ \frac{HX^3_{i+1,j}}{12}\left(\frac{P_{i+1,j}-P_{i,j}}{\Delta x}\right)\Delta y + \frac{HY^3_{i,j+1}}{12}\left(\frac{P_{i,j+1}-P_{i,j}}{\Delta y}\right)\Delta x$$

$$= - \frac{U_s \Delta y}{2}\left(HX^+_{i,j} - HX^-_{i,j}\right) . \qquad (2\text{-}84)$$

Equation (2-84) correctly represents the equation for pure sliding given by (2-57). It is emphasized that $\frac{\partial H}{\partial t}$ for the Patir element cannot be evaluated in the limit of $\Delta t \to 0$ since Δt is finite. Hence, only the configurations of pure rolling ($U_1 = U_2 = U$) and pure sliding ($U_1 = -U_2 = -\frac{1}{2} U_s$) can be analyzed.

The second grid, termed the corner point method, is based on an idea by Castelli [19] and is sketched in Figure 2-12. Again, the pressure array is rectangular and described by $P_{i,j}$ for $i = 1,\ldots,N_x - 1$ and $j = 1,\ldots,N_y - 1$. In this arrangement the film thickness array is generated only at the element midpoints and becomes $H_{i,j}$ for $i = 1,\ldots,N_x$ and $j = 1,\ldots,N_y$.

The analysis of $\frac{\partial H}{\partial t}$ for the control volume shown in Figure 2-13 is simple and general. With the aid of Figure 2-13, the volume V of the control volume at time t is given by:

$$V(t) = \left(H_{i,j} + H_{i+1,j} + H_{i,j+1} + H_{i+1,j+1}\right) \frac{\Delta x \Delta y}{4} \qquad (2\text{-}85)$$

Now subjecting each surface to a small time increment Δt and assuming $U_2 > U_1$, the volume at time $t + \Delta t$ can be written:

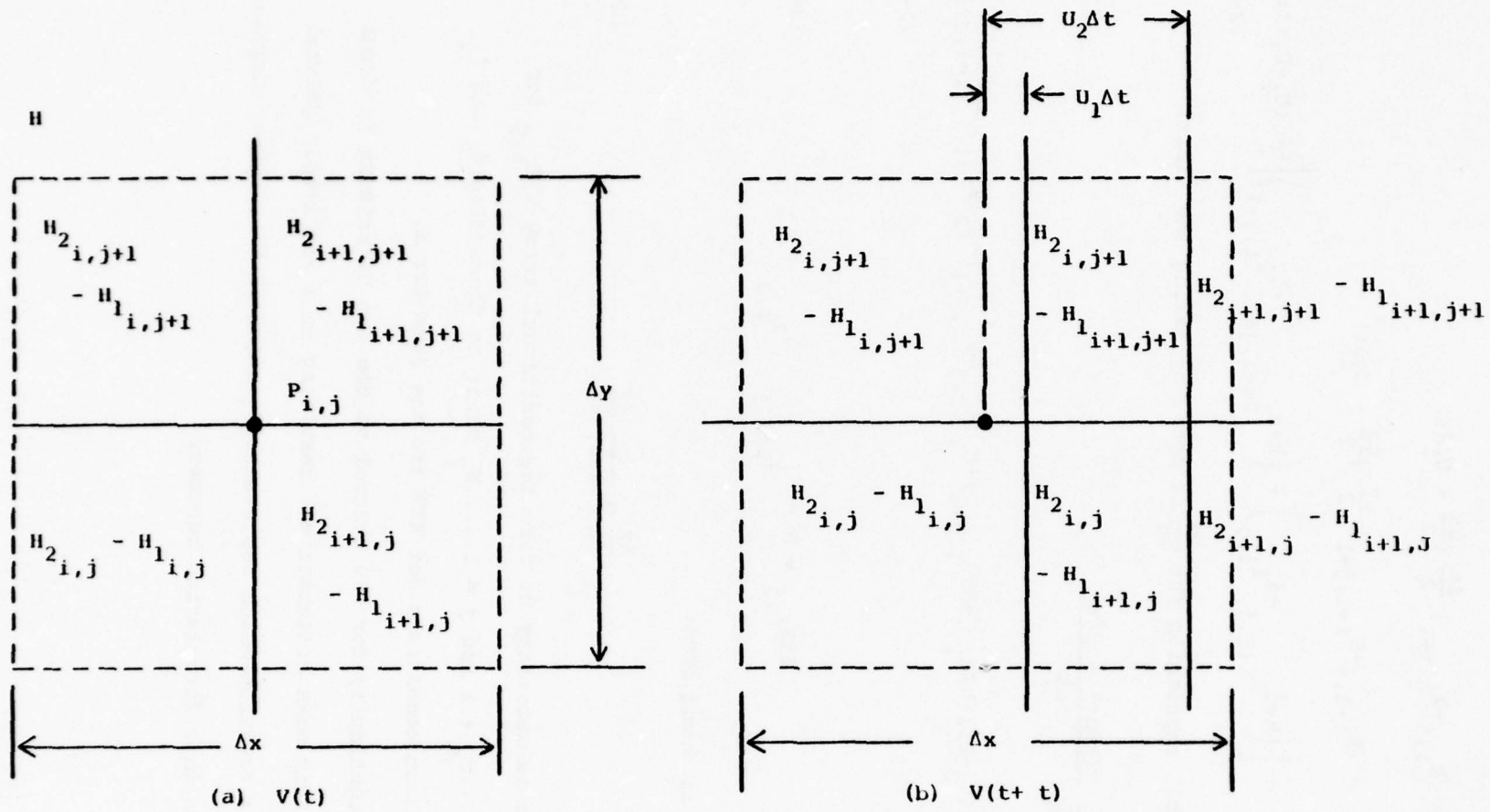

Figure 2-13. Control Volume for CPM

$$V(t+\Delta t) = [H_{i,j}+H_{i,j+1}]\frac{\Delta y}{2}\left(\frac{\Delta x}{2} + U_1\Delta t\right)$$

$$+ [H_{i+1,j}+H_{i+1,j+1}]\frac{\Delta y}{2}\left(\frac{\Delta x}{2} - U_2\Delta t\right)$$

$$+ \left[\left(h+\delta_{1_{i+1,j}}+\delta_{2_{i,j}}\right) + \left(h+\delta_{1_{i+1,j+1}}+\delta_{2_{i,j+1}}\right)\right]\frac{\Delta y}{2}(U_2-U_1)\Delta t \ . \tag{2-86}$$

The general expression for $\frac{\partial V}{\partial t}$ is found by taking the limit:

$$\frac{\partial V}{\partial t} = \lim_{\Delta t \to 0} \frac{V(t+\Delta t) - V(t)}{\Delta t}$$

$$= \frac{\Delta y}{2}[(U_2-U_1)(HTR_{i,j}+HTR_{i,j+1})+U_1(H_{i,j}+H_{i,j+1})-U_2(H_{i+1,j}+H_{i+1,j+1})] \tag{2-87}$$

where:

$$HTR_{i,j} = h + \delta_{1_{i+1,j}} + \delta_{2_{i,j}} \ . \tag{2-88}$$

Then $\frac{\partial H}{\partial t}$ is found from:

$$\frac{\partial H}{\partial t} = \frac{1}{\Delta x \Delta y}\frac{\partial V}{\partial t} \ . \tag{2-89}$$

Thus, it is necessary to form the additional array $HTR_{i,j}$ for $i = 1,\ldots,N_x - 1$ and $j = 1,\ldots,N_y$ prior to discarding δ_1 and δ_2. The contact conditions for HTR are the same for H.

Continuity for the control volume can be written in terms of explicit mass conservation, resulting in a completely general Reynolds equation which represents Equation (2-51). After simplification this formulation becomes:

$$A_{i,j}P_{i,j} = B_{i,j}P_{i-1,j} + C_{i,j}P_{i+1,j} + D_{i,j}P_{i,j-1} + E_{i,j}P_{i,j+1} + F_{i,j} ,$$

$$A_{i,j} = (H^3_{i,j} + H^3_{i+1,j} + H^3_{i,j+1} + H^3_{i+1,j+1}) \left(\frac{\Delta y}{\Delta x} + \frac{\Delta x}{\Delta y}\right) ,$$

$$B_{i,j} = (H^3_{i,j} + H^3_{i,j+1}) \frac{\Delta y}{\Delta x} ,$$

$$C_{i,j} = (H^3_{i+1,j} + H^3_{i+1,j-1}) \frac{\Delta y}{\Delta x} ,$$

$$D_{i,j} = (H^3_{i,j} + H^3_{i+1,j}) \frac{\Delta x}{\Delta y} ,$$

$$E_{i,j} = (H^3_{i,j+1} + H^3_{i+1,j+1}) \frac{\Delta x}{\Delta y} ,$$

$$F_{i,j} = -12\,\eta(U_2 - U_1)\Delta y \left[HTR_{ij} + HTR_{i,j+1} - \frac{1}{2}(H_{i,j} + H_{i,j+1} + H_{i+1,j} + H_{i+1,j+1})\right] . \quad (2\text{-}90)$$

It is observed that Equation (2-90) is completely general and reduces to the required equations for pure rolling and pure sliding. An additional advantage lies in the fact that any combination of rolling and sliding may be solved with the same equation.

Patir has contended that the film thickness at the half-grid points should be defined directly rather than averaged because averaging changes the statistics of the surface. While it is certainly true that the half-grid film heights would have to be averaged if the roughness was generated at the pressure points, it is not necessary for the corner point method just described. Granted that the finite difference equation appears to have average terms

on the left-hand side, it is not the case in terms of pure physical reasoning. This method has advantages of smaller roughness grids required, only a single array describes each surface and the method is general.

Aside from the method of formulation, there are other differences between the Patir method and the corner point method (CPM) that have physical meaning. The Patir contact points are half as large as the CPM and there are twice as many contacts for a given h and delay correlation values n,m. For sufficiently large grids $N_x \times N_y$ this is not a critical factor. It is also noticed that a single Patir contact only blocks leakage in one direction only. This is not realistic. The CPM contact obstructs leakage in both directions, and it would be reasonable to assume that the CPM would have a higher resistance to flow. However, the path length around a Patir contact is considerably longer than the path length around a CPM contact which offsets the higher flow resistance mentioned.

These concepts can be illustrated by considering the example ϕ_x flow problem shown in Figure 2-14. The grids for the Patir method and the corner point method are carefully drawn so that each bearing segment has a total available flow area of 9 $\Delta x \Delta y$. The film thickness in all elements is taken to be unity except for the cross-hatched regions which are contacts where H = 0. Film thicknesses are indicated in the elements and boundary conditions are enforced with $p_a = 1$, $p_b = 0$. Leakage in the y-direction out the ends is prevented by placing contact points in the flow path at these locations. Two contacts are located in the Patir grid as shown

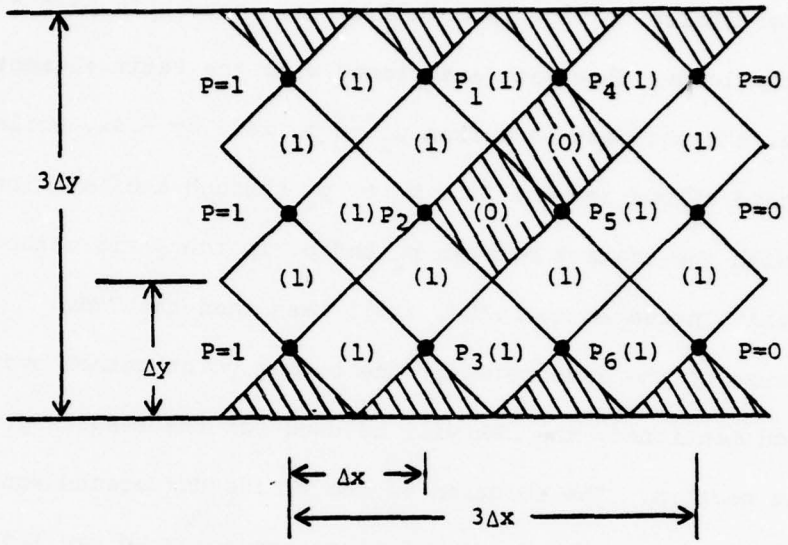

(a) Patir method

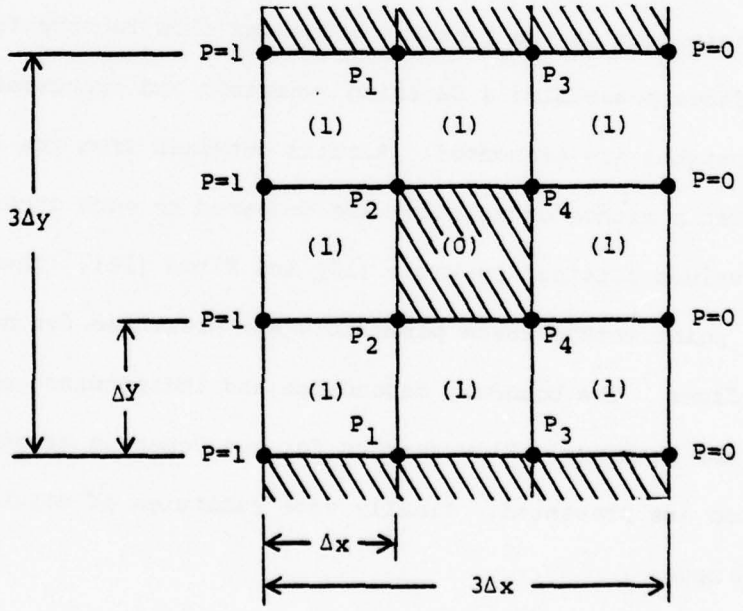

(b) CPM

Figure 2-14. Models to Compare Solution Methods

and one in the CPM grid so that the contact area in each case is 1/9. Solution of ϕ_x for the Patir method is 0.778 while the CPM ϕ_x is 0.846. This exercise indicates that the Patir method offers a greater resistance to flow in a fundamental sense. In part this is due to the longer flow path associated with the Patir element. For example, the shortest path from p_2 to p_5 is $2\Delta y + \Delta x$, while the CPM method allows leakage from p_2 to p_4 through the path length Δx. Even with the contact between p_4 and p_5 in the Patir method removed, ϕ_x only increases to 0.800, still less than the CPM.

Because of the advantages of the corner point method over the Patir method mentioned, the CPM will be used for the results presented in the next section. The solution of the finite difference equations is by overrelaxation. Boundary conditions are enforced explicitly.

RESULTS OF THE AVERAGE FLOW MODEL

In this section the pressure and shear flow factors for isotropic surfaces possessing a Gaussian symmetric and truncated distribution of heights are presented. Results obtained from the corner point and Patir method of solution are compared to each other and to published values obtained by Patir [18] and Elrod [16]. Then using the corner point method these parameters are presented for non-isotropic surfaces. The boundary dependence and independence of ϕ_x, ϕ_y and ϕ_s are examined. Flow factors for the Gaussian truncated distribution are presented. Finally some estimates of solution accuracy are made.

Flow Factors for Gaussian-symmetric Surfaces

The solutions for the pressure flow factor ϕ_x at $\gamma = 1$ or for isotropic surfaces are shown in Figure 2-15. Four results are plotted on this figure, two of which are published solutions by Elrod [16] and Patir [18]. Solution points obtained from the corner point method (CPM) and the Patir method are bracketed by 90% confidence intervals based on 10 solution averages. The same set of different but statistically identical surfaces was used for each value of h/σ in order to obtain smooth results.

Comparing the Patir published result to that of the Patir method obtained herein, it is observed that the published result barely intersects the confidence interval of the Patir method results. Several seed numbers generating different sets of surfaces were tried in an attempt to obtain better agreement but none altered this comparison. It is concluded that the set of surfaces used by Patir in obtaining the published curve may have been somewhat of an improbable occurrence, or that the relative asperity size to grid size used by Patir differed from that used herein. The latter point will be discussed in some detail later. In any case the published results are statistically possible and are considered satisfactory by this investigation.

The solution curve for ϕ_x from the CPM is qualitatively similar to the Patir result but higher as was predicted from the comparative discussion on the two methods. This indicates that the assumptions about the shape and character of a representative asperity are important to the outcome of the flow factors. The

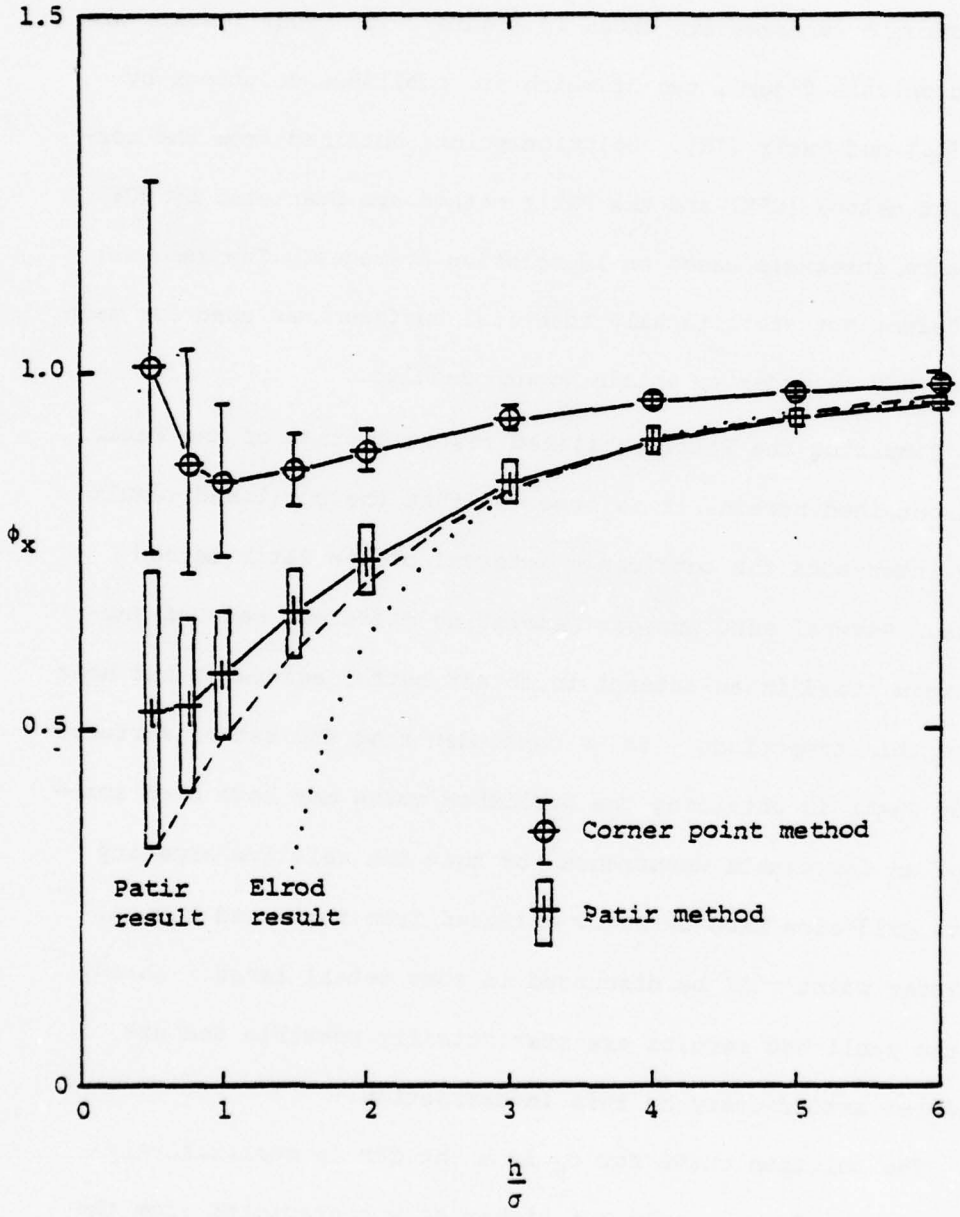

Figure 2-15. ϕ_x for Isotropic, Gaussian-symmetric Surfaces

square element chosen for the CPM offers less resistance to flow than the Patir element.

It is demonstrated that the results obtained independently by Elrod using a perturbation technique [16] agree quite well with the Patir results for $h/\sigma > 3$. The method used by Elrod is only valid for large h/σ and the limitation on the minimum acceptable value is not calculated. Although the results from the corner point method shown in Figure 2-15 do not agree with Elrod, there are a few selective seed numbers for which agreement was achieved for $h/\sigma \geq 4$. One such result is presented in Figure 2-16. Hence all of the results in Figure 2-15 are considered acceptable for the regime $h/\sigma > 3$.

The curves of Figure 2-15 also show an increase in the 90% confidence interval as $h/\sigma \rightarrow 0.5$. This behavior occurs for two reasons. First, the factor ϕ_x is normalized by the nominal leakage (Equation 2-54). As h/σ is reduced, the width of the confidence interval increases accordingly since the denominator decreases with $(h/\sigma)^3$. For example, the reduction in nominal leakage flow from $h/\sigma = 2$ to $h/\sigma = 1$ is a factor of 8. Hence a 2.5% scatter at $h/\sigma = 2$ becomes a 20% scatter at $h/\sigma = 1$. Second, actual flows become small as the nominal leakage becomes small resulting in some machine roundoff error. This is a minor source of scatter.

The non-isotropic results for ϕ_x obtained by the CPM are presented in Figure 2-17. These results are qualitatively comparable to the Patir results (not shown) and in all cases the estimation of roughness effects by the CPM indicate less flow

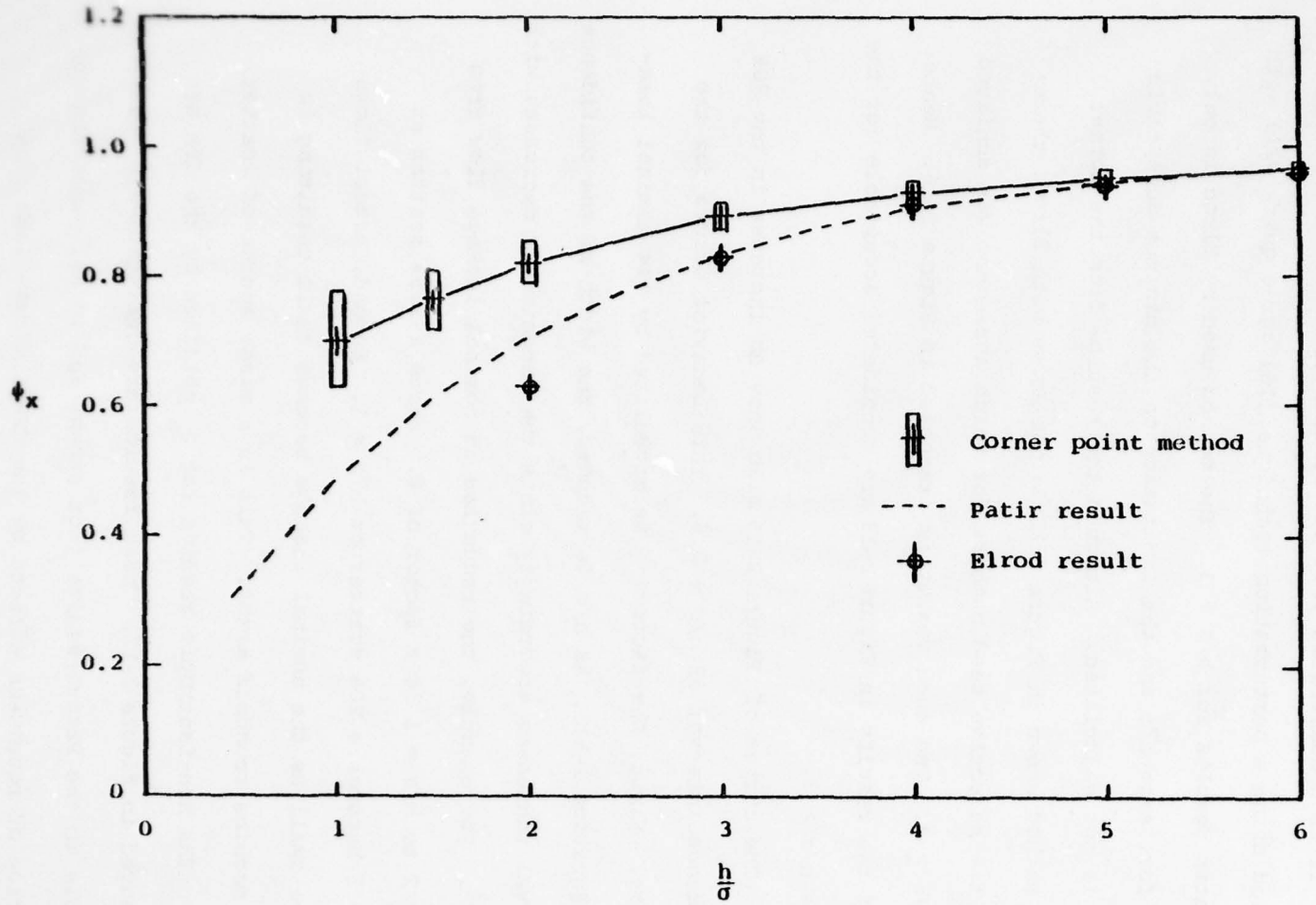

Figure 2-16. ϕ_x for Isotropic, Gaussian-symmetric Surface Using CPM

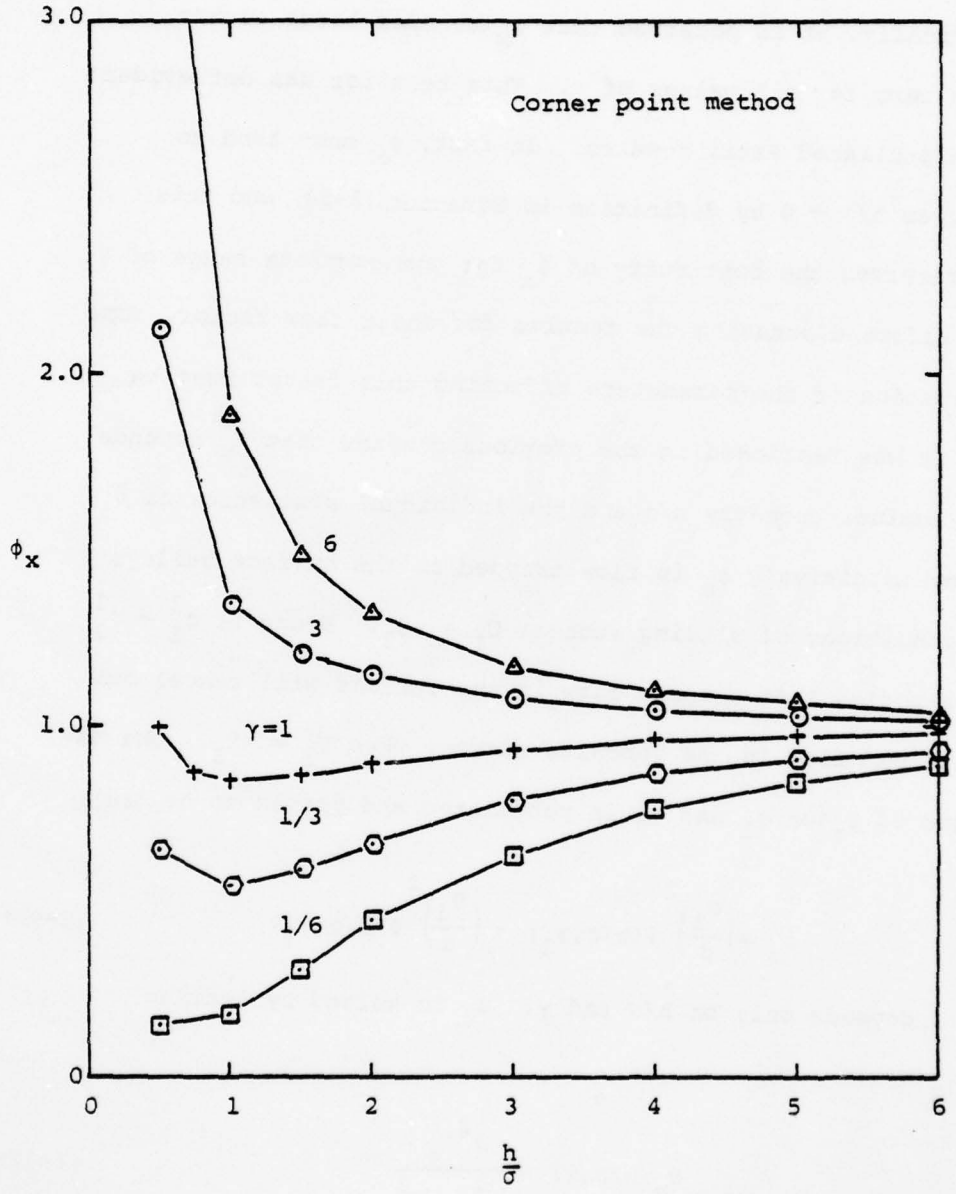

Figure 2-17. ϕ_x for Non-isotropic, Gaussian-symmetric Surfaces

resistance than the Patir model predicts. It is also evident that the requirement $\phi_x \to 1$ as $h/\sigma \to \infty$ is satisfied for all values of γ.

Finally, it is observed that ϕ_x becomes large as h/σ tends to zero for all values of γ. This behavior was not evident from the published Patir results. In fact, ϕ_x must tend to infinity as $h/\sigma \to 0$ by definition in Equation (2-54) and this point preserves the continuity of ϕ_x for the complete range of γ.

Before discussing the results for shear flow factor, some clarification of the parameters affecting this factor must be made. It was mentioned in the previous chapter that ϕ_s depends on the nominal geometry h/σ and the individual statistics of δ_1, δ_2. Now intuitively ϕ_s is flow trapped in the surface valleys under conditions of sliding such as $U_1 = -U_2$. Hence if $\sigma_1^2 = \sigma_2^2$ it is expected that trapped flow in one surface will cancel out with trapped flow in the opposite surface when $U_1 = -U_2$. The dependence of ϕ_s on σ_1 and σ_2 is postulated and proven to be [18]:

$$\phi_s = \left(\frac{\sigma_2}{\sigma}\right)^2 \Phi(h/\sigma,\gamma_2) - \left(\frac{\sigma_1}{\sigma}\right)^2 \Phi(h/\sigma,\gamma_1) \qquad (2\text{-}91)$$

where Φ depends only on h/σ and γ. Φ_s is solved by letting $\gamma_1 = \gamma_2 = \gamma$:

$$\Phi_s(h/\sigma,\gamma) = \frac{\sigma^2 \phi_s}{\sigma_2^2 - \sigma_1^2} \qquad (2\text{-}92)$$

In results not included herein the non-dependence of Φ_s on σ_1,σ_2 is verified and the dependence of ϕ_s on σ_1,σ_2 is removed by the hypothesis of Φ_s in Equation (2-91).

The results for Φ_s using isotropic surfaces and $\sigma_1^2 \neq \sigma_2^2$ are presented in Figure 2-18. It is observed that the published curve has a slightly different shape from the Patir method curve. Patir's published curve intersects the 10 point 90% confidence interval everywhere except the region from $3 \leq h/\sigma \leq 5$. This behavior cannot be explained without more intimate knowledge of Patir's work.

Again the CPM solution behaves as anticipated. Since this method offers less resistance to pressure forced flow, it also drags less self-induced flow in the absence of a nominal pressure gradient. The results are everywhere less than the Patir result and the closeness to the Patir result is about the same as for ϕ_x.

For this flow factor it is observed that the scatter in results does not increase as $h/\sigma \to 0$. This is because shear flow is normalized in terms of the sliding velocity $U_s = U_2 - U_1$ (Equation 2-59) which is invariant of h/σ . The size of the confidence interval is related to the magnitude of the flow factor only, but is subject to some roundoff as $h/\sigma \to 0$.

Shear flow has a maximum value for h/σ near 1.25. This is because as h/σ is decreased from 6, the pressure gradients, which are nominally zero, increase due to the surface roughness effects. However, when h/σ becomes small enough, the increase in pressure gradient is offset due to the decrease in "valley" volume. Hence as $h/\sigma \to 0$, Φ_s tends to a small value not necessarily 0. As $h/\sigma \to \infty$ it is observed that Φ_s tends to zero, as well as $\partial\Phi_s/\partial(h/\sigma)$. This is noted because the actual quantity of interest is $\partial\phi_s/\partial x = (\partial\phi_s/\partial h)(\partial h/\partial x)$ in Equation (2-40).

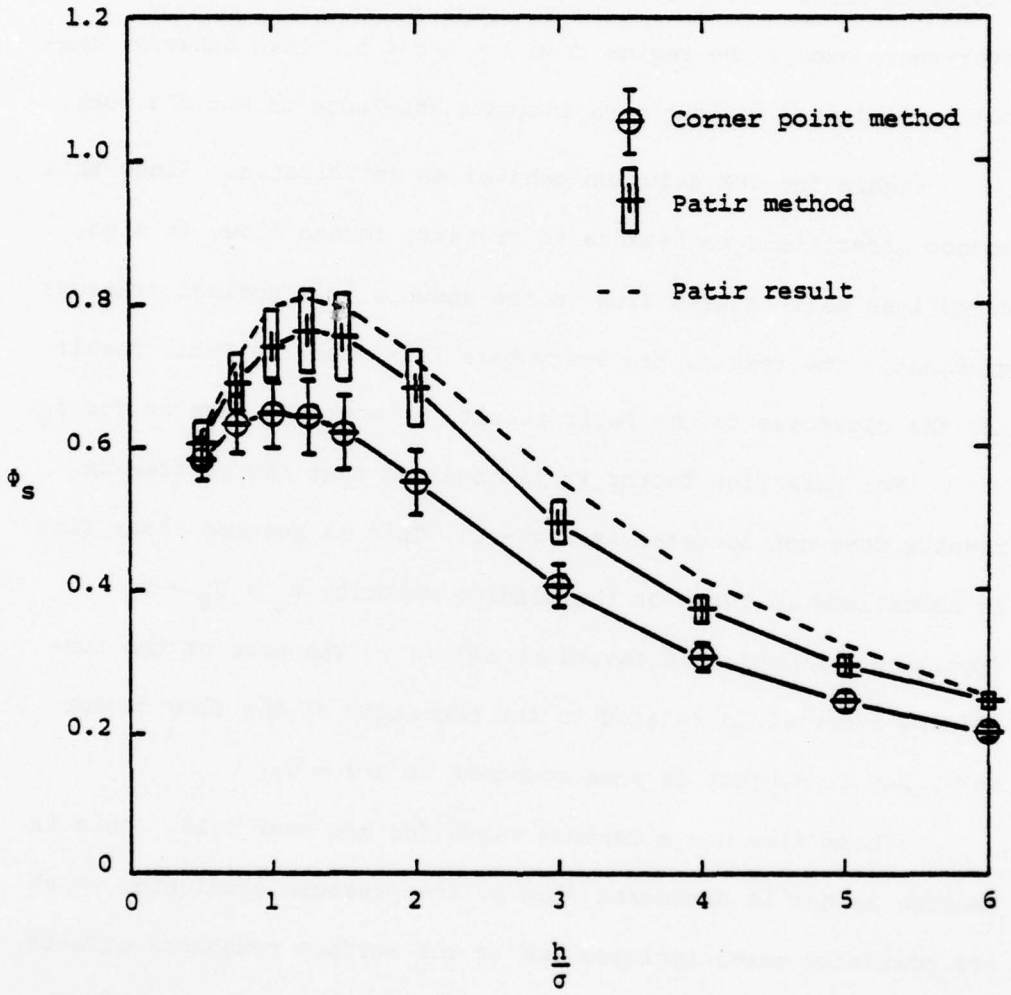

Figure 2-18. Φ_s for Isotropic, Gaussian-symmetric Surfaces

ϕ_s for non-isotropic surfaces as predicted by the CPM are shown in Figure 2-19. These results indicate less flow due to sliding than the Patir results. The reason shear flow increases with decreasing γ is that the valley volume is greater for more transverse surfaces since the valleys are longer in the direction perpendicular to sliding. For purely longitudinal surfaces it is expected that very little flow would be picked up since there are no transverse surfaces to trap the fluid in the valleys.

Independence of Flow Factors

As described previously, the independence of ϕ_x and ϕ_s is tested by imposing both a sliding velocity and a nominal pressure gradient $\frac{\partial \bar{p}}{\partial x}$. By varying the relative magnitude of the sliding velocity and the nominal pressure gradient, the lines plotted in Figure 2-20 are determined. Each solid line represents the mean for $E\left[\frac{-H^3}{12}\frac{\partial p}{\partial x}\right]$ and is bounded by 90% confidence intervals based on 10 point averages. It is evident that ϕ_x and ϕ_s are indeed independent, for all regions bounded by confidence intervals intersect the dark region which contains the previous solutions for ϕ_x and ϕ_s at $h/\sigma = 2$, $\gamma = 1$.

The boundary dependence of ϕ_x and ϕ_y is tested by completely specifying pressure on the boundary, as described in the previous chapter. Results for $\gamma = 1$, using Gaussian-symmetric surfaces, are tabulated in Table 2-1. It is first observed that the values ϕ_x and ϕ_y do not depend significantly on the ratio of the magnitude of the pressure gradients applied to the model as predicted. Next, it is noted that $\phi_x = \phi_y$ satisfactorily for $\gamma = 1$ as they should.

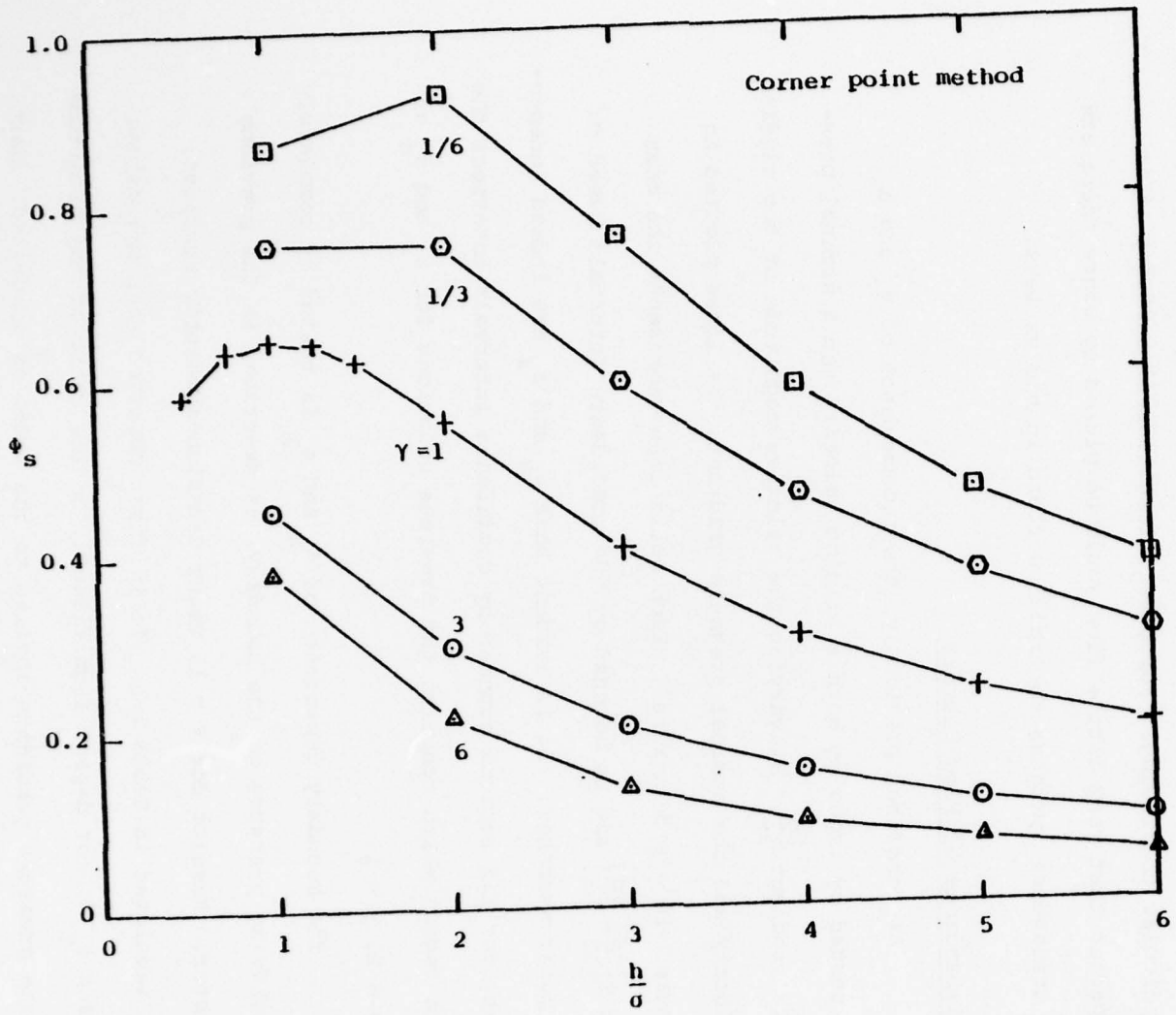

Figure 2-19. Φ_s for Non-isotropic, Gaussian-symmetric Surfaces

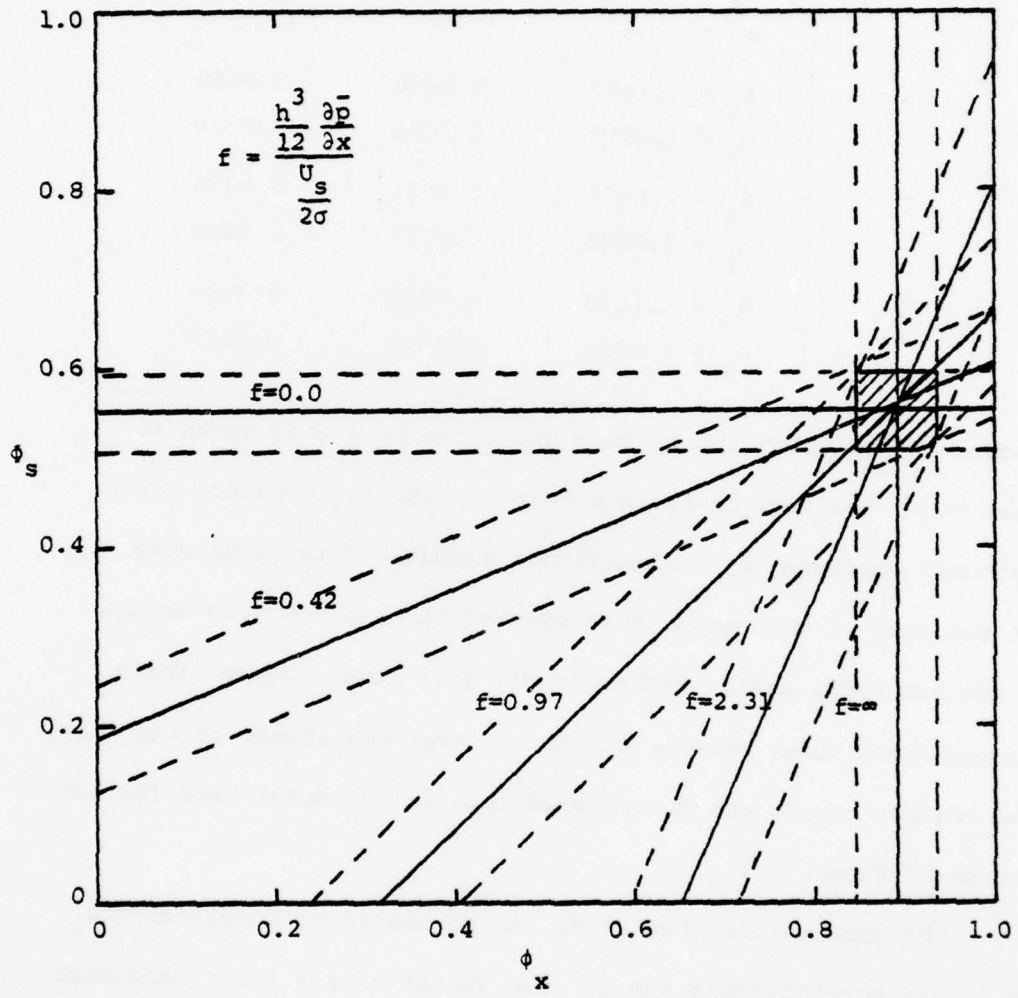

Figure 2-20. Independence of ϕ_x and ϕ_s

Table 2-1. Testing the Boundary Dependence of ϕ_x and ϕ_y. $\gamma = 1$.

$\frac{\partial \bar{p}}{\partial x} / \frac{\partial \bar{p}}{\partial y}$		h/σ 1	2	3
∞	ϕ_x =	1.1400	0.9707	0.9693
	ϕ_y =	-	-	-
3	ϕ_x =	1.1381	0.9650	0.9656
	ϕ_y =	1.0616	0.9091	0.9354
2	ϕ_x =	1.1372	0.9621	0.9638
	ϕ_y =	1.0683	0.9262	0.9464
1	ϕ_x =	1.1138	0.9536	0.9583
	ϕ_y =	1.0751	0.9433	0.9575

However, the solution for ϕ_x does not agree with that given in Figure 2-15. The flow resistance here is less (ϕ_x greater) than previously predicted by a significant amount. This is because when the flow is obstructed by a contact it need not pass around the contact necessarily, rather it may just turn. Hence, these boundary conditions provide a path of lower resistance to the flow when contact points are encountered than in the model used for the results of Figure 2-15.

The explanation just given can be tested by considering ϕ_x and ϕ_y for non-isotropic cases. Two values of $\gamma \neq 1$ are tabulated in Table 2-2. It is verified that $\phi_y(h,\gamma) = \phi_x(h,1/\gamma)$ considering confidence intervals. Comparing the values in Table 2-2 to those presented in Figure 2-17, the flow is everywhere greater in the completely pressure specified boundary case. This reinforces the argument that the pressure flow factors are boundary dependent and

Table 2-2. Boundary Dependence of ϕ_x, ϕ_y for Non-Isotropic Surfaces $\frac{\partial \bar{p}}{\partial x} \Big/ \frac{\partial \bar{p}}{\partial y} = 1$

		h/σ		
γ	1	1.5	2	3
1/3	ϕ_x = 0.6686	0.6548	0.7025	0.8026
	ϕ_y = 1.6289	1.3373	1.2176	1.1139
1	ϕ_x = 1.1138	-	0.9536	0.9583
	ϕ_y = 1.0751	-	0.9433	0.9575
3	ϕ_x = 1.6356	1.3414	1.2209	1.1158
	ϕ_y = 0.8199	0.7569	0.7759	0.8430

must be redetermined for each particular application. Although it is not investigated herein, it is reasonable to assume that ϕ_s is also boundary dependent to an even greater extent than ϕ_x and ϕ_y. Since flow can run down the valleys transversly in this model, less fluid will remain trapped by the transverse ridges.

Flow Factors for Gaussian-Truncated Surfaces

The Gaussian-truncated distribution of roughness heights adds the additional variable r, the truncation level, to the analysis of flow factors. This level is variable because of the possible mating of a surface with higher shear strength to a surface having lower shear strength. The significant truncation level of the weaker surface will possibly be lower than the stronger surface and the probable cross-section area at a given height must be considered to determine r for a pair of surfaces.

Another aspect of truncated surfaces is that asperity deformation is no longer present. This allows the flow factors to be solved

for $h/\sigma < 0.5$, which was a limitation on the average flow model previously. Absence of asperity deformation also means that $E(\delta_1)$ and $E(\delta_2)$ are time and position invariant, lending support to the previous arguments debating the average Reynolds equation techniques.

Before presenting the results for flow factors from truncated distributions it is pointed out that no direct comparison to the symmetric distributions can be made. This is because even with $r = 0.0$, the lower surface (Figure 2-10) possesses valleys which reduce the contact area. If σ_1 is then made 0, a truncated distribution no longer exists and the situation resembles Gaussian-symmetric. Hence, the results to be presented stand alone and can only be compared to previous results qualitatively.

The pressure flow factor ϕ_x for isotropic truncated surfaces having variable r and $\sigma_1 = \sigma_2$ is plotted in Figure 2-21. Values of r from 0 to 0.5 are given only since for $\sigma_1 = \sigma_2$, $\phi_x(h,\gamma,r) = \phi_x(h,\gamma,1-r)$. As r increases to 0.5, flow decreases because the contact increases. Qualitatively, the results resemble those for symmetric surfaces, but the flow resistance is much less due to less contact. It is also true that the average value of H is greater than the symmetric distribution because deformable asperities which would decrease H have been truncated. This explains why a $\gamma = 1$ in this case nearly corresponds to a $\gamma = 2$ or 3 in the previous case of deformable asperities.

The effect of γ on ϕ_x with $r = 0.5$, $\sigma_1 = \sigma_2$ is shown in Figure 2-22. Again, the qualitative behavior is the same as for symmetric surfaces, but the flow resistance is much lower.

Results for the ϕ_s case are much more interesting. The linearity of ϕ_s with σ_1^2 and σ_2^2 proposed by Patir for deformable

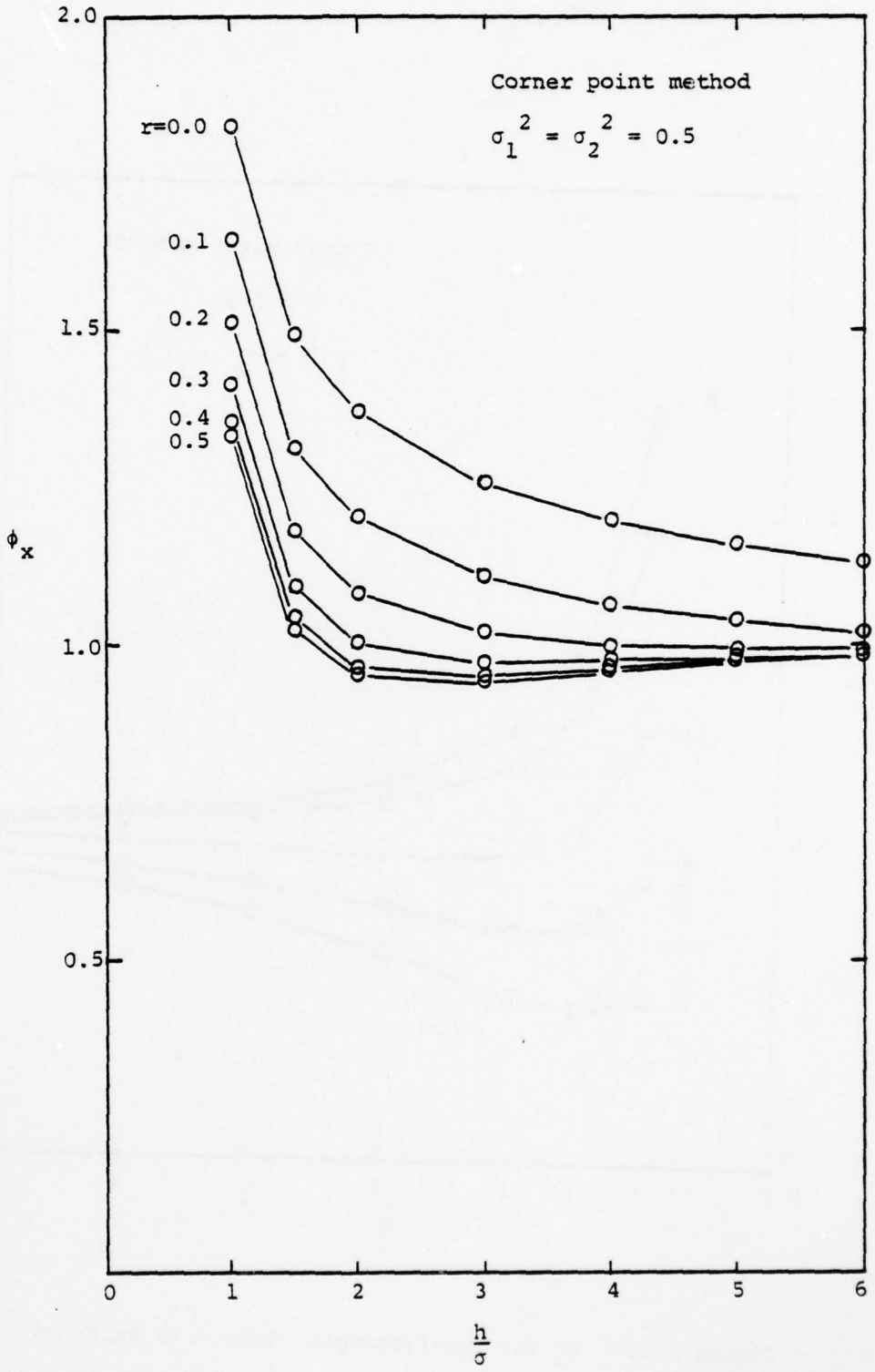

Figure 2-21. ϕ_x for Isotropic, Truncated Surfaces

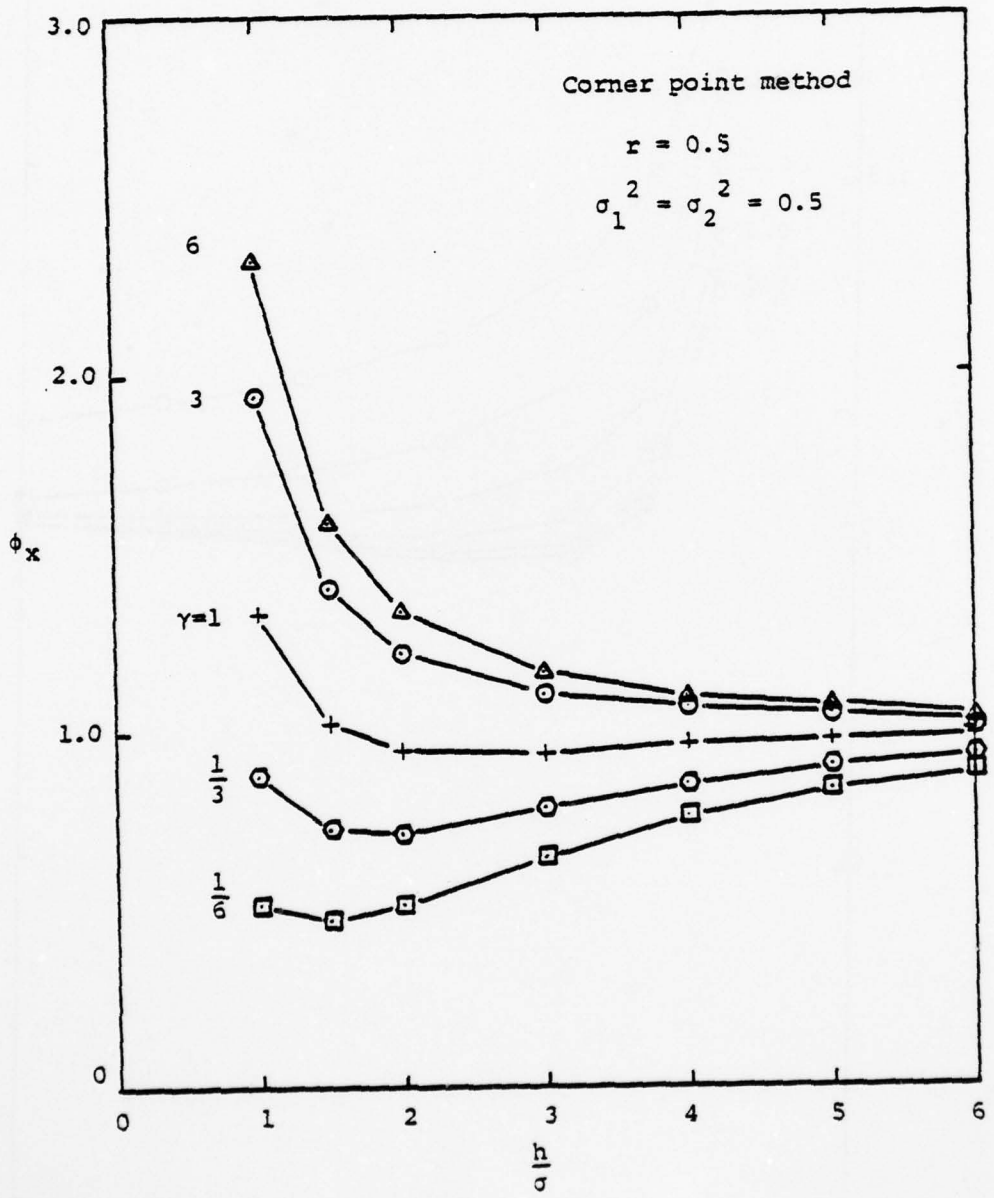

Figure 2-22. ϕ_x for Non-isotropic, Truncated Surfaces

surfaces is no longer valid. To illustrate this a graph of ϕ_s for $\sigma_1 = \sigma_2$ and variable r is shown in Figure 2-23. In the symmetric density function results, ϕ_s was expected to be zero for $\sigma_1 = \sigma_2$. However, this is only true for r = 0.5 in the truncated distribution. Other values of r create valley depths on one surface larger than those on the opposing surface which produces a net shear flow. The curves have the same basic shape as the previous results for ϕ_s, but the magnitude of the flow is much lower for any comparable case. Figure 2-24 shows ϕ_s for fixed r = 0.5 and variable σ_1^2. Again, for $\sigma_1^2 = \sigma_2^2 = 0.5$, no flow is developed. But, as $\sigma_1^2 \rightarrow 0.9$, the valleys on δ_1 become larger than on δ_2 and flow picks up.

Results for ϕ_s using non-isotropic surfaces truncated at r = 0 with $\sigma_1^2 = \sigma_2^2$ are plotted in Figure 2-25. This figure yields no new information since the qualitative trends are consistent with those results of the Gaussian symmetric distribution.

Limitations of the Numerical Formulation

Several error estimates and checks were made on the numerical method. The solution to the finite difference equations was accomplished by successive overrelaxation. Hence, the convergence criteria involved a relative pressure change tolerance τ. Selection of the appropriate value of τ involved a tradeoff between computer time and accuracy of the solution. It was noted previously that ϕ_x could be solved at any value of x, since it should be the same everywhere. Table 2-3 gives typical values of ϕ_x at $x = \Delta x(I = 2)$, $x = L_x - \Delta x(I = N_x - 2)$ and ϕ_x mean for a

AD-A065 924 NEW MEXICO UNIV ALBUQUERQUE BUREAU OF ENGINEERING R--ETC F/G 11/1
HYDRODYNAMIC LUBRICATION WITH WEAR AND ASPERITY CONTACT IN MECH--ETC(U)
JAN 79 A O LEBECK, J L TEALE, R E PIERCE N00014-76-C-0071
UNCLASSIFIED ME-95(79)ONR-414-1 NL

2 OF 2
AD A065924

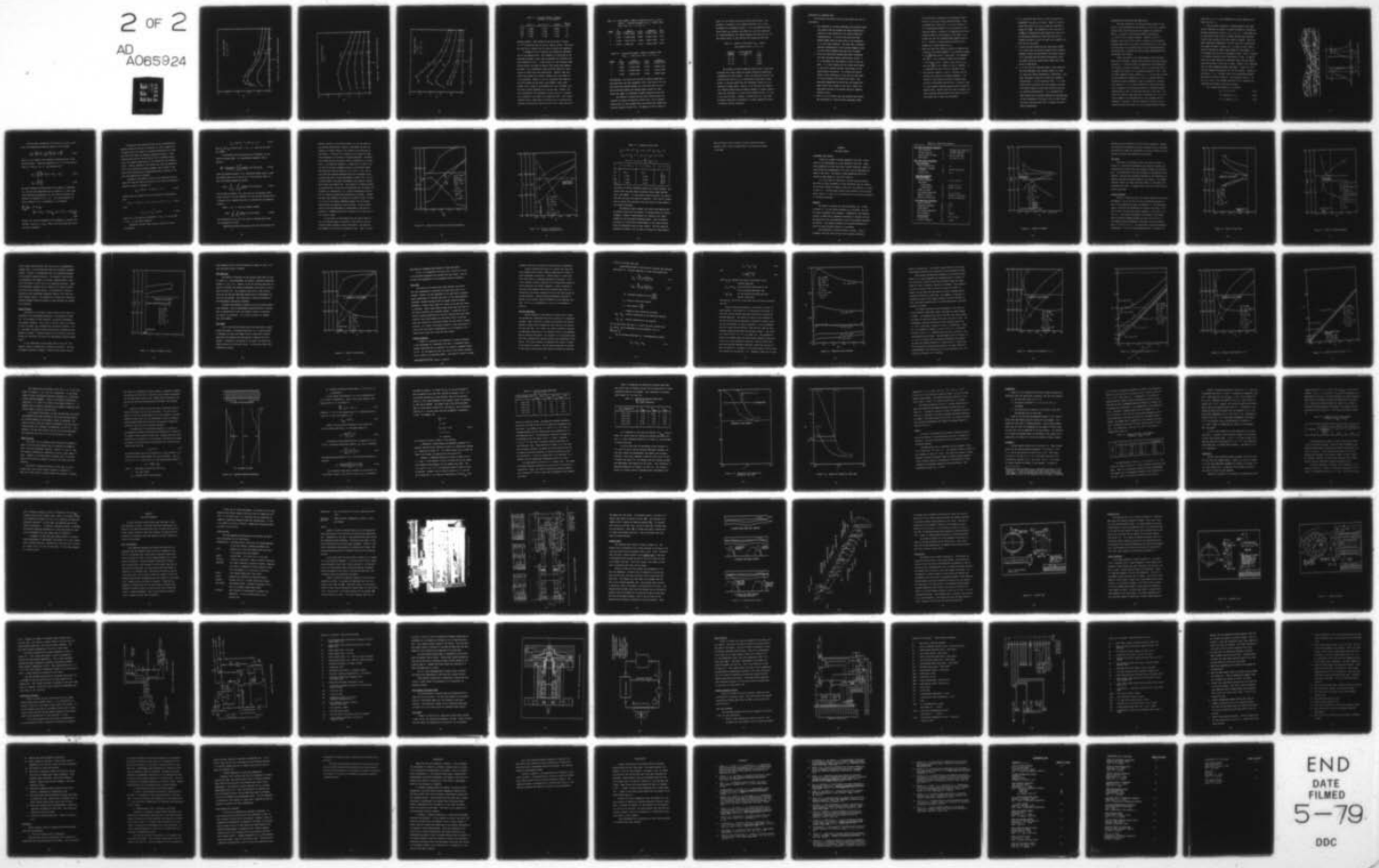

END
DATE FILMED
5-79
DDC

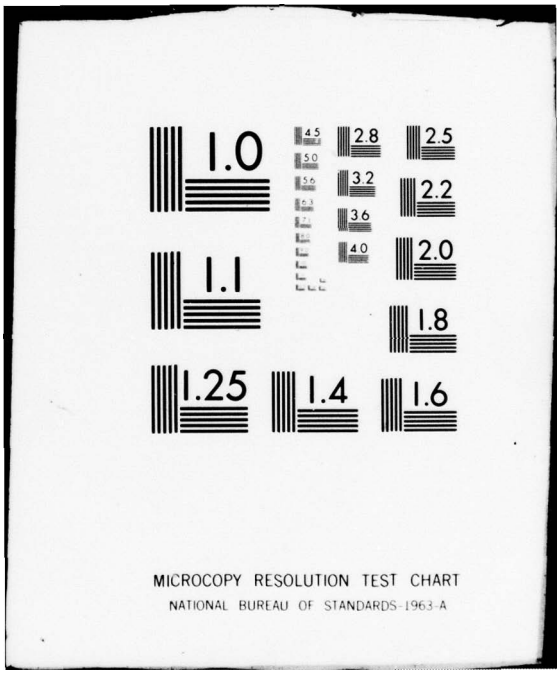
1.0
1.1
1.25
1.4
1.6
1.8
2.0
2.2
2.5
2.8
3.2
3.6
4.0
4.5
5.0
5.6
MICROCOPY RESOLUTION TEST CHART
NATIONAL BUREAU OF STANDARDS-1963-A

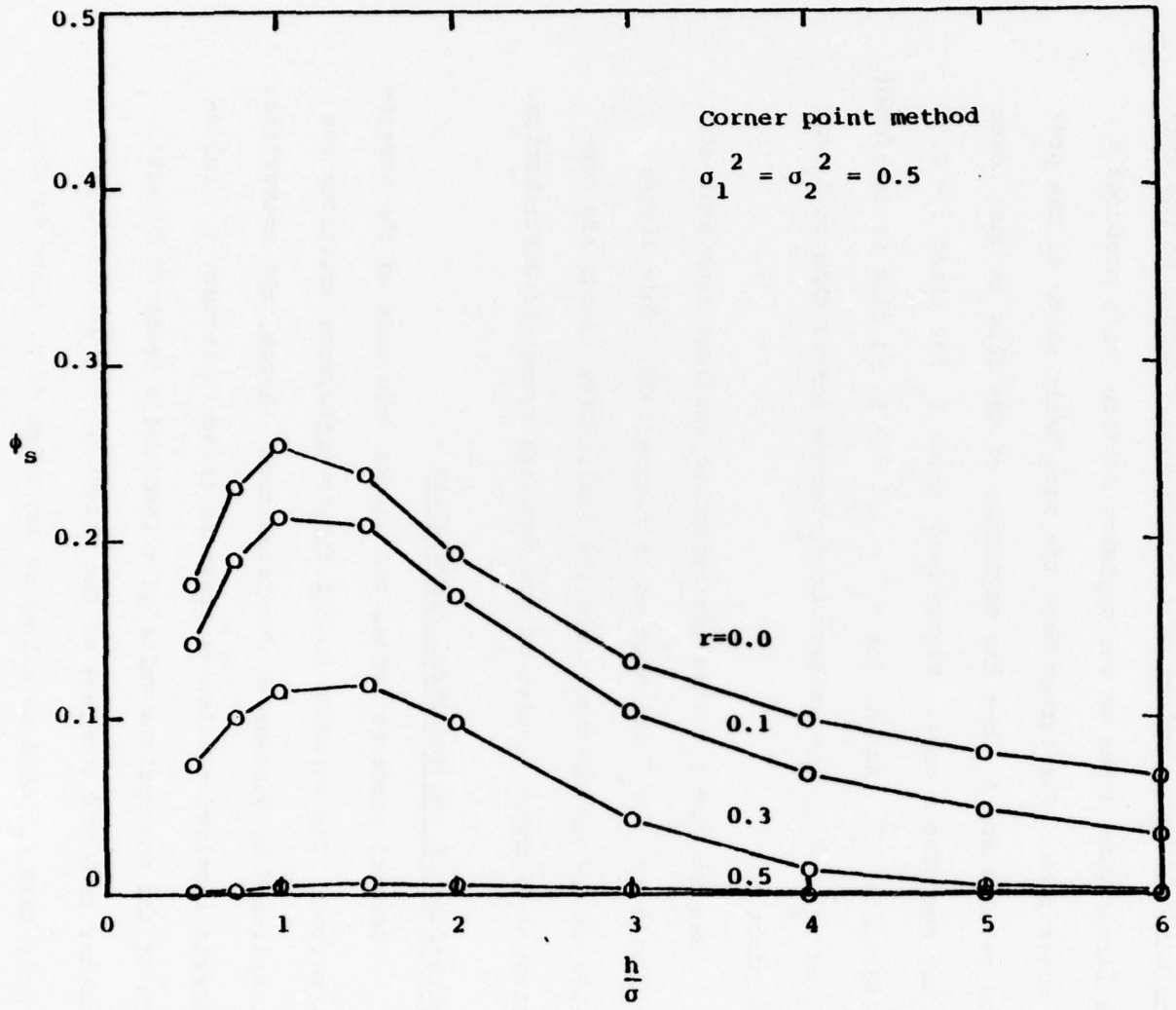

Figure 2-23. ϕ_s for Isotropic, Truncated Surfaces

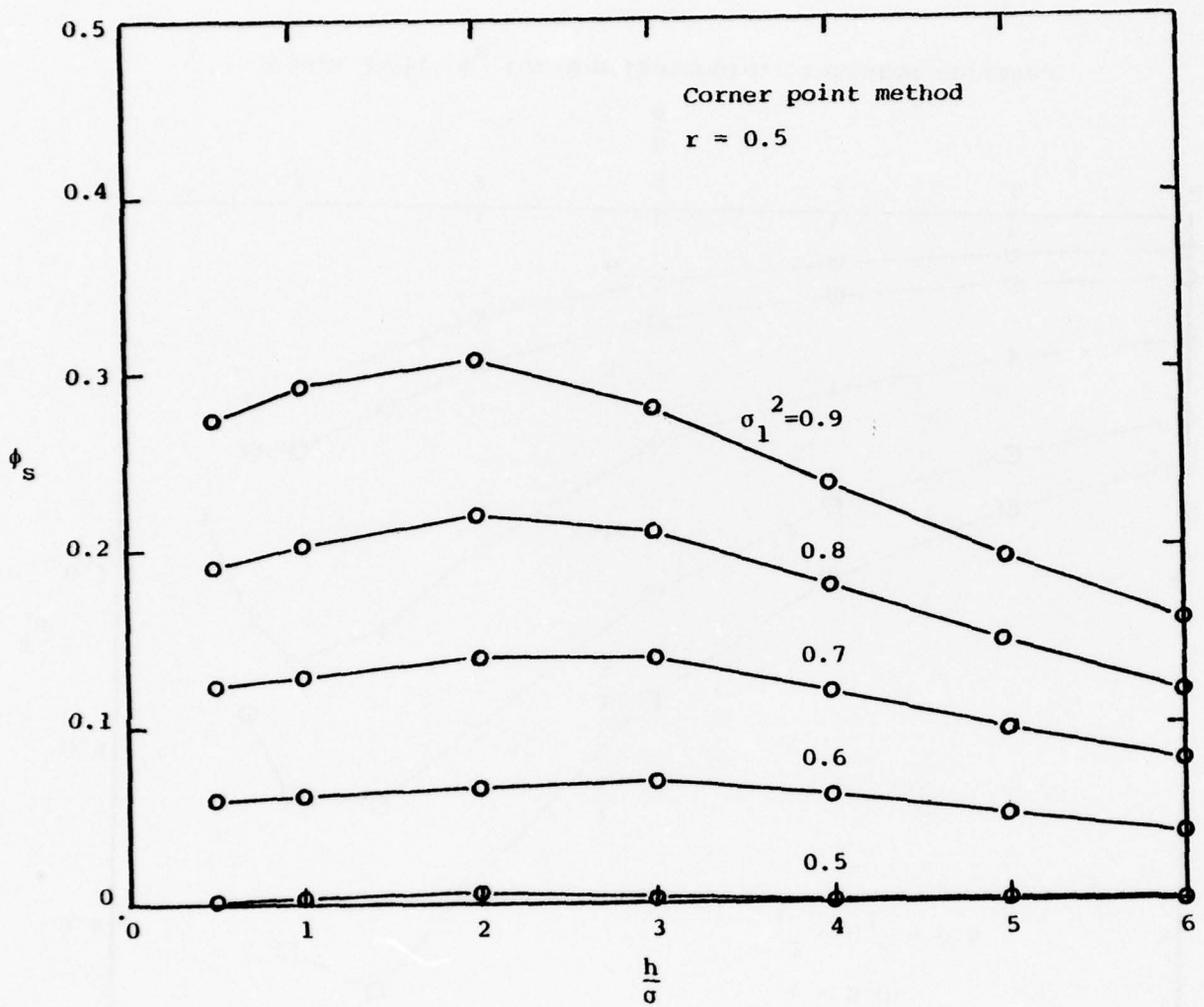

Figure 2-24. Effect of σ_1 on Truncated Surface ϕ_s

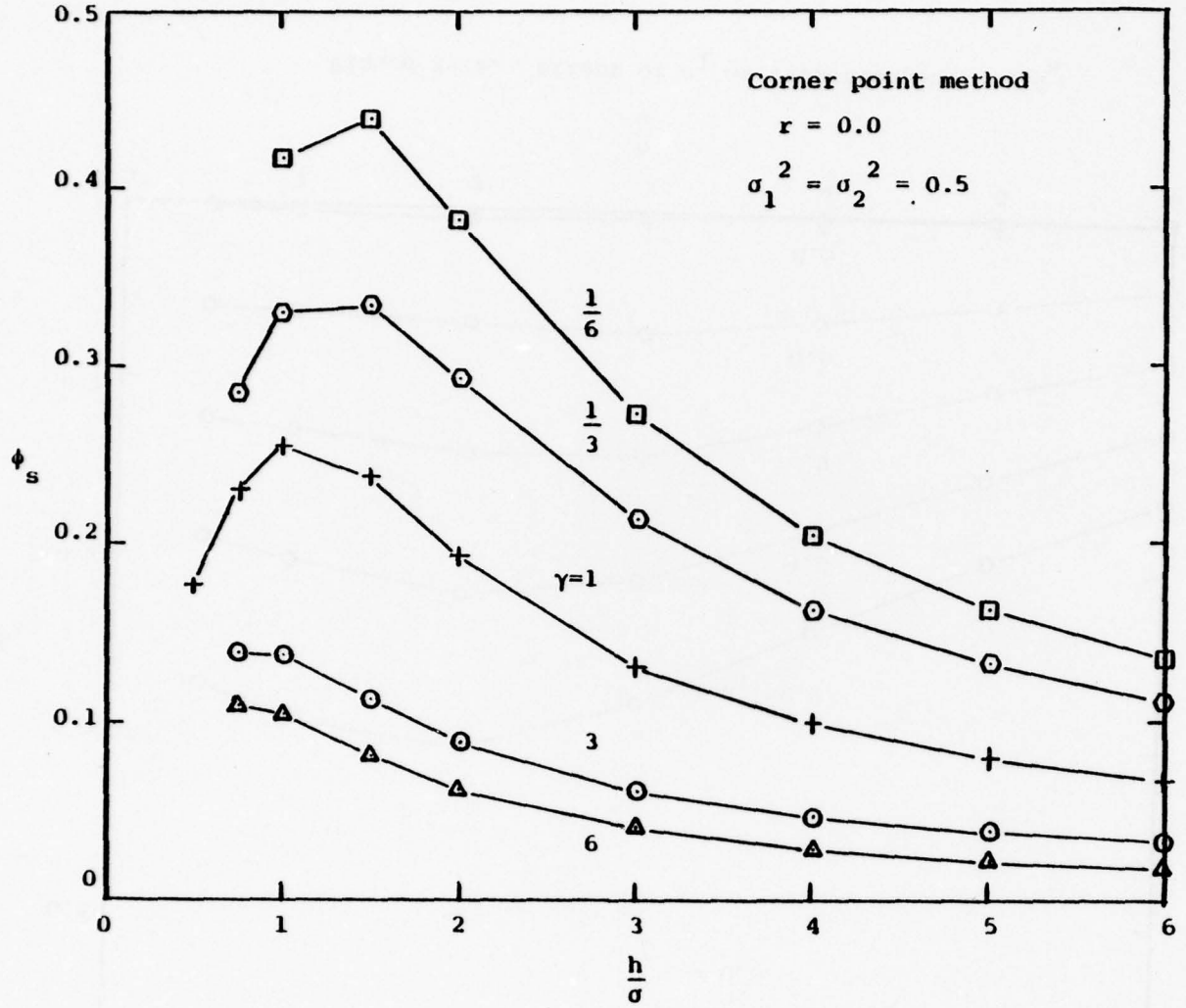

Figure 2-25. ϕ_s for Non-isotropic, Truncated Surfaces

Table 2-3. Accuracy Problem - Necessary Tolerance for Convergence.

τ	$\phi_x \mid I = 2$	$\phi_x \mid I = N_x - 1$	$\phi_x \mid$ mean	IBM 360 CPU
10^{-3}	0.5895	0.9796	0.8500	19
10^{-4}	0.7058	0.7441	0.7305	31
10^{-5}	0.7191	0.7153	0.7177	47
10^{-6}	0.7196	0.7142	0.7172	>56

specific surface. Even though the end values fail to match, $\tau = 10^{-4}$ yields less than 2% error in mean ϕ_x values. This value was used for all results and this error estimate was repeatable.

A different sort of limitation was imposed by consideration of the asperity size. This parameter is controlled by the correlation lengths n and m used to generate the artificial surfaces (Equation (2-66)). Larger values of n and m create larger contact points, but fewer of them so that contact area remains the same. For a sufficiently large grid the values of n and m should not effect the flow significantly. However, when this effect was studied for isotropic surfaces (m=n) the effect on ϕ_x was profound. Tables 2-4 and 2-5 illustrate this study for the Patir method and the corner point method. While there appears to be a trend of $\bar{\phi}_x$ decreasing as n(=m) increases, this was found in some instances not to be the case. However, the trend exhibited by the confidence interval size as it increases with increasing n was found to be always the case. This clearly indicates that a large range of results for ϕ_x is statistically possible by varying the choice of m and n for a fixed grid size.

Table 2-4. Patir Method - Effect of Asperity Size on ϕ_x (Flow Factor), γ (Pattern Parameter) and P_c (Contact Area), Grid is 26 × 26, $\gamma = 1$, $h/\sigma = 1$.

N(=M)	$\bar{\phi}_x$	90% CI	$\bar{\gamma}$	90% CI	$\bar{P}_c$
1	0.6179	0.5671-0.6687	0.9947	0.9693-1.0200	16.00
2	0.5937	0.5186-0.6688	0.9957	0.9455-1.0458	15.97
3	0.5780	0.4401-0.7159	0.9709	0.8807-1.0611	15.96
4	0.5379	0.3299-7459	0.9142	0.8462-0.9822	16.15

Table 2-5. Corner Point Method - Effect of Asperity Size on ϕ_x, γ. Grid is 26 × 26, $\gamma = 1$, $h/\sigma = 1$.

N(=M)	$\bar{\phi}_x$	90% CI	$\bar{\gamma}$	90% CI
1	1.1191	1.0143-1.2238	0.9820	0.9504-1.0135
2	0.8696	0.7786-0.9607	0.9798	0.9082-1.0514
3	0.7963	0.6939-0.8986	0.9772	0.9021-1.0522
4	0.6393	0.4639-0.8147	0.9558	0.8256-1.0861

Unfortunately, this choice was limited by computer space and so the value m=n=2 was used throughout, with a grid size of 26 x 26. This value was selected because it is felt that m=n=1 is not a well-correlated surface and because higher values of m and n reduce the number of correlation lengths contained in the grid.

The effects of varying the grid size yields similar conclusions as varying the asperity contact size. For a constant contact size n,m the increased grid size effectively reduces the relative asperity contact size. An example of this is shown in

Table 2-6, for n=m=2 and using the corner point method. The parameter of interest is the standard deviation of ϕ_x, which determines the confidence interval. It is concluded that large grids reduce σ_{ϕ_x}, however, the effect on ϕ_x was not conclusive. As already mentioned, the largest feasible grid size was 26 × 26. The primary factor in this decision was storage and CPU time.

Table 2-6. Effect of Grid Size on σ_{ϕ_x}. Corner Point Method, N=M(γ = 1), $\bar{h}$ = 1.0.

Grid Size NXXNY	Points Averaged NAV	σ_{ϕ_x}
10 × 10	20	0.5166
20 × 20	17	0.3477
30 × 30	17	0.2837
40 × 40	14	0.1418

The studies of relative asperity contact size to grid size indicated that larger grids with longer correlation lengths are recommended for three reasons. First, the asperity size will not influence the value of ϕ_x if a sufficiently large grid is used. Second, it has been shown that the confidence interval on ϕ_x is reduced for larger grids. Finally, it is felt that the lubrication behavior would be more accurately modeled if several pressure nodes were contained in a given contact instead of only 3 or 4 as is the case for m=n=2. However, a network with 100 × 100 nodes and n=m=10 would only be feasible on a larger computer and using a different solution technique.

CONCLUSIONS ON ROUGHNESS MODEL

The following conclusions have been made based upon this investigation.

1. The selection of a finite difference grid network alters the results from the average flow model significantly. Implicit in this selection is the contact shape and characteristics. It is felt that since the Patir method element does not block flow in two directions, it is not a good selection. The fact that a different physical interpretation of the contact geometry alters the flow factor suggests that more work is needed.
2. Since the corner point method used herein intersects the Patir and Elrod results statistically for $\frac{h}{\sigma} > 3$, it is concluded that this method is valid in this regime. It is also thought that the corner point method is only one of several possibly valid models of the rough surface lubrication. The corner point method offers a lower resistance to flow than the Patir method so that pressure flow factors are larger. This conclusion emphasizes the point that the average flow model should not be taken at face value, rather the lubrication problem to be modeled should be examined carefully first.
3. While it is not evident that the pressure flow factors are continuous in γ from the Patir published curves,

this continuity is observed to be necessary by definition of ϕ_x and the results presented herein. Since ϕ_x becomes very large for $\frac{h}{\sigma} < 0.5$ at all values of γ, it is questionable whether or not any results in this range are usable. Although it is admitted that the deformation model is not accurate in this range, it is pointed out that the truncated model remains valid as $\frac{h}{\sigma} \to 0$. However, in either case the question still stands due to large scatter of ϕ_x.

4. While the shear flow factor ϕ_s exists to preserve continuity in the bearing segment, it is uncertain whether or not $\frac{\partial \phi_s}{\partial x}$ should exist in some cases. The arguments that $\frac{\partial \phi_s}{\partial x} = 0$ for a truncated surface are presented in the second section. However, later results indicate that $\frac{\partial \phi_s}{\partial h} \neq 0$ for constant δ_1 and δ_2 surfaces. It is suggested that this could be a boundary effect.

5. The results of Tables 2-1 and 2-2 indicate that the pressure flow factors are boundary dependent. Suppression of the nominal y-direction leakage rarely occurs as in the model used by Patir. Typically there is a zero nominal pressure gradient applied across the bearing width. Results from this type of boundary condition indicate higher pressure flow factors than the Patir model due to lower flow resistance.

6. It is concluded from Figure 2-20 that the implied independence of ϕ_x and ϕ_s is valid. Hence it is ascertained that both the ϕ_x and ϕ_s terms are required to expand $E\left(-H^3 \frac{\partial p}{\partial x}\right)$. The expansion of this term when H^3 and $\frac{\partial p}{\partial x}$ are correlated has been debated for years, and the hypothesis proposed by Cheng and Patir for deformable surfaces is valid at least for an element with zero flow at the edges.

7. In both the Patir method and the corner point method it is found that the relative contact size to bearing dimension alters the quantitative flow factor results. It is concluded that the results presented by Patir and herein should be checked using larger grid sizes prior to application.

8. It is felt that the truncated model is more realistic than the deformable rough surface concept, at least for cases when elastic deformation is negligible. This model necessarily requires the additional parameter specification r, or the truncation level. It is also evident from the results that both pressure and shear flow factors depend on individual surface statistics for truncated distributions. It is concluded from these results that truncated surfaces are characterized by less resistance to flow due in part to less contact and also to the fact that $E(H^3)$ is greater for truncated distributions.

SIGNIFICANCE FOR ROUGH WAVY SEAL LUBRICATION

The model developed in the previous annual report [1] was based on the Christensen [20] and Tonder [21] result for isotropic surfaces where the moving surface was assumed to be perfectly smooth. In essence, Christensen and Tonder indicate that $\phi_x = E(H^3)/h^3$ for isotropic roughness. However, $E(H^3)/h^3 > 1$. Comparing this result to the curves in Figure 2-15 for isotropic roughness shows that the ϕ_x used in the previous work is too large. Flow resistance in the previous work is larger than predicted by the present work; therefore the previous model underestimates the hydrodynamic load support.

Before the amount of the underestimate can be calculated based on the new model, certain other features of the model require evaluation. In the Patir-Cheng [6] approach the much debated but real factor ϕ_s has been introduced. Now ϕ_s is significant only if it changes with respect to x, according to Equation (2-40). Also, for equal roughness on both surfaces $\phi_s = 0$. For the sake of avoiding the problem of interpreting ϕ_s, let it be assumed that both surfaces have equal roughness or that the roughness is constant with respect to x. It is quite reasonable to assume that roughness is constant on the moving face and has a truncated Gaussian character due to wear. On the fixed wavy face of the seal, it is likely that there is some variation of roughness with x, but this can be assumed to be negligible,and it can be assumed that the roughness is truncated. Finally, inspection of Figure 2-15 for Gaussian surfaces and Figure 2-21 for truncated Gaussian surfaces

shows that $\phi_x = 1$ is a good assumption for equal roughness surfaces with $h/\sigma > 2$.

From the above discussion it becomes apparent that under certain conditions the effect of surface roughness on lubrication becomes insignificant, that is, $\phi_x = 1$, $\phi_s = 0$. A valid model can be constructed without having to answer the many open questions raised in the analysis of the Patir Cheng [6] method. Using the above simplifying assumptions, the wavy rough seal configuration must appear as shown in Figure 2-26. In order to have a finite region of mechanical contact (when needed for load support), it is necessary that the wave be flattened as shown. This is required if a constant truncation level distribution is used. In reality there may be some variation in truncation level near the contact region particularly if the wave is fixed. However, for a traveling wave the above assumption appears reasonable. Figure 2-26 also shows the assumed distributions for the two surfaces. Contact occurs when $h = 2\ t_r$. The mean value of the untruncated Gaussian distribution is used to define h. The truncation level, t_r as well as σ_1 and σ_2, the standard deviations of the roughness distributions are variables that must be chosen.

For a cosine wave function, h is given by

$$h_z = h_o + h_n \cos n\theta \tag{2-93}$$

$$h = h_z \text{ when } h_z \geq 2\ t_r \tag{2-94}$$

$$h = 2\ tr \text{ when } h_z < 2\ t_r \tag{2-95}$$

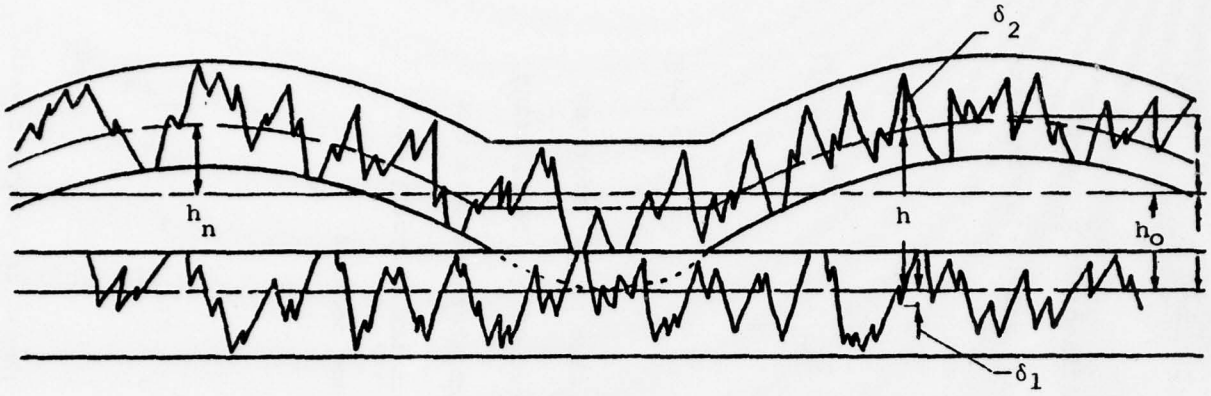

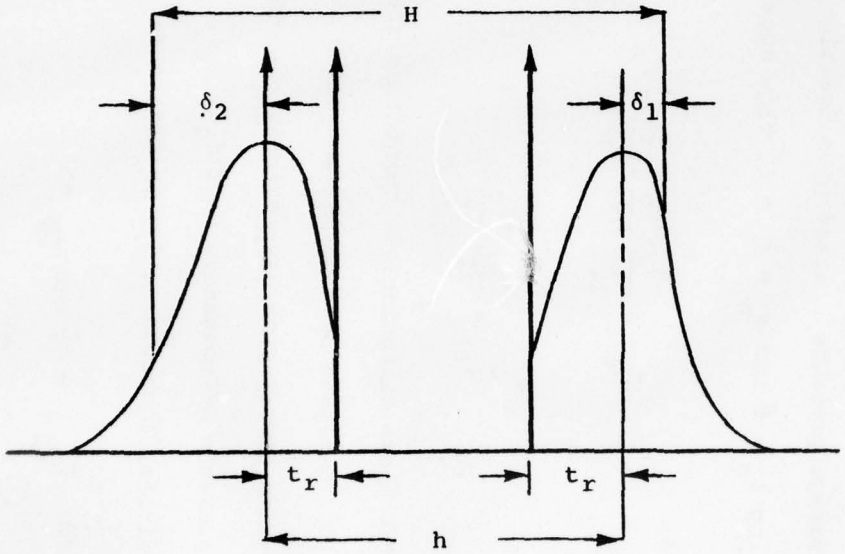

Figure 2-26. Truncated Roughness Model

With the above assumptions and converting to polar coordinates, the dimensionless Reynolds equation (2-40) becomes

$$\frac{1}{\bar{r}} \frac{\partial}{\partial \theta} \left(\frac{\partial \bar{p}_\sigma}{\partial \theta} \bar{h}_\sigma^3 \right) + \frac{\partial}{\partial \bar{r}} \left(\bar{r} \frac{\partial \bar{p}_\sigma}{\partial \bar{r}} \bar{h}_\sigma^3 \right) = 6\bar{r} \frac{\partial \bar{h}_\sigma}{\partial \theta} \tag{2-96}$$

where $\bar{h}_\sigma$ is the nominal film thickness as defined and $\bar{p}_\sigma$ is the average pressure. Based upon Equations (2-37) and (2-38) and letting $\phi_s = 0$ and $\phi_x = \phi_y = 1$, flow equations are

$$\bar{q}_{\theta\sigma} = \frac{-\bar{h}_\sigma^3}{12\bar{r}} \frac{\partial \bar{p}_\sigma}{\partial \theta} + \frac{\bar{r}}{2}[\bar{h}_\sigma + E(\bar{\delta}_{1\sigma} + \bar{\delta}_{2\sigma})] \tag{2-97}$$

$$\bar{q}_{r\sigma} = \frac{-\bar{h}_\sigma^3}{12} \frac{\partial \bar{p}_\sigma}{\partial \bar{r}} \tag{2-98}$$

The above dimensionless quantities are the same as in Reference [1], but have been normalized using σ instead of c. Thus, using these simplifying assumptions, the only term that reflects the presence of roughness is $E(\delta_1 + \delta_2)$. The cavity boundary condition, Equation (2-37) in Reference [1], now becomes

$$\left.\frac{\partial \bar{p}}{\partial \bar{h}}\right|_{②} \bar{h}_{②\sigma}^3 = 6\bar{r} \cos \alpha_{②} \times \left[\left(\bar{h}_\sigma + E(\bar{\delta}_{1\sigma}) + E(\bar{\delta}_{2\sigma}) \right)_{②} - \left(\bar{h}_\sigma + E(\bar{\delta}_{1\sigma}) + E(\bar{\delta}_{2\sigma}) \right)_{①} \right] \tag{2-99}$$

However, for the given assumption that roughness is constant with position, the $E(\delta_{1\sigma}) + E(\delta_{2\sigma})$ terms on the right hand side cancel and vanish completely.

The previous four equations along with the straightforward boundary conditions outlined in Reference [1] form a complete set of equations for the solution for pressure distribution for rough wavy seal faces under the roughness assumption outlined. These equations show that for this particular set of roughness assumptions, the pressure distribution is not affected by the roughness itself. However, mechanical load support and fluid and mechanical friction are affected by surface roughness, and a method of computing these factors must be established before a solution to the wavy seal problem can be obtained.

Mechanical load support is given by the probability of two asperities touching times the total face area times the compressive strength, similar to reference [1].

$$p_{m_a} = p_m P[(\delta_2 < t_r) \text{ and } (\delta_1 < t_r)] \tag{2-100}$$

Assuming that the roughness on the two surfaces is uncorrelated, then

$$P[(\delta_2 < t_r) \text{ and } (\delta_1 < t_r)] = P(\delta_2 < t_r) \times P(\delta_1 < t_r) \tag{2-101}$$

where

$$P(\delta_1 < tr) = \int_{-\infty}^{-t_r} f(\delta)\,d\delta \tag{2-102}$$

where $f(\delta)$ is the Gaussian distribution. $P(\delta_2 < t_r)$ is the same as $P(\delta_1 < t_r)$ for equal roughness.

Mechanical friction shear stress is given by a similar relationship.

$$p_{s_a} = p_s P[(\delta_2 < t_r) \text{ and } (\delta_1 < t_r)] \qquad (2\text{-}103)$$

Both p_{m_a} and p_{s_a} are zero when $h > 2t_r$, i.e., when the seal does not contact.

To calculate fluid film friction as in Reference [1] one needs to evaluate $E(\frac{1}{H})$. For uncorrelated roughness, this is given by

$$E(\frac{1}{H}) = E\left(\frac{1}{h+\delta_1+\delta_2}\right) = \int_{-\infty}^{\infty}\int_{-\infty}^{\infty} \frac{1}{h+\delta_1+\delta_2} f(\delta_1) f(\delta_2) d\delta_1 d\delta_2 \qquad (2\text{-}104)$$

Under the condition where $h = 2t_r$, then $\frac{1}{H}$ can become large, so that the minimum value of H is set at Δ as in the previous report [1]. Then the integral appears as follows:

$$E(\frac{1}{H}) = \int_{-t_r+\frac{\Delta}{2}}^{\infty} \int_{-t_r+\frac{\Delta}{2}}^{\infty} \frac{1}{h+\delta_1+\delta_2} f(\delta_1)\delta(\delta_2) d\delta_1 d\delta_2 \qquad (2\text{-}105)$$

For this case of contact, $f(\delta_1)$ and $f(\delta_2)$ are the Gaussian distribution functions, and the probability of the combined impulses shown in Figure 2-26 is ignored since this is accounted for by mechanical friction.

When $h > 2t_r + \Delta$, then the integral becomes

$$E(\frac{1}{H}) = \int_{-t_r}^{\infty} \int_{-t_r}^{\infty} \frac{1}{h+\delta_1+\delta_2} f(\delta_1) f(\delta_2) d\delta_1 d\delta_2 \qquad (2\text{-}106)$$

and the impulses on $f(\delta_1)$ and $f(\delta_2)$ must be included since there is no mechanical friction.

Combining the above relationships and

methods outlined in the previous report [1], one can solve for the pressure distribution, friction, and leakage for this new problem in a manner similar to the problem of the previous annual report. In Figure 2-27 a typical set of results is shown for performance as a function of waviness amplitude. The parameter values used are the same as those in Reference [1] for base case 2. The combined roughness σ is taken as 1/3 c where c was one half of the total roughness height in the previous report. The truncation level was taken at 1.5 σ_1 or $\overline{t_r}$ = 1.06. The results for the truncated roughness model can be compared to the original base case 2 results reproduced as Figure 2-28. For the truncated model, the percent hydrodynamic load support increases more rapidly and reaches 100%. This behavior is expected because as stated earlier, the use of the Christensen [20] and Tonder [21] assumption is conservative, i.e., greater hydrodynamic load support is actually achieved than predicted by this model. Leakage and mean film thickness are plotted as divided by three in Figure 2-27 so as to be directly comparable between the two figures. These results are similar for the two models. Friction coefficient for the truncated model is significantly lower and was plotted on a different scale than in Figure 2-28 so that this effect could be shown.

At this point it would appear that the results based on the two different models are similar in most ways but that the truncated model provides a larger load support. One question that remains is the choice of truncation level. Table 2-7 shows

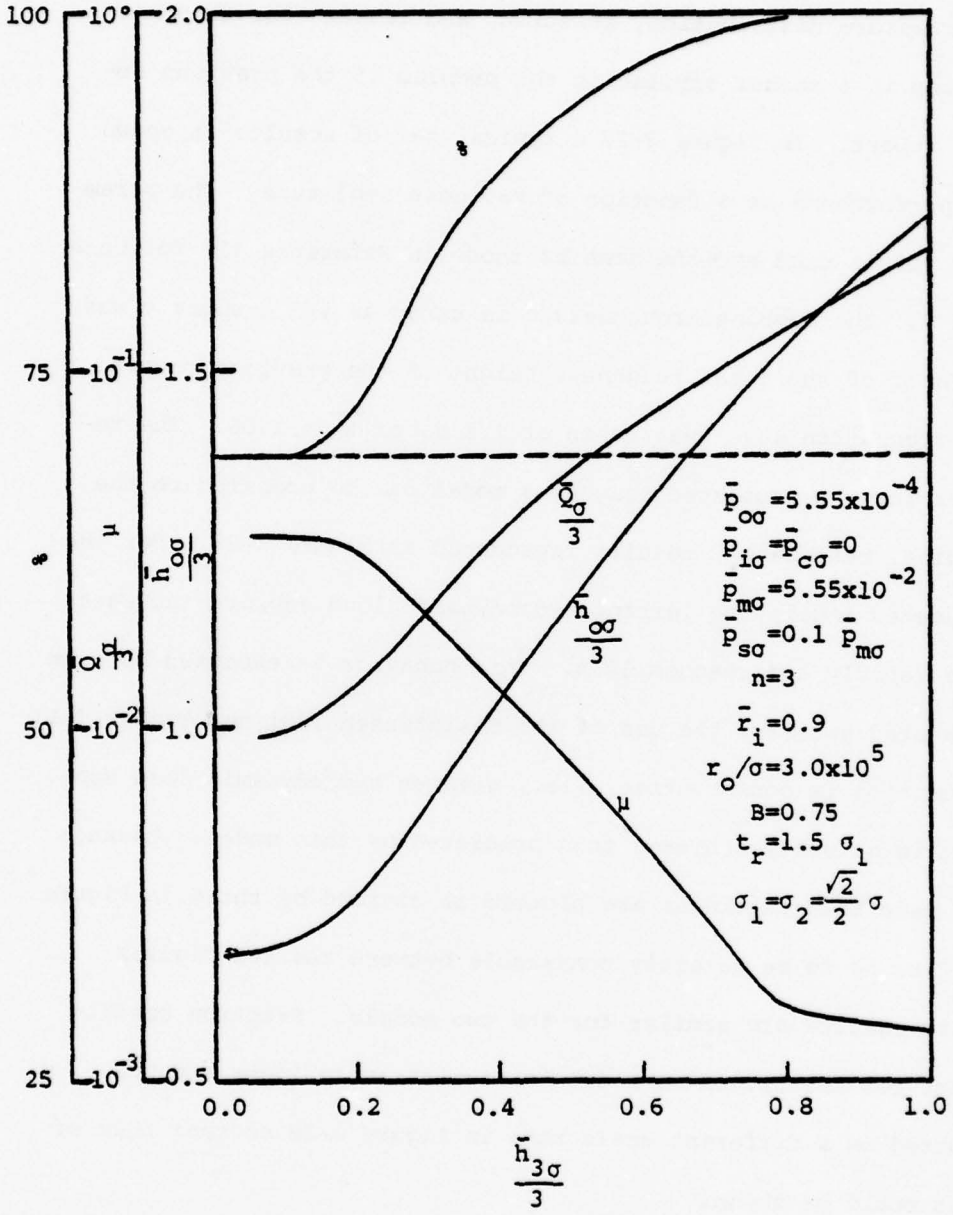

Figure 2-27. Effect of Net Waviness--Truncated Roughness

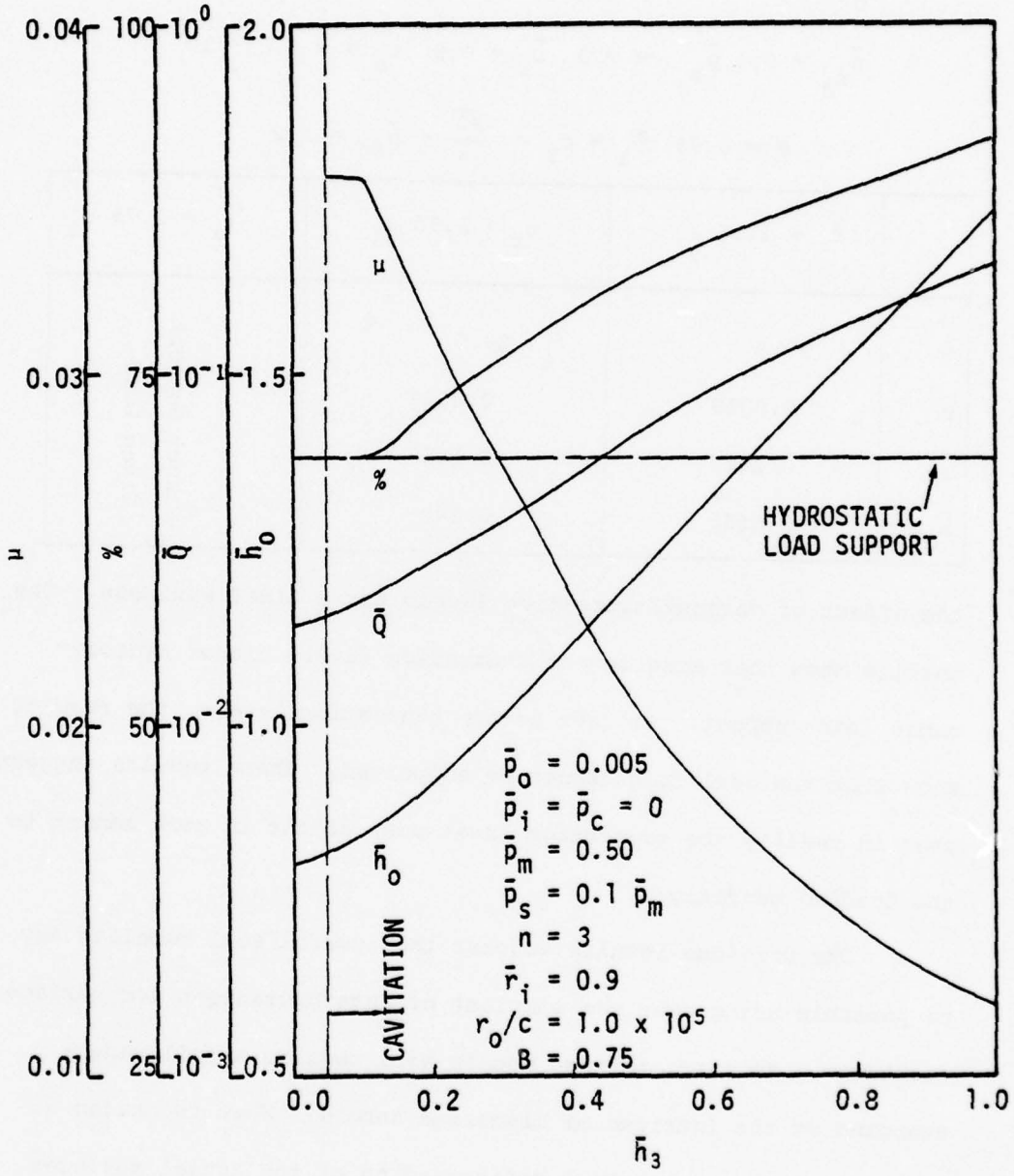

Figure 2-28. Effect of Net Waviness - Isotropic Roughness Case 2

Table 2-7. Truncation Level Study

$\bar{p}_{o_\sigma} = 5.55 \times 10^{-4}$ $\bar{p}_{m_\sigma} = 5.55 \times 10^{-2}$ $\bar{p}_{i_\sigma} = \bar{p}_{c_\sigma} = 0.0$

$\bar{p}_{s_\sigma} = 0.1\ \bar{p}_{m_\sigma}$ $n = 3$ $\bar{r}_i = 0.9$ $r_o/\sigma = 3.0 \times 10^5$

$B = 0.75$ $\sigma_1 = \sigma_2 = \frac{\sqrt{2}}{2}\sigma$ $\bar{h}_{3\sigma} = 1.2$

	$t_r = 1.25\ \sigma_1$	$t_r = 1.50\ \sigma_1$	$t_r = 1.75\ \sigma_1$
%	99.8	89.5	Cannot Support Given Load
μ	0.0019	0.0124	
$\bar{Q}_\sigma$	0.1022	0.1066	
$\bar{h}_{o_\sigma}$	3.0555	3.140	

the effect of various truncation levels for a fixed waviness. The results show that more severe truncation favors higher hydrodynamic load support. At less severe truncation levels, the results show that the seal ring cannot be supported. These results suggest that in reality the truncation level must adjust in some manner to the loading conditions.

The previous results suggest that useful seal modeling may be possible using even the simplest of interpretations for surface roughness. However, refined models will require a full understanding of the intricacies discussed herein. What is needed at this point is a much better understanding of the actual surfaces which are developed during the wear process. The test apparatus described in Chapter 4 will be used to further this understanding.

When the nature of worn surfaces is better understood experimentally, then a better interpretation of the preceding results can be made.

CHAPTER 3

WAVY SEAL DESIGN

PARAMETER STUDY RESULTS

There are a number of design parameters that have a direct effect on the performance of a wavy mechanical face seal. Among these parameters are seal face width, surface roughness, number of waves around the circumference of the seal, and the amplitude and shape of the waves. The values of these parameters may be controlled to some degree by a face seal designer.

As a first step in developing a rational design procedure, the effect of these parameters on seal performance must be studied. The following studies are based on base case 2 of Reference [1] shown in Table 3-1. Although these results were presented in the previous annual report [1], they will be reviewed here to facilitate discussion of the design procedure.

Pressure

The effect of changing the outside pressure, $\bar{p}_o$, is shown in Figure 3-1. As the outside pressure $\bar{p}_o$ is increased, the load that must be balanced also increases. Consequently, more asperity contact is needed and $\bar{h}_o$ decreases accordingly to balance the load. The fraction of the load supported by fluid film pressure decreases accordingly. The leakage increases with increasing pressure because the radial pressure gradient is increasing.

The coefficient of friction remains constant. As $\bar{p}_o$ is increased, the total fluid friction force remains essentially

Table 3-1. Base Case Parameters

FACE SEAL APPLICATION PARAMETERS		
Fluid Viscosity	η	3.05×10^{-4} Pa·s (93°C H_2O) (6.37×10^{-6} lb·s/ft^2)
Outside Pressure	p_o	2.87 MPa (416 psi)
Angular Speed of Shaft	ω	188 r/s (1800 rpm)
Mean Radius	r_c	47.54 mm (1.87 in.)
FACE SEAL DESIGN PARAMETERS		
Fixed Parameters		
Ring Stiffness Ratio	A	6.0
Compressive Strength of Carbon	p_m	250 MPa (36000 psi)
Balance Ratio	B	0.75
Variable Parameters (Base Case Shown)		
Surface Roughness	c	0.5 µm (20 µin.)
Face Width		
Inside Radius	r_i	45 mm (1.77 in.)
Outside Radius	r_o	50 mm (1.97 in.)
Number of Waves	n	3
Net Waviness Amplitude	h_3	0.1 µm (4 µin.)
Moment of Inertia	I_x	4830 mm^4 (0.0116 in.^{4})
Modulus of Elasticity	E	21 GPa (3.0×10^6 psi)
Non-Dimensional Parameters		
Outside Pressure	$\bar{p}_o$	0.005
Compressive Strength	$\bar{p}_m$	0.50
Inside Radius	$\bar{r}_i$	0.9
Net Waviness Amplitude	$\bar{h}_3$	0.2
Ring Stiffness	$\bar{K}$	2.5×10^{-7}
Shear Strength of Asperities	$\bar{p}_s$	0.05 (0.1 $\bar{p}_m$)
Friction Parameter	r_o/c	1.0×10^5

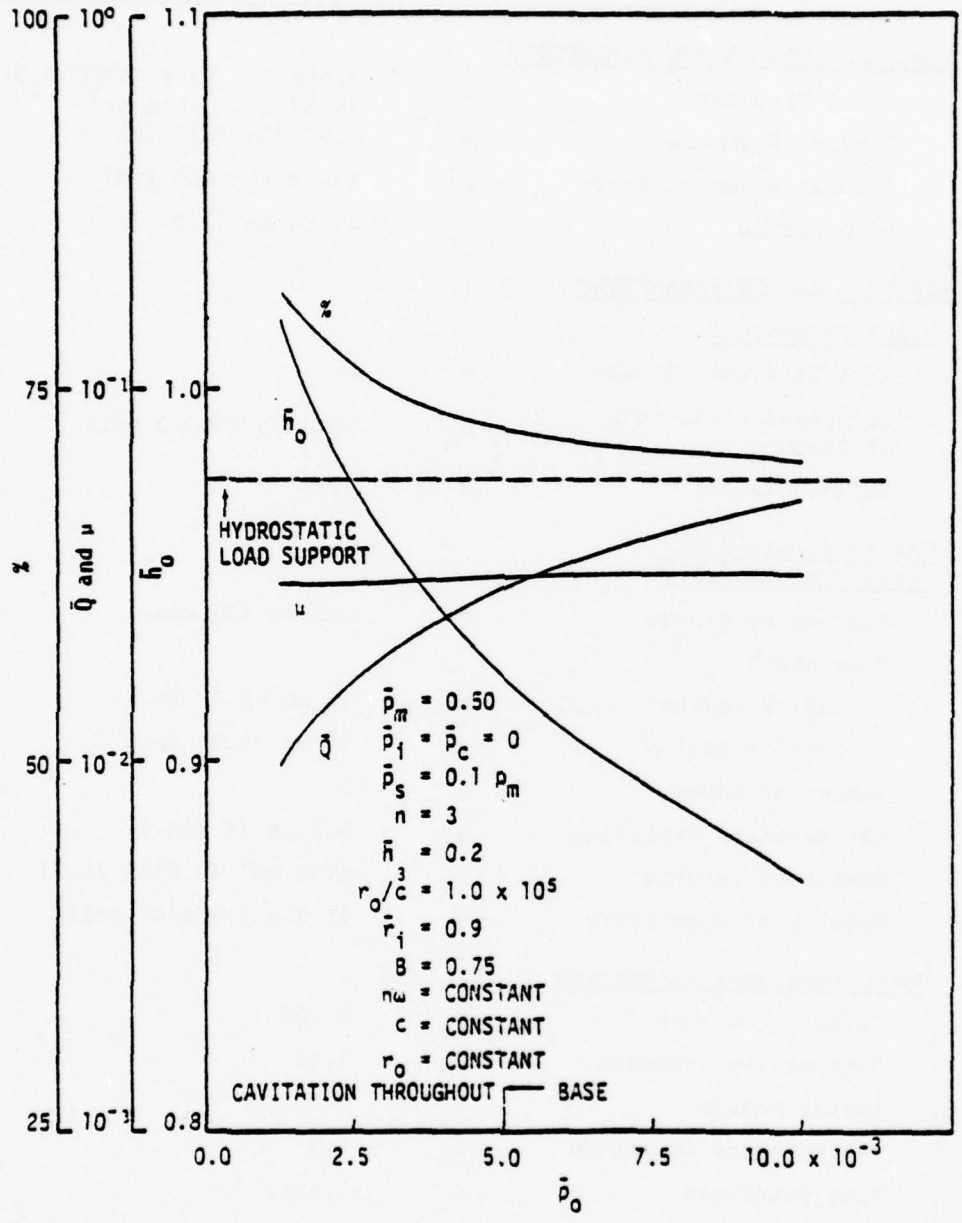

Figure 3-1. Effect of Pressure

constant and the coefficient of fluid friction decreases. However, the coefficient of mechanical friction increases as $\bar{p}_o$ is increased. The addition of these two coefficients of friction results in an essentially constant total coefficient of friction.

Face Width

The results of changing the seal face width are shown in Figure 3-2. The percent hydrodynamic load support increases with increasing face width as more area becomes available for load support. The coefficient of friction decreases as hydrodynamic action improves. The mean film thickness increases as less penetration is needed to develop the required asperity load support. The leakage decreases because the radial pressure gradient is decreasing with increasing face width. It appears that a seal with a wide face has several advantages.

Surface Roughness

Figure 3-3 shows the effect of surface roughness on face seal performance. Due to the fact that the non-dimensionalization of many of the parameters involves the parameter "c," the dimensional values of the base case parameters are shown on the figure. Cavitation occurs only when the surface roughness is less than 1.0 μm (40 μin.). The percent hydrodynamic load support rises sharply when the surface roughness becomes less than 0.64 μm (25 μin.). One hundred percent hydrodynamic load support would be expected when c = 0.33 μm (13 μin.). The coefficient of friction decreases considerably. Due to the non-dimensionalization of leakage, the

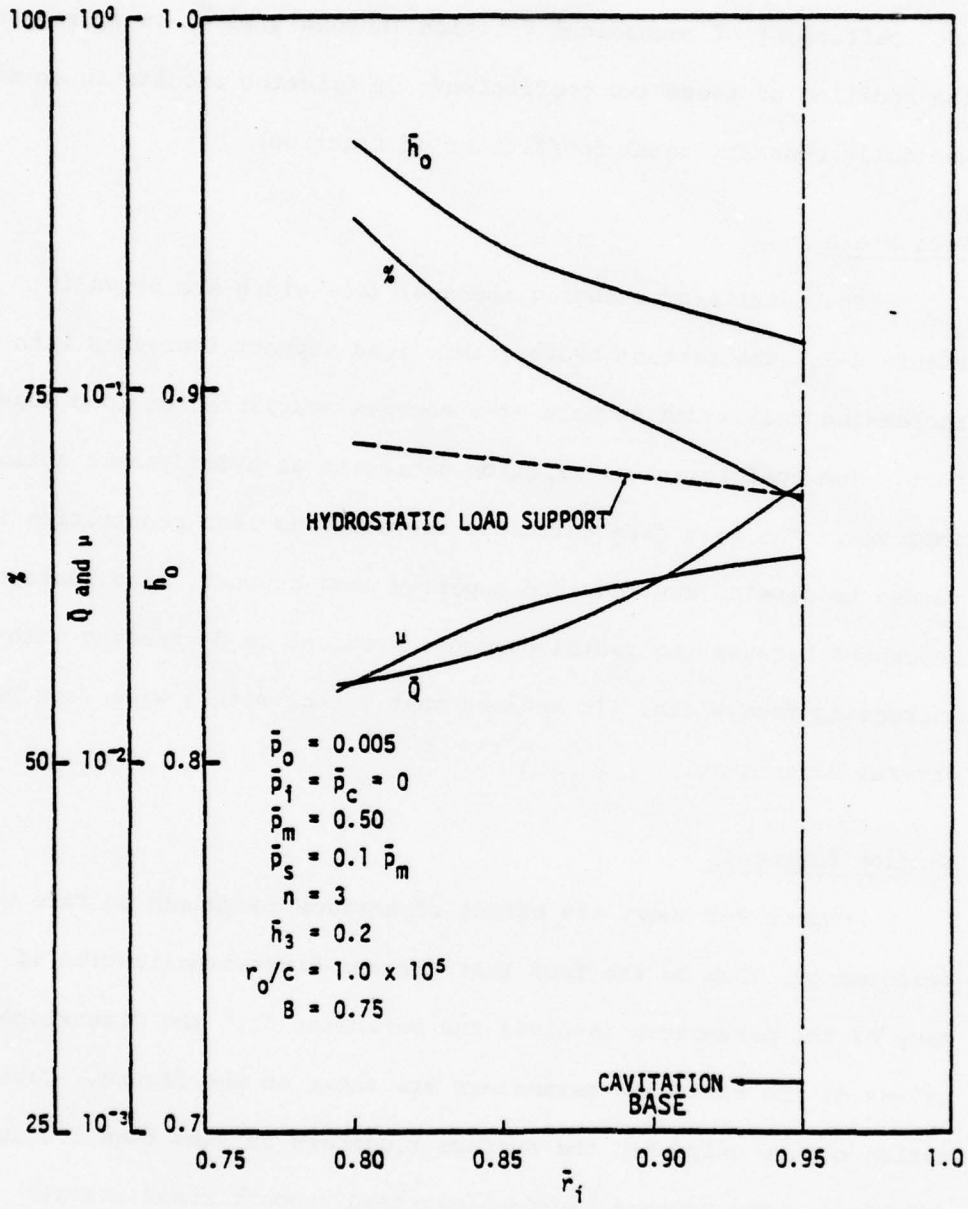

Figure 3-2. Effect of Face Width

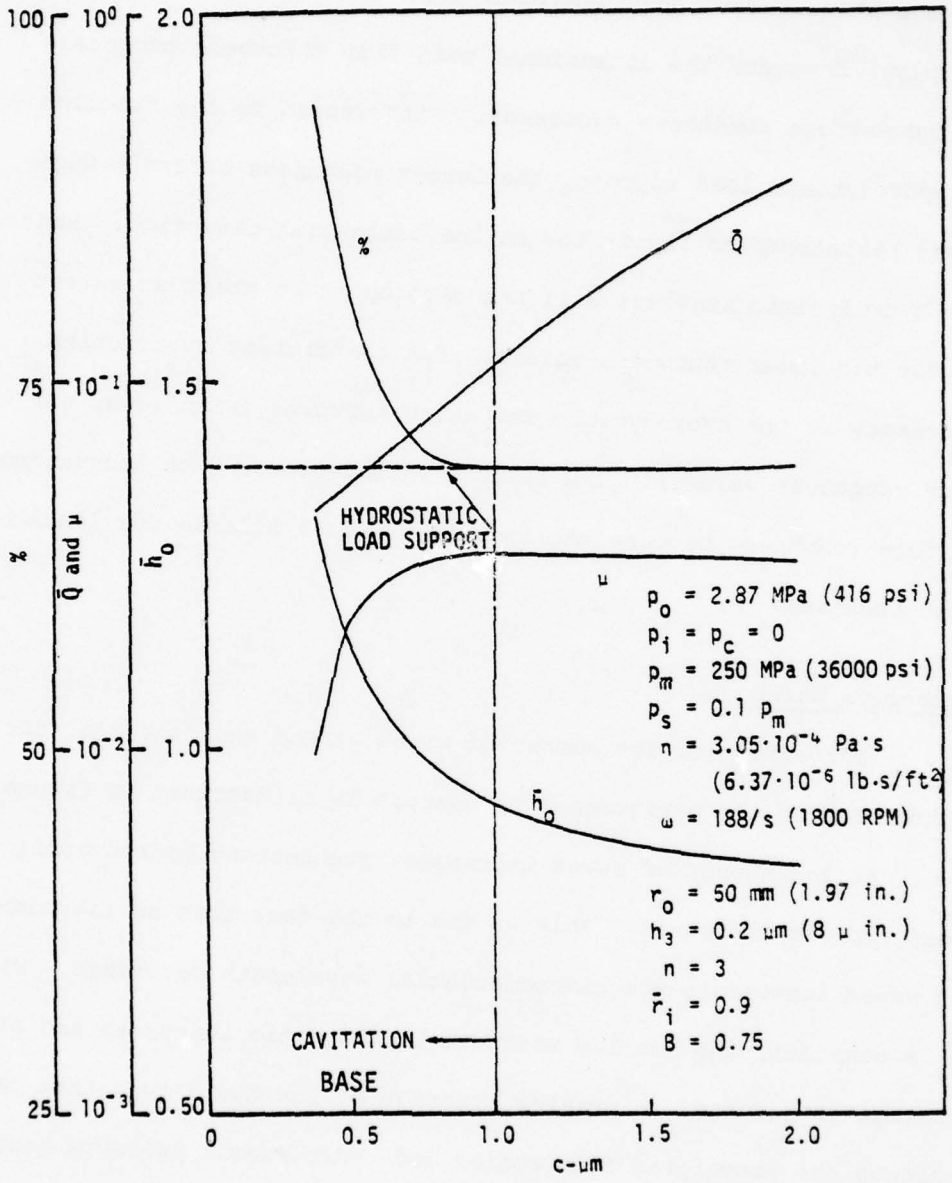

Figure 3-3. Effect of Surface Roughness

actual leakage decreases more than the curve for non-dimensional leakage shows. The non-dimensional mean film thickness increases sharply. However, the dimensional mean film thickness decreases as the surface roughness decreases. With regard to the fraction of hydrodynamic load support, the larger roughness offers a much lower resistance to fluid flow in the tangential direction. Hence, the hydrodynamic pressure will not develop to as great an extent as for the lower roughness values. The coefficient of friction decreases as the hydrodynamic mechanism improves (with lower surface roughness values). The leakage will increase with increasing surface roughness because the amount of area available for leakage also increases.

Number of Waves

The effect of the number of waves around the face seal circumference on the performance parameters is illustrated in Figure 3-4. As the number of waves increases, the percent hydrodynamic load support increases. This is due to the fact that as the number of waves increases, the circumferential wavelength decreases. With $\bar{r}_i$ = constant, the bearing width-to-length ratio increases and side leakage is reduced. A greater fraction of the fluid must then pass through the converging film region and hydrodynamic pressure becomes higher.

As the hydrodynamic forces support more of the load, less asperity contact is needed and $\bar{h}_o$ increases accordingly. The leakage remains essentially constant. There are more regions through

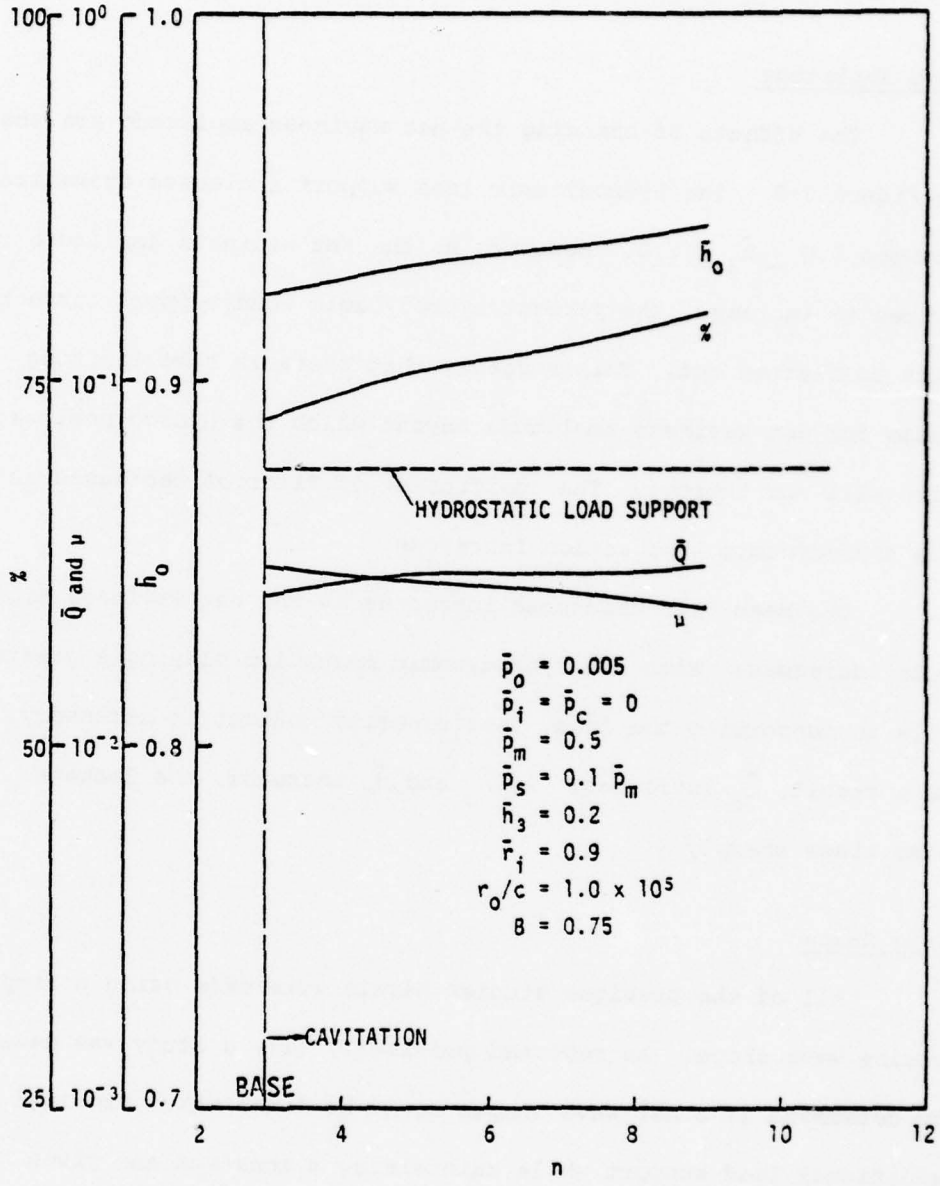

Figure 3-4. Effect of Number of Waves

which leakage can flow (with increasing the number of waves), but each individual region is smaller.

Wave Amplitude

The effects of changing the net waviness amplitude are shown in Figure 3-5. The hydrodynamic load support increases dramatically between $0.0 \leq \bar{h}_3 \leq 2.0$. However, as the net waviness amplitude continues to increase, the percent hydrodynamic load support curve begins to flatten out. This suggests that there is some limiting value for net waviness amplitude beyond which the hydrodynamic action will not improve. The coefficient of friction decreases as the hydrodynamic lubrication increases.

The mean film thickness increases as the net waviness amplitude increases. With the hydrodynamic mechanism playing a greater role in supporting the load, less asperity contact is necessary. As a result, $\bar{h}_o$ increases. As $\bar{h}_o$ and $\bar{h}_3$ increase, the leakage also rises sharply.

Wave Shape

All of the previous studies herein were made using a simple cosine wave shape. As reported previously [1], a study was made to determine if other wave shapes could be found which provided additional load support while maintaining a constant and given leakage. According to the results of the study, the cosine wave shape was found to be the best choice. No other wave shape tried improved the results.

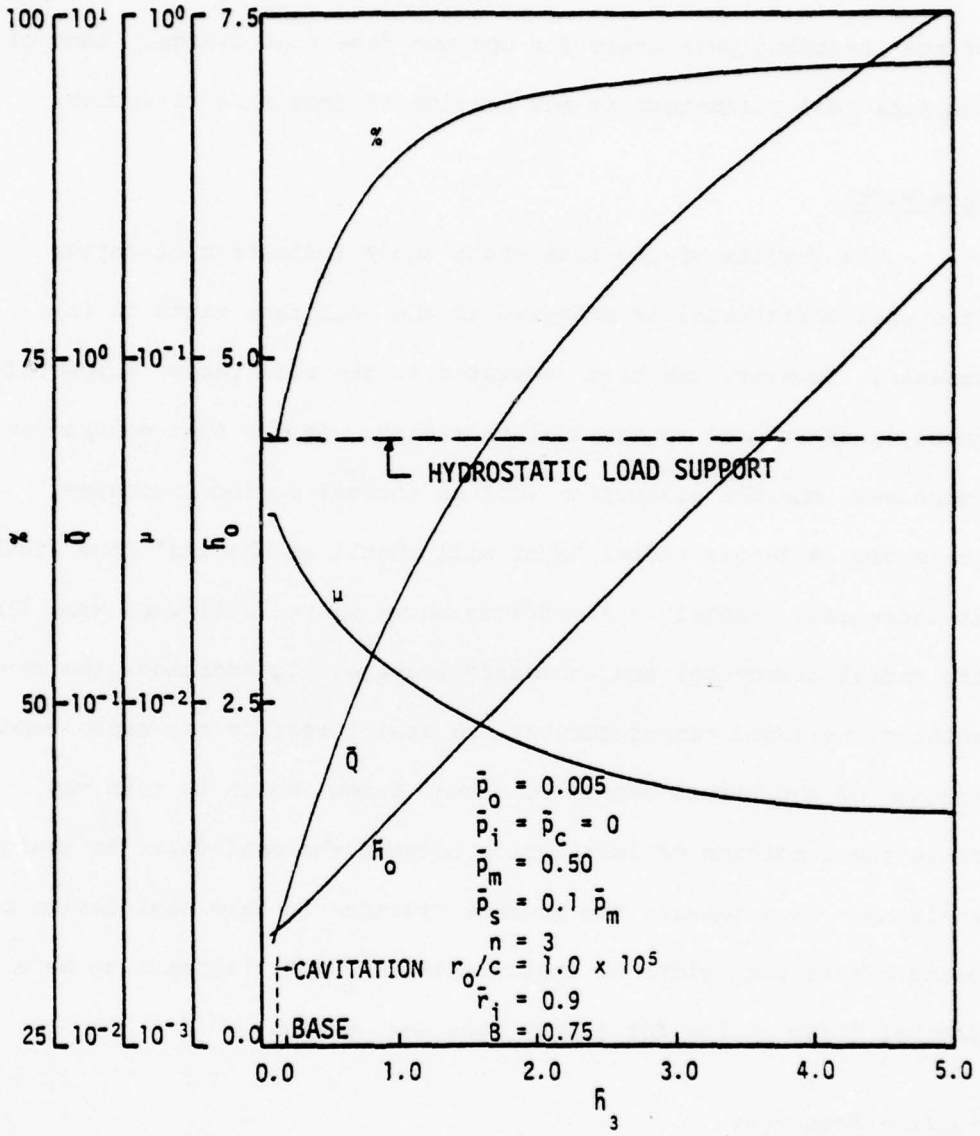

Figure 3-5. Effect of Net Waviness

APPLICATION OF PARAMETER STUDY RESULTS TO FACE SEAL DESIGN

So far, no consideration has been given to practical values of the preceding parameters for optimum face seal design. Each of the face seal parameters is now considered from this viewpoint.

Face Width

The results of the face width study indicate that better face seal performance is achieved as the seal face width is increased. However, the heat generated at the seal faces is approximately proportional to the seal face area. As the heat generation increases, thermal distortion such as thermal coning increases. Therefore, a larger radial taper will result as the seal face width is increased. Radial taper effects cause uneven seal face wear (in the radial direction) and increased leakage. In addition, the resulting increased temperature at the seal interface may cause vaporization of the liquid between the seal faces, which in turn may cause the condition of lubrication between the seal faces to change entirely. As a result, the present practice in face seal design of using a seal face width of approximately $\bar{r}_i \cong 0.9$* appears to be a logical first choice for a wavy face seal design.

Surface Roughness

Figure 3-3 illustrates the importance of surface roughness on the performance of a mechanical face seal. Considerable hydrodynamic lubrication can be achieved if the asperity roughness height is low. For the numerical study, the value of the surface roughness can be lowered in an arbitrary manner. The range of values of surface

*For seals up to a few inches in diameter.

roughness which can be obtained in practice must be determined.

Results presented previously [1] indicate that some face seals presently have surface roughness amplitudes low enough to allow hydrodynamic lubrication. However Figure 3-3 shows that even lower values of roughness amplitude are desirable. Since little research has been conducted on the relationship between material properties and surface roughness, it must be assumed at this point that material pairs can be selected that result in a sufficiently low surface roughness so that a wavy seal design can be made practical. Results from the experiments discussed in Chapter 4 will provide further information on this important subject. For now it is assumed that $c = 20$ μin. is attainable in practice.

Waviness Amplitude

Initial waviness is that amount of waviness that is somehow imposed upon a mechanical face seal ring when it is completely unloaded. When a face seal is placed into operation, the sealed pressure (closing force) flattens the wavy face seal ring against the face seal seat. As a result, the initial waviness is reduced by some amount resulting in a net waviness, which is the parameter used in previous discussions. Net waviness is the important parameter when considering the waviness effects upon hydrodynamic lubrication. The initial waviness is important also because it serves as the source of waviness. The net waviness amplitude is related to the initial waviness amplitude primarily through the stiffness

factor of the face seal ring.

Relationships between initial and net waviness were developed previously [1]. The most important of these relationships are:

$$\bar{h}_{da_1} = \frac{\bar{p}_{a_1}}{\bar{K}} \frac{n^2 + A}{n^6 - 2m^4 + n^2} \tag{3-1}$$

$$\bar{h}_{db_1} = \frac{\bar{p}_{b_1}}{\bar{K}} \frac{n^2 + A}{n^6 - 2m^4 + n^2} \tag{3-2}$$

$\bar{K}$ - stiffness constant for ring $\dfrac{EI_x c^3}{r_c^3 r_o^4 n\omega}$

r_c - radius to seal ring centroid

A - ring constant = $\dfrac{EI_x}{GI_\theta}$

n - number of waves around the seal face

$\bar{h}_{da_1}$, $\bar{h}_{db_1}$ - Fourier coefficients of the deflected waviness

$\bar{p}_{a_1}$, $\bar{p}_{b_1}$ - Fourier coefficient of the pressure

For any particular face seal n, A, and $\bar{K}$ are known constants and $\bar{p}_{a_1}$ and $\bar{p}_{b_1}$ can be determined by use of Equation (2-62) in Reference [1].

The net waviness amplitude, $\bar{h}_n$, is mathematically defined as

$$\bar{h}_{a_1} = \bar{h}_{ia_1} + \bar{h}_{da_1} \tag{3-3}$$

$$\bar{h}_{b_1} = \bar{h}_{ib_1} + \bar{h}_{db_1} \tag{3-4}$$

and

$$\bar{h}_n = \sqrt{\bar{h}_{a_1}^2 + \bar{h}_{b_1}^2} \tag{3-5}$$

where $\bar{h}_{a_1}, \bar{h}_{b_1}$ represent the Fourier coefficients of net waviness amplitude,

$\bar{h}_{ia_1}$ and $\bar{h}_{ib_1}$ are the Fourier coefficients of the initial waviness amplitude, and

$\bar{h}_{da_1}, \bar{h}_{db_1}$ are the deflected waviness amplitude Fourier coefficients

and where $\bar{h}_{b_1}$ can be set to zero since this term merely positions the wave.

Using the above relationships, the results in Figure 3-6 were obtained. Using Figure 3-6 in conjunction with Figure 3-5 gives the initial waviness amplitude required for a desired net waviness amplitude. The larger the value of ring stiffness $\bar{K}$, the less initial waviness amplitude is required to achieve a particular net waviness, as would be expected. It is also apparent that for a given initial waviness, there may be as many as three different operating conditions (net waviness values). (See points A, B, and C for $\bar{K} = 5.0 \times 10^{-7}$ on Figure 3-6). The determining factor as to whether there are three possible operating conditions or only one is the stiffness of the ring. The less stiff rings have three possible operating conditions, though only two may be shown in Figure 3-6. Actually, for the lower values of $\bar{K}$ the curves will continue to rise when $\bar{h}_3 > 5.0$. Therefore, there will be three

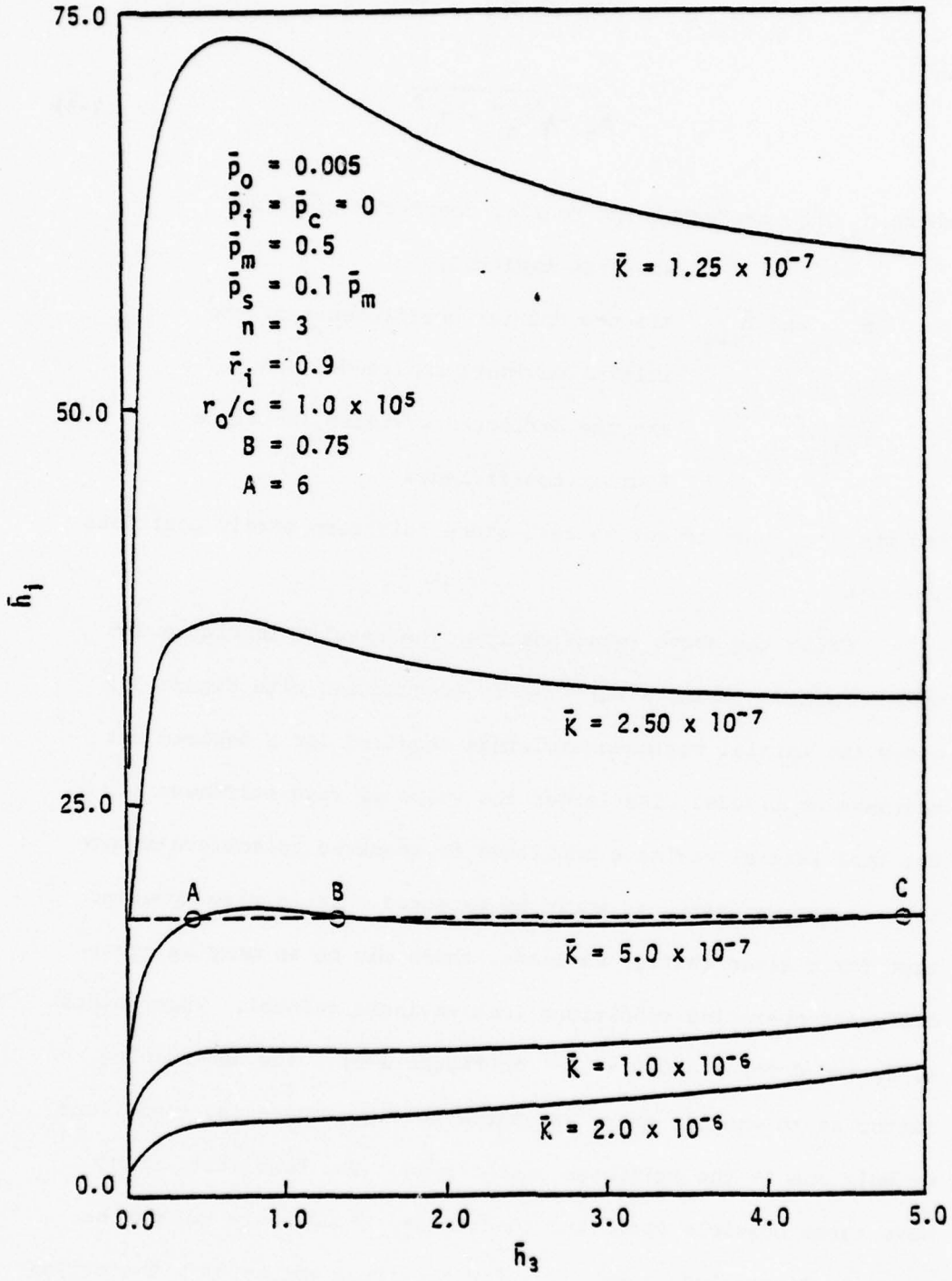

Figure 3-6. Required Initial Waviness

points of intersection. The stiffer rings of Figure 3-6 have only one operating condition for a particular initial waviness as shown.

Using methods developed and presented in the previous annual report [1], it was determined that operating points in Figure 3-6 for which the $\bar{h}_i$ versus $\bar{h}_3$ curve has a positive slope are stable. Where the slope is negative, operation is unstable. Thus operation can occur at points A and C, but not at point B in Figure 3-6. Figure 3-6 also shows that the amount of initial waviness must be carefully controlled in some cases. For example, if operation is occurring at point A and a small increase in initial waviness occurs, the stable operation point will move beyond point C and high leakage will result.

To provide additional design information on the effect of initial waviness, additional studies were made for larger numbers of waves. All parameters were held at the base case values except the number of waves was changed from three to six and to nine. The performance curves and the required initial waviness curves for n = 3 are illustrated in Figures 3-5 and 3-6, respectively. These are to be compared to Figures 3-7 and 3-8 for n = 6, and Figures 3-9 and 3-10 for n = 9. Comparing the three sets of curves, a few generalizations can be made. The performance curves of Figures 3-5, 3-7, and 3-9 indicate that the percent hydrodynamic load support and face seal leakage increase to a higher level at a faster rate with increasing net waviness amplitude for the higher values of n. Correspondingly, the coefficient of friction decreases, for a particular net waviness, as n increases.

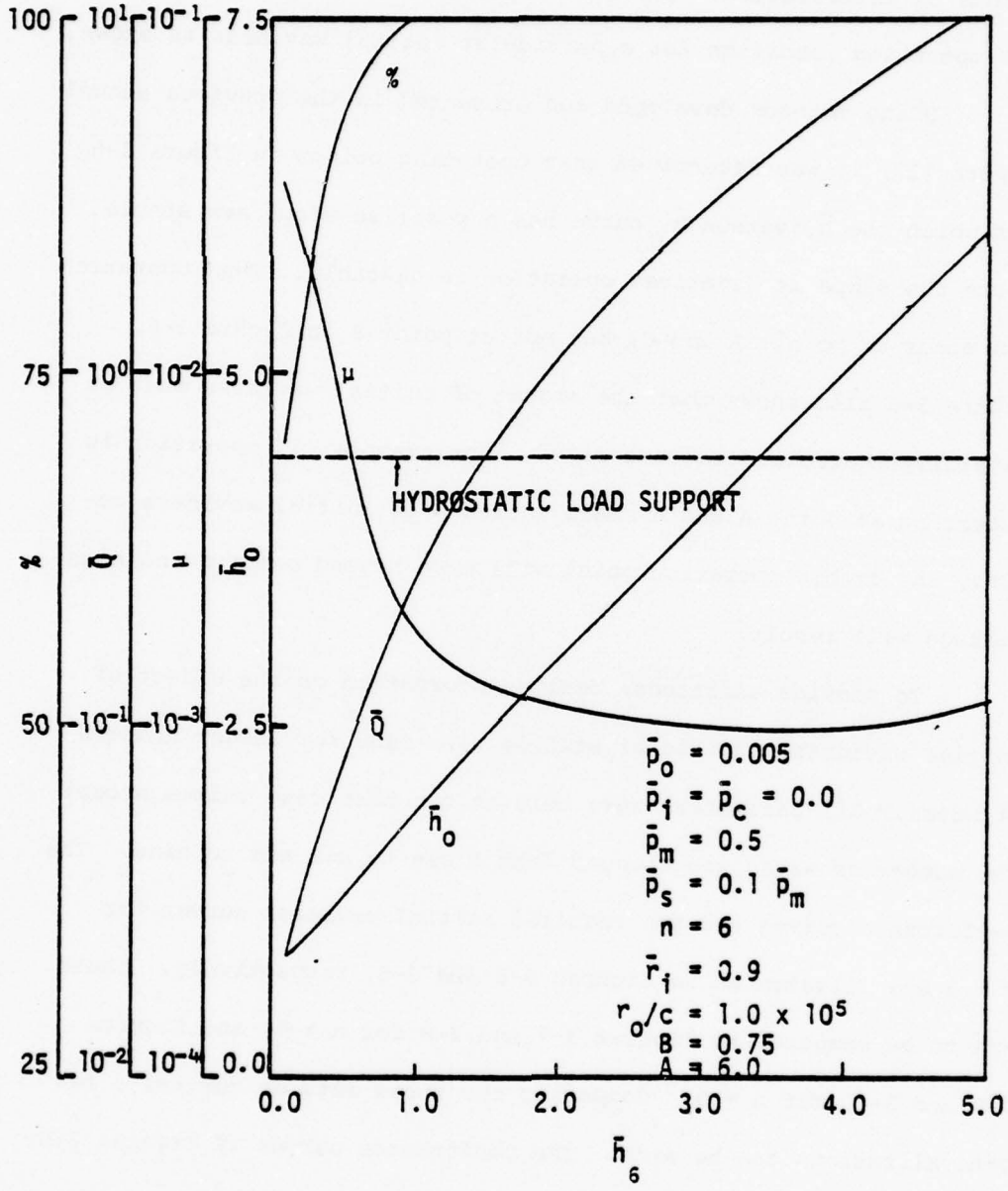

Figure 3-7. Effect of Net Waviness (n = 6)

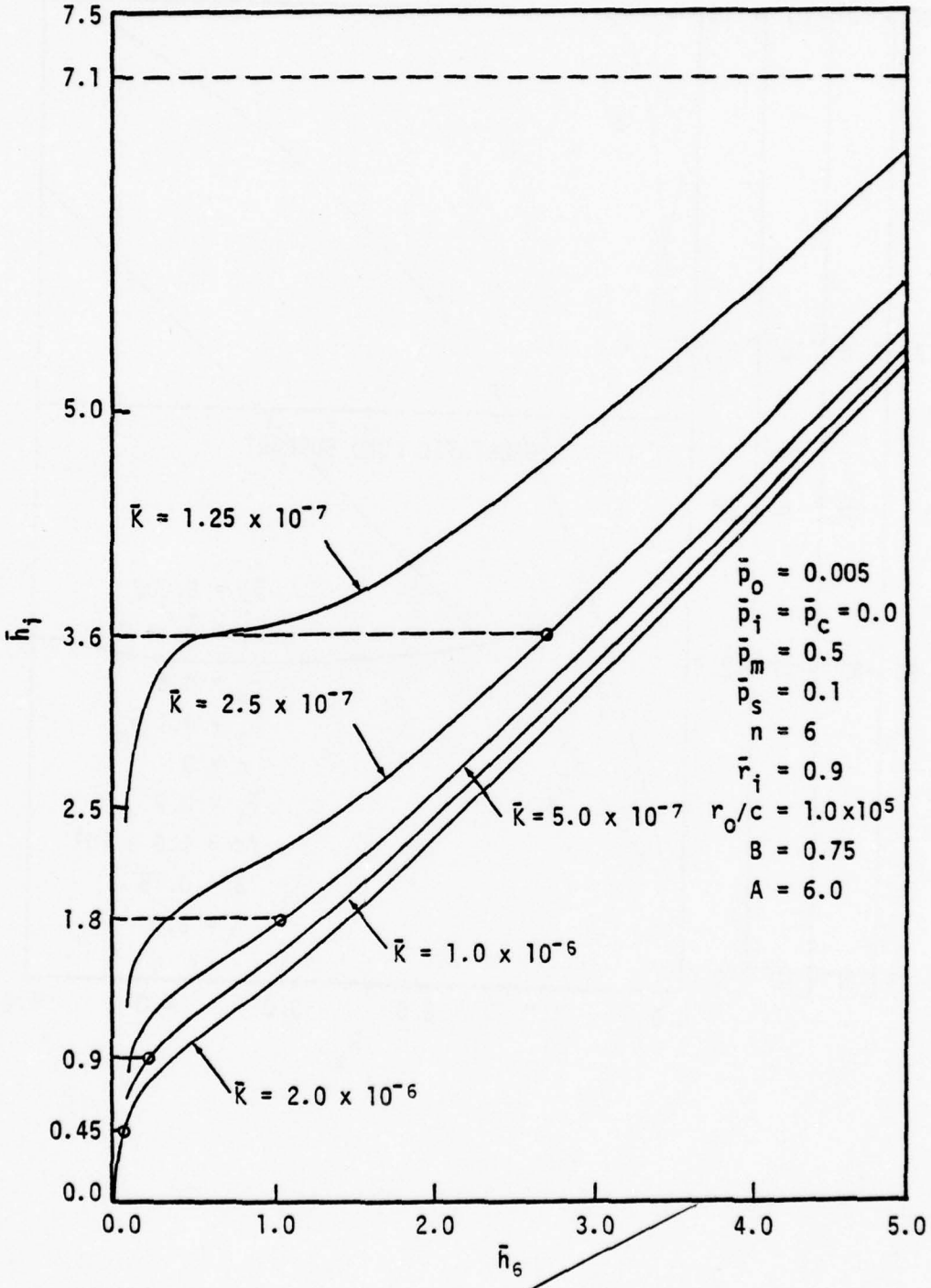

Figure 3-8. Required Initial Waviness (n = 6)

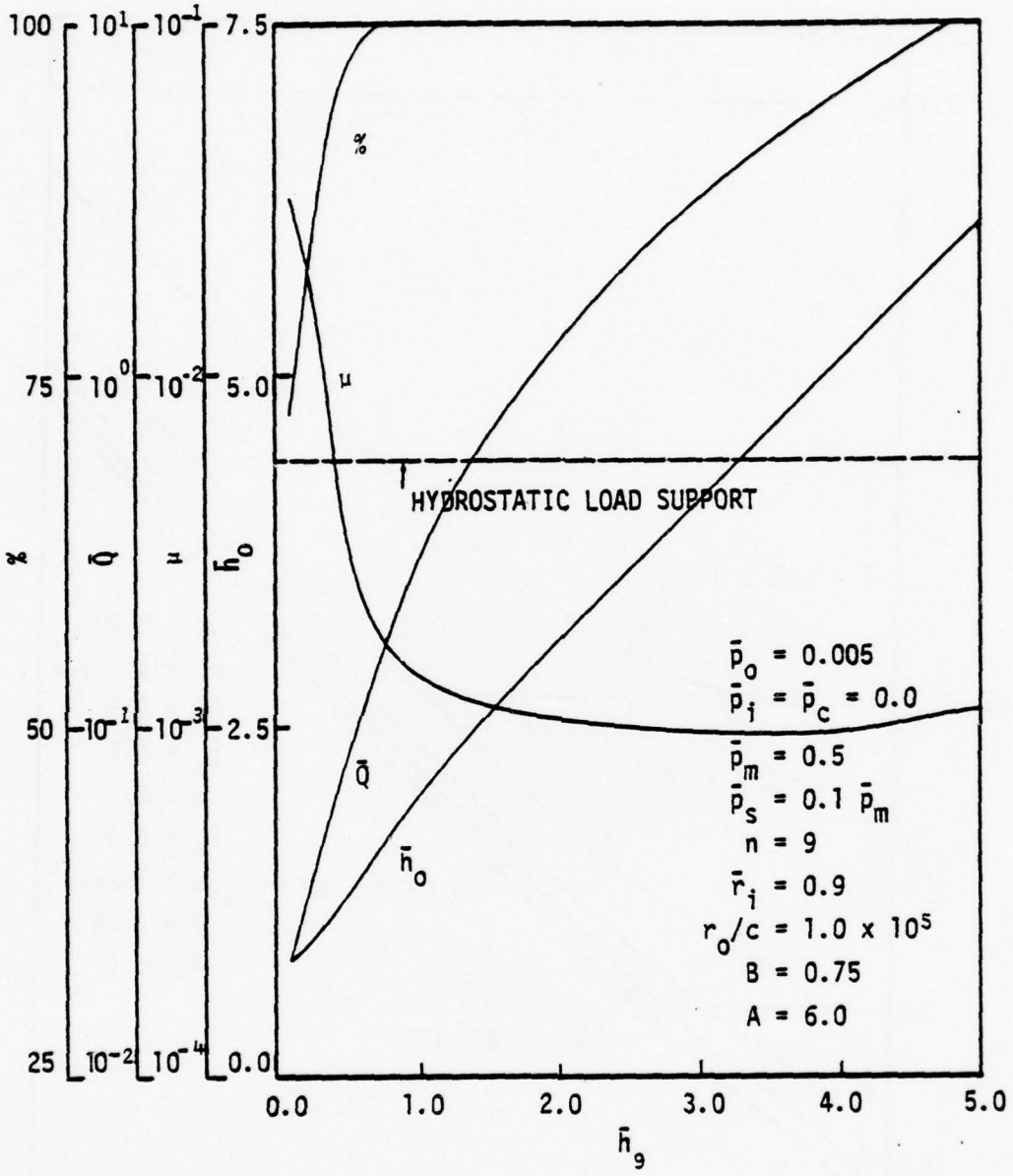

Figure 3-9. Effect of Net Waviness (n = 9)

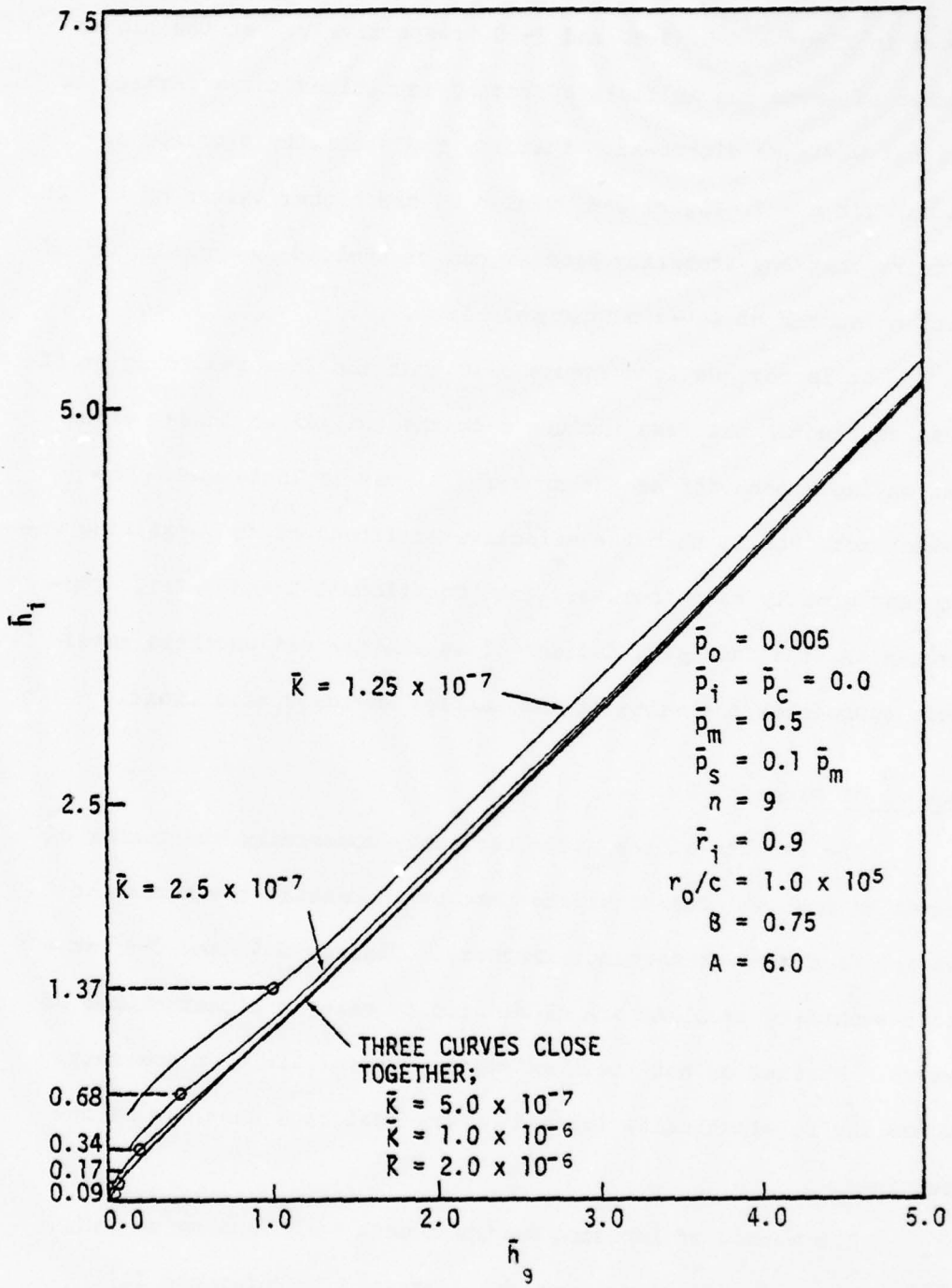

Figure 3-10. Required Initial Waviness (n = 9)

The required initial waviness curves for n = 3, 6, and 9 are shown in Figures 3-6, 3-8, and 3-10, respectively. At the higher number of waves the multiple operating conditions for a particular initial waviness disappear. That is, the stability problems apparent for n = 3, Figure 3-6, vanish at the higher values of n. It appears that any stability problem can be avoided by imposing a sufficient number of waves on the seal face.

It is obvious from Figure 3-10 that the face seal ring stiffness constant $\bar{K}$ has less influence on the initial waviness versus net waviness behavior as the number of waves is increased. The reason for this is that the effective stiffness of the seal ring increases greatly as n increases (see Equations 3-1 and 3-2)). Consequently, the face seal deflects less and the net waviness amplitude approaches the value of the initial waviness as a limit.

Number of Waves

The results of the parameter study concerning the number of waves on the seal face indicate that by increasing the number of waves, face seal performance improves. Figures 3-7 and 3-9 show that stability problems are eliminated by using a higher number of waves. Whether or not there exists a physical limit on how many waves can be elastically imposed on the seal face must now be determined.

The method of imposing waviness on a seal face to be considered here is the elastic method discussed in Reference [1], where two O-rings provide a bending moment when pressure is applied.

The reason for considering an elastic method, as opposed to lapping the waviness into the face, is that with such a method the waviness can be moved around the seal ring, thereby evenly distributing the wear on the seal face and preserving the waviness (see Reference [1]).

Figure 3-11 shows the face seal ring cross-section and the waviness cylinder (with only one wave shown). The wavy lines in Figure 3-11 are the outside edges of the O-ring grooves. The area between the wavy lines is to be pressurized to cause an angularly varying bending moment about the seal ring centroid, thereby deforming the seal ring into the desired waviness.

The amplitude of the resulting waviness is a function of many parameters including the pressure used between the O-rings and the number of waves around the face seal. Assuming that the O-ring grooves are in the shape of a sine function, the desired wave shape, the moment that results when the area between the O-rings is pressurized takes the form

$$M = M_o \sin n\theta \tag{3-6}$$

The maximum moment that can be achieved for a given pressure is of interest since any lesser moment will also be possible. That is, let $\sin n\theta = 1.0$. From Figure 3-11, the maximum bending moment is

$$M_o = (2a)\left(\frac{\ell}{2} - a\right)p_b \tag{3-7}$$

where a - amplitude of waviness of the O-ring,

ℓ - seal ring length,

p_b - pressure used to cause bending,

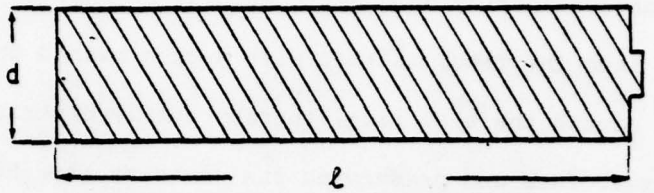

(a) Seal Ring Cross-Section

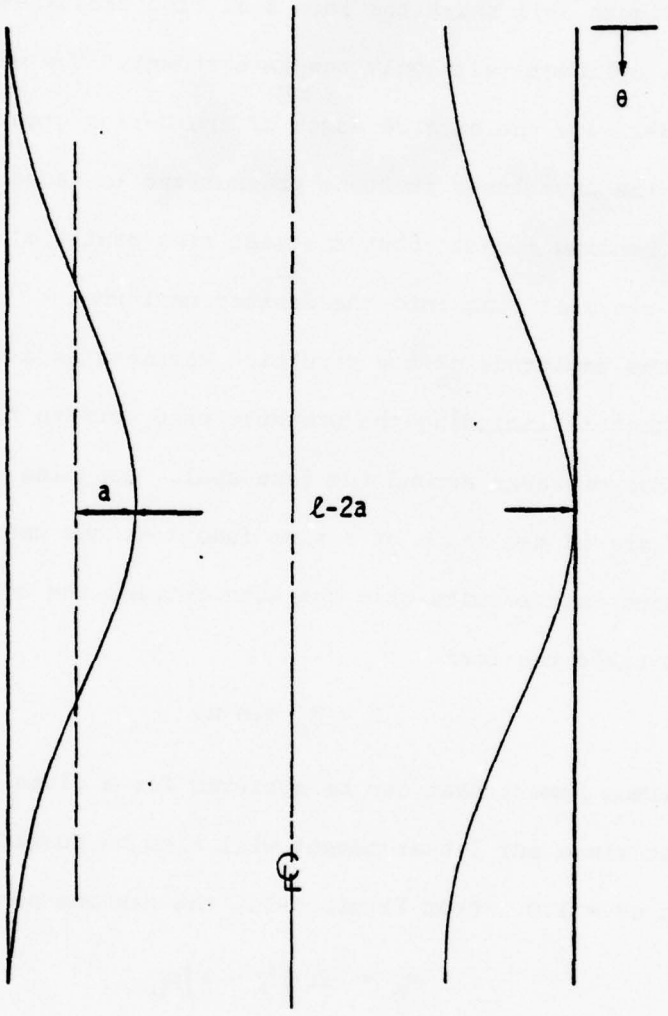

(b) Waviness Cylinder

Figure 3-11. Waviness Generating Mechanism

M_o - maximum distributed bending moment (in lb. per in. of circumference).

It would appear from Equation (3-7) that an optimum value of "a" exists to maximize M_o. Since ℓ and p_b are constants, the optimum value of "a" is arrived at

$$\frac{dM_o}{da} = p_b (\ell - 4a) = 0 \tag{3-8}$$

Therefore, $a = \ell/4$ is the optimum value of "a." Substituting this value for "a" back into Equation (3-7)

$$M_{o_{max}} = \frac{1}{8} \ell^2 p_b \tag{3-9}$$

Lebeck [22] has derived an expression that relates the initial waviness amplitude h_i to the bending moment M_o.

$$M_o = \frac{h_i EI_x (n^2 - 1)^2}{r_c^3 (1 + A)} \tag{3-10}$$

By equating the two expressions for M_o (Equations 3-9) and (3-10)), the desired relationship among h_i, p_b, and n is obtained.

$$h_i = \frac{\ell^2 r_c^3 (1 + A)}{8EI_x (n^2 - 1)^2} p_b \tag{3-11}$$

Non-dimensionalizing Equation (3-11), the following expression is obtained:

$$\bar{h}_i = \left(\frac{1}{8}\right)\left(\frac{1}{\bar{K}}\right)\left(\frac{\ell^2}{r_o^2}\right)\left[\frac{1 + A}{(n^2 - 1)^2}\right]\bar{p}_b \tag{3-12}$$

For a mechanical face seal to operate in a particular, desired manner (region), there exists a value of $\bar{h}_n$, net waviness,

that must be present. To obtain this $\bar{h}_n$, an initial waviness $\bar{h}_i$ must be imposed on the seal face, defined by Equation (3-12). If the waviness pressure $\bar{p}_b$ is held constant, then for any specific value of n (all other parameters held constant) there is a maximum $\bar{h}_i$ that can be imposed. Any lesser value of $\bar{h}_i$ can be achieved. That is, there exists a range of $\bar{h}_i$, and thus $\bar{h}_n$, that is possible, given $\bar{p}_b$, $\bar{K}$, n, and the other face seal parameters in expression (3-12). For example, for

$$\frac{\ell}{r_o} = 0.5$$

$$A = 6.0$$

$$\bar{p}_b = \bar{p}_o = 0.005 \qquad (3\text{-}13)$$

$$n = 3, 6, 9$$

$$\bar{K} = \text{variable}$$

the following $\bar{h}_i$ shown in Table 3-2 are possible.

A comparison is made between the maximum $\bar{h}_i$ possible for a specific case and the $\bar{h}_i$ required to result in a particular, desired $\bar{h}_n$. Referring to Figure 3-6 , all stable values of $\bar{h}_3$, within the range of the figure, are possible for each value of $\bar{K}$.

However, a comparison between the values in Table 3-2 for n = 6 and n = 9 and Figures 3-8 and 3-10 shows that not all operating conditions are possible (for the example face seal). For n = 6 and $\bar{K} = 1.25 \times 10^{-7}$, all desired $\bar{h}_6$ shown in Figure 3-8 can be achieved. However, for all other $\bar{K}$ curves of n = 6, and for all $\bar{K}$ curves for n = 9, there are intersections of the $\bar{h}_{i_{max}}$ line

Table 3-2. Initial Waviness Amplitudes for n = 3, 6, 9

Ring Stiffness ($\bar{K}$)	$\bar{h}_{i_{max}}$ (n=3)	$\bar{h}_{i_{max}}$ (n=6)	$\bar{h}_{i_{max}}$ (n=9)
1.25×10^{-7}	136.7	7.1	1.37
2.50×10^{-7}	68.4	3.6	0.68
5.00×10^{-7}	34.2	1.8	0.34
1.00×10^{-6}	17.1	0.9	0.17
2.00×10^{-6}	8.5	0.45	0.09

and the h_i versus $\bar{h}_n$ curves. The physically possible operating conditions are those to the left of the point of intersection for each curve. For example, with n = 6 and $\bar{K} = 2.5 \times 10^{-7}$ there is a maximum possible initial waviness that can be achieved of 3.6 non-dimensional units. Correspondingly, referring to Figure 3-8, the maximum $\bar{h}_6$ that can result is $\bar{h}_6 = 2.7$ units. Therefore, $0 \leq \bar{h}_6 \leq 2.7$ is the range of possible operating conditions for this particular case. Again referring to Figure 3-8, as the seal ring stiffness increases, the amount of initial waviness that can be imposed elastically decreases, as does the resulting $\bar{h}_6$ that can be achieved. In fact, $\bar{h}_6$ reaches such a low value that it is doubtful that any appreciable hydrodynamic action will occur.

The same behavior exists for n = 9 (Figure 3-10). The ranges of possible operating conditions are to the left of the points of intersection. Again, the range of possible $\bar{h}_9$ decreases rapidly with increasing $\bar{K}$, to such a point that hydrodynamic action becomes very small.

Table 3-3 summarizes the maximum net waviness amplitudes that result when the maximum initial waviness amplitudes for stable operating conditions are imposed. This information is obtained from Figures 3-6, 3-8, and 3-10.

Table 3-3. Maximum Net Waviness Amplitudes for n = 3, 6, 9 (for stable operation)

Ring Stiffness ($\bar{K}$)	$\bar{h}_{3_{max}}$	$\bar{h}_{6_{max}}$	$\bar{h}_{9_{max}}$
1.25×10^{-7}	0.75	>5.00	1.00
2.50×10^{-7}	0.75	2.70	0.42
5.00×10^{-7}	0.75	1.08	0.18
1.00×10^{-6}	> 5.00	0.22	0.08
2.00×10^{-6}	> 5.00	0.10	0.05

It is important to note that the behavior of $\bar{h}_{3_{max}}$ (shown in Table 3-3) results from the instability problems associated with the n = 3 case, displayed graphically in Figure 3-6, and discussed in detail previously.

It can be seen from the performance curves (Figures 3-5, 3-7, and 3-9) that as the net waviness amplitude increases, the face seal leakage and hydrodynamic load support also increase. Therefore, since the $\bar{h}_n$ maximum is known for each value of $\bar{K}$ and n studied (see Table 3-3), the maximum face seal leakage and maximum hydrodynamic load support are also known. This information is displayed graphically in Figures 3-12 and 3-13. The curves of Figure 3-12 connect points of maximum percent hydrodynamic load

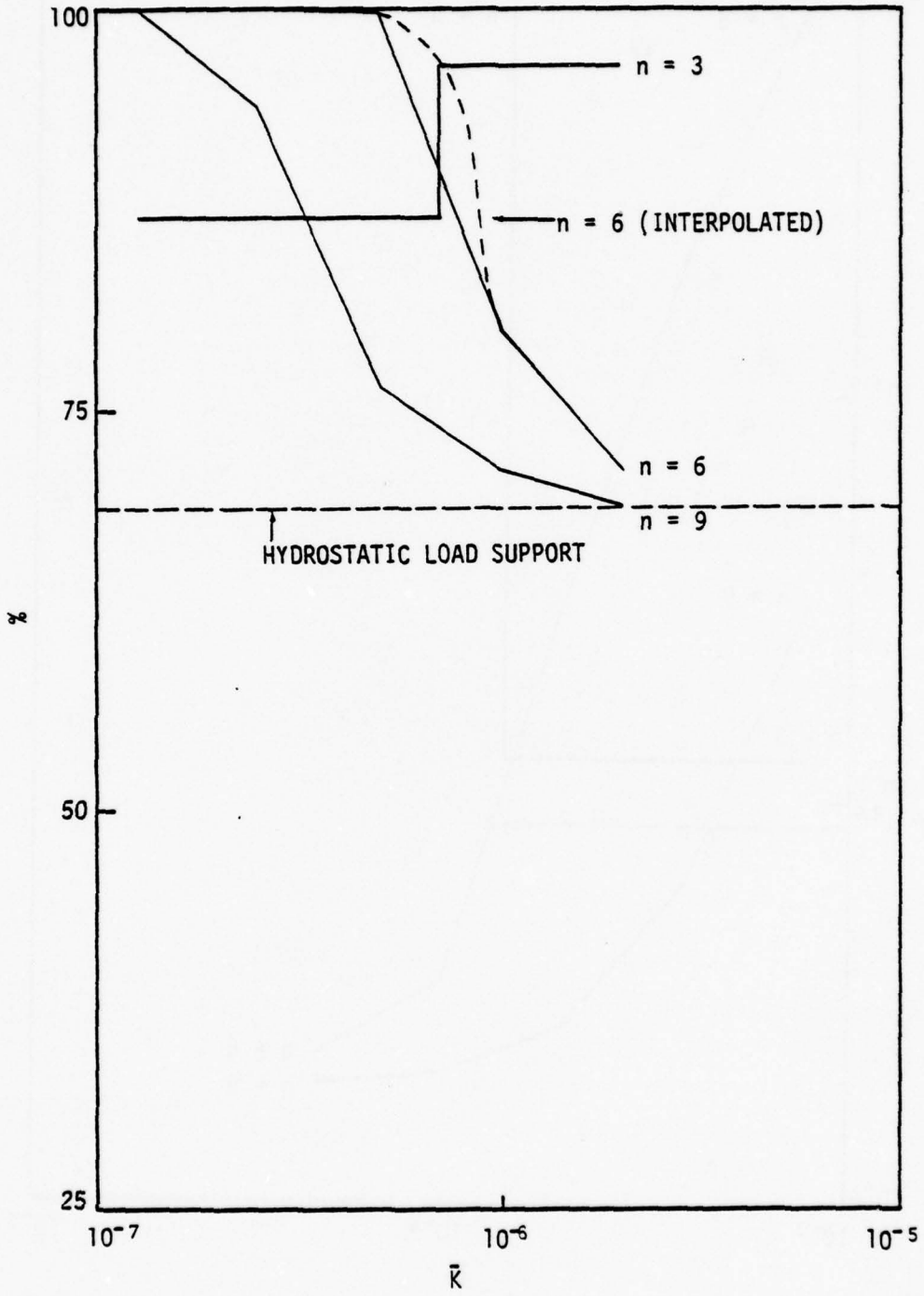

Figure 3-12. Hydrodynamic Load Support for Maximum $\bar{h}_n$ (Base Case)

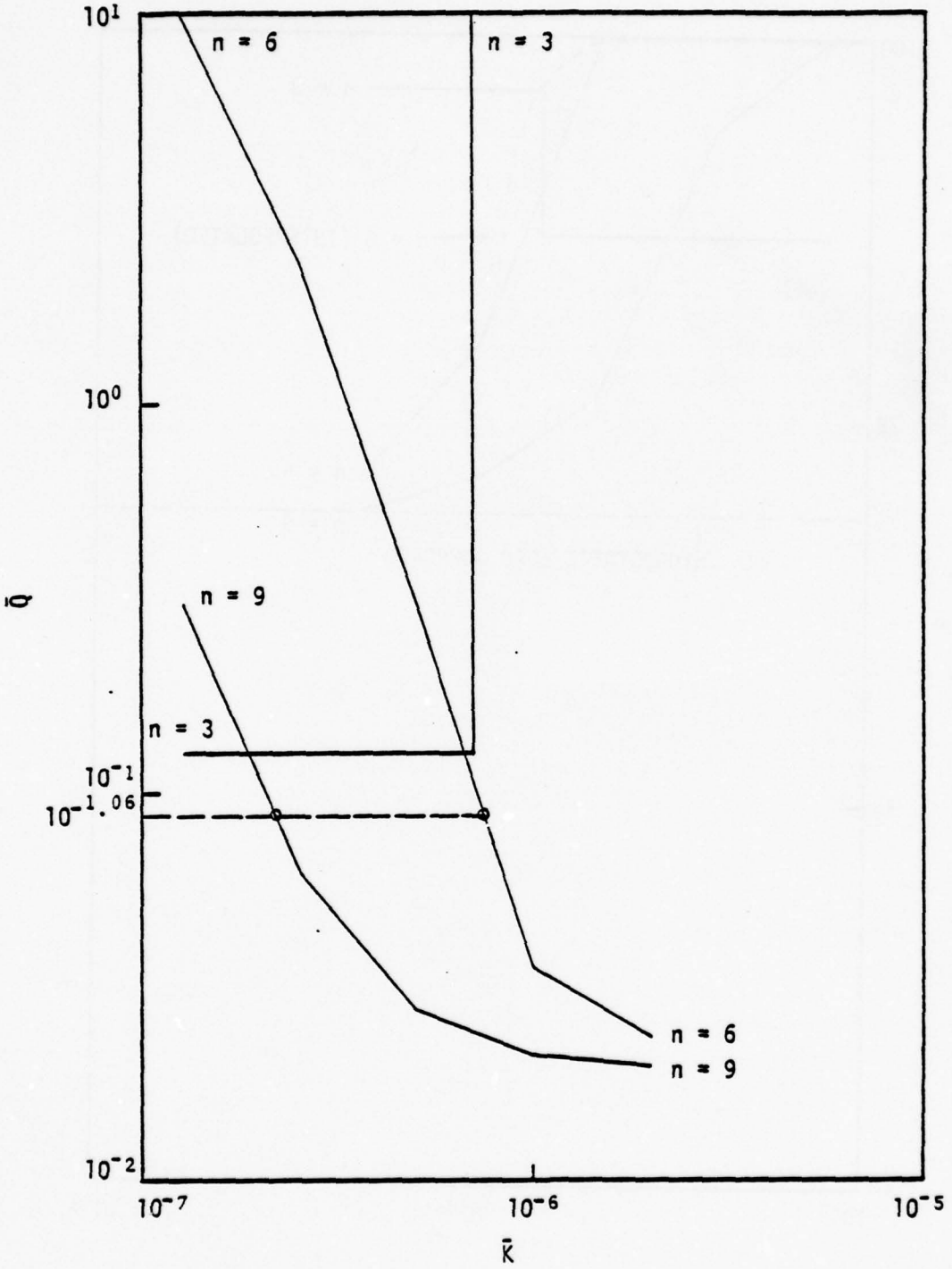

Figure 3-13. Leakage for Maximum $\bar{h}_n$ (Base Case)

support for n = 3, 6, and 9, and $1.25 \times 10^{-7} \leq \bar{K} \leq 2.0 \times 10^{-6}$. Figure 3-13 is the same type of graph as Figure 3-12 only for maximum face seal leakage. The possible operating ranges are to the left of the n = 6 and n = 9 curves and below the n = 3 curves.

The step-like behavior of the n = 3 curves graphically portrays the instability problems associated with this case (see Table 3-3). In addition, Figures 3-12 and 3-13 emphasize the fact that as n is increased, the range of possible operating conditions is reduced. With these figures one can tell at a glance the physically possible hydrodynamic load support and leakage ranges as a function of $\bar{K}$ and n.

EXAMPLE

In order to illustrate how the previous information can be used in the design of a wavy mechanical face seal, an example is presented. Two design procedures are used for comparison and illustration purposes.

The application that is considered for this example is that of the "base case" (see Table 3-1). The maximum allowable leakage for this example is taken as 2 cc/min. This value for leakage is chosen because it offers the greatest number of possible design complications including stability considerations, and because this value represents an acceptable leakage for many applications. Nondimensional leakage, $\bar{Q}$, is 0.0878.

Assumptions

There are a few assumptions that must be made concerning the mechanical face seal application, materials, and face seal geometry.

1) The seal face width is $\bar{r}_i = 0.9$.

2) The surface roughness of $c = 0.5$ μm (20 μin.) is attainable.

3) The traveling wave concept is to be used in order that the waviness will not wear away.

Three of the five design parameters studied in this investigation have been fixed at certain values for this example. The reasons for this were discussed previously. The two design parameters that are still to be examined are the number of waves around the seal face, and the amplitude of the net waviness. The objective is to attain the maximum amount of hydrodynamic load support while maintaining the leakage at or below the maximum allowable leakage.

Procedure 1

The most useful figures are 3-5 through 3-10. These figures relate the two remaining design parameters. From Figure 3-5 for $n = 3$, the $\bar{h}_3$ that gives $\bar{Q} \leq 0.0878$ is $\bar{h}_3 \leq 0.60$.[1] From Figure 3-6 for $\bar{h}_3 = 0.60$ and $\bar{K} = 2.5 \times 10^{-7}$ (the base case value of $\bar{K}$), the stable $\bar{h}_i$ required is $\bar{h}_i = 36.8$ units. For $n = 3$ all values of initial waviness for Figure 3-6 are possible. Although an

[1] The figures actually require $\log \bar{Q}$. Therefore, $\log \bar{Q}_{max} = -1.075$. Figures 3-5, 3-7, and 3-9 indicate that the largest h_n that still limits $\bar{Q}_{max} \leq 0.0878$ and provides the highest percent hydrodynamic load support is best, so the inequality will no longer be considered.

$\bar{h}_i$ = 36.8 units is physically possible to achieve, this particular value of $\bar{h}_i$ is very close to the peak of the $\bar{h}_3$ versus $\bar{h}_i$ curve for $\bar{K} = 2.5 \times 10^{-7}$ (see Figure 3-6). Consequently, if $\bar{h}_i$ cannot be imposed precisely enough, stability problems are likely to occur. This would not be a recommended operating condition. However, for the purpose of illustration, it is assumed that $\bar{h}_i$ can be made 36.8 units. Therefore, a design solution for this example is n = 3, $\bar{h}_3$ = 0.60 and $\bar{h}_i$ = 36.8, with all other design parameters as previously specified. Referring to Figure 3-5, the percent hydrodynamic load support that is expected for this design is 84.5 percent, a significant gain over the lower limiting value of 69 percent. The coefficient of friction is 0.0178. This result is summarized in Table 3-4.

Table 3-4. Example Face Seal Design Results (Procedure 1) ($\bar{Q}_{max}$ = 0.0878)

	n = 3	n = 6	n = 9	n = 9 (modified)
$\bar{h}_i$	36.8	1.98	0.68	0.775
$\bar{h}_n$	0.60	0.55	0.42	0.525
%	84.5	95.3	94.50	98.20
μ	0.0178	0.0065	0.0066	0.0036

The same procedure used for n = 3 is used for n = 6. The results are shown in Table 3-4. The $\bar{h}_i$ required is physically possible. There is a significant increase in percent hydrodynamic load support and a corresponding decrease in the coefficient of friction. There is no stability problem for this design.

Finally, the design procedure is used for n = 9. This case is different from the n = 3 and n = 6 cases and is explained in detail. From Figure 3-9 for log $\bar{Q}_{max}$ = -1.057, the $\bar{h}_9$ required is $\bar{h}_9$ = 0.525. Referring to Figure 3-10 for $\bar{h}_9$ = 0.525, the $\bar{h}_i$ required is $\bar{h}_i$ = 0.75. However, this value is larger than the maximum $\bar{h}_i$ that can be achieved (see Table 3-2). Consequently, the highest $\bar{h}_i$ that can be attained (for this example) is $\bar{h}_i$ = 0.68. The $\bar{h}_9$ that corresponds to $\bar{h}_i$ = 0.68 is $\bar{h}_9$ = 0.42. Referring to Figure 3-9 for $\bar{h}_9$ = 0.42, the percent hydrodynamic load support is % = 94.50 percent, while the coefficient of friction is μ = 0.0066. Table 3-4 summarizes the results of this example face seal design.

So far in this example $\bar{K}$ has been restricted to the base case value. In reality n and $\bar{K}$ would be allowed to vary through a wider, more precise range. If for n = 9, $\bar{K}$ were allowed to assume any value and in particular $\bar{K} = 2.33 \times 10^{-7}$, the results obtained make the n = 9 design more desirable. (See Table 3-4 for n = 9 (modified)).

Procedure 2

Another, more simplified design procedure can also be used for this face seal example design. Figures 3-12 and 3-13 contain all of the most important information on Figures 3-5 through 3-10 in a very concise form. In addition, $\bar{K}$ can assume any value in the range of $\bar{K}$ that has been examined.

Referring to Figure 3-13, the points of intersection of the

leakage curves for n = 3, 6, and 9, and log $\bar{Q}_{max}$ = -1.057 are determined. (For n = 3, since there is no point of intersection, an approximation will have to be made throughout the design procedure.) These points of intersection define the optimum $\bar{K}$ for each value of n. Knowing the optimum values of $\bar{K}$, Figure 3-12 is used to determine the maximum percent hydrodynamic load support that can be obtained for each value of n. The results are shown in Table 3-5.

Table 3-5. Example Face Seal Design Results (Procedure 2) ($\bar{Q}_{max}$ = 0.0878).

	n = 3	n = 6	n = 9
$\bar{K}$ (optimum)	Determined by Stability	7.55×10^{-7}	2.19×10^{-7}
%	$\leq$87.2	86.7	95.0

The results shown in Table 3-5 differ from those in Table 3-4 for the following reasons. Error has been introduced in the graphical method used in producing the figures, particularly Figures 3-12 and 3-13. If all of the curves shown in all of the figures were continuous, the results in Table 3-4 and 3-5 would be identical. However, the data points are quite widely spread and are linearly interpolated causing considerable error.

The major advantage of Procedure 2 over Procedure 1 is its speed and simplicity. However, an important disadvantage of Procedure 2 is demonstrated with the n = 3 case. For face seals that

have a stability problem (no point of intersection for the Q_{max} = constant curve and the leakage curve), there is not enough information contained in Figures 3-12 and 3-13 to determine the practical operating conditions. In such cases, the designer must use the curves of Procedure 1. In addition, although Procedure 2 indicates the possible operating conditions for a face seal design, $\bar{h}_i$ must still be determined from the figures used in Procedure 1.

In summary, the wavy face seal design results in a considerable improvement in hydrodynamic load support for a given leakage over a non-wavy face seal. Theoretically, the wear rate is reduced by a factor of 17:1 for the n=9 case where % = 98.20 when compared to a flat face seal.

CHAPTER 4

SEAL TEST APPARATUS

To date, only very limited studies have been made of wavy seals operating in water. To provide additional experimental verification of the model described herein and to provide facilities for further studies related to other seal problems, the design and construction of a mechanical seal test apparatus has been completed as a part of this project.

BASIC REQUIREMENTS

A test apparatus designed for research must meet more requirements than test machines used for study of commercial seals. First it is necessary that a wide range of speed and sealed pressure be available in order to verify modeled behavior over a wide range of conditions. Certain otherwise uncontrolled variables such as shaft runout, seal waviness, and seal radial taper must be very carefully controlled. For testing the lubrication model of interest, it is necessary that a controllable waviness be applied to the seal faces, and in order to reduce the effects of wear this waviness must be moved circumferentially with respect to the primary ring. Leakage from the seal must be measured. Torque must be measured in a manner such that the seal torque is measured independently of bearing torque or torque arising from a second seal used in a tandem arrangement. Many of the distortions commonly found in commercial seals must be minimized.

To meet all of these requirements, the design of such a test apparatus must depart somewhat from that found in commercial practice. On the other hand, it is important that the apparatus be capable of simulating commonly found seal installations. In fact, it is useful to be able to install a commercially available standard seal in the test rig.

SPECIFICATIONS

The test apparatus specifications which satisfy the above basic requirement are set forth below.

Configuration:	Horizontal shaft, single seal with torque measured on the seal housing. Rotating secondary ring.
Size:	Accepts up to 3-5/8 inch nominal shaft size seal. 4 inch nominal seal face diameter.
Speed:	500-4000 RPM. 9-70 ft/sec for a 4 inch seal.
Pressure:	0-1000 psi continuous. Vessel is rated at 2000 psi.
Bearings:	Five ABEC-7 bearings on precision spindle. Bearings are rated at a maximum of 12000 lb thrust at 4000 RPM (corresponds to a 4 inch seal at 1000 psi).
Motor:	5 Hp variable speed drive (belt type).
Fluid:	Materials are selected for seawater service.
Balance:	Balance ratio of 1.0 (lower values can be used).
Seal Rings:	Zero moment design. Designed to minimize the effects of pressure caused radial taper.
Waviness:	Seal waviness is controllable by variable ring distortion. It can be moved relative to the primary ring.

Temperature: Can be controlled at any given temperature above 100°F.

Quantities Measured: Speed, pressure, temperature, waviness, torque, and leakage.

DESIGN

Figure 4-1 shows the general layout of the test apparatus. The bolted vessel on the right hand end contains the pressurized seal. Immediately to the left is the waviness drive plate and the bird cage-like torque transducer. The entire test vessel is supported cantilever style by the torque transducer. Further to the left is the bearing housing which is attached to the frame. The variable speed motor drive is located to the left of the bearing housing.

On the level below the test vessel in Figure 4-1 is located all of the auxiliary equipment. To the left end is the oil supply system including a tank, pump, filter, and cooler. On the right end is the high pressure water circulation pump heat exchanger. Beyond the machine to the right is the control panel and a rack containing torque and temperature recorders.

Figure 4-2 shows the essential features of the seal test apparatus in detail. The primary and secondary seal rings are shown as parts (27) and (31). Shaft (1) turns on five precision angular contact bearings designed to operate under the large thrust load. Cooling water is circulated through the test chamber (41) through openings not shown. The torque tranducer (11) acts as

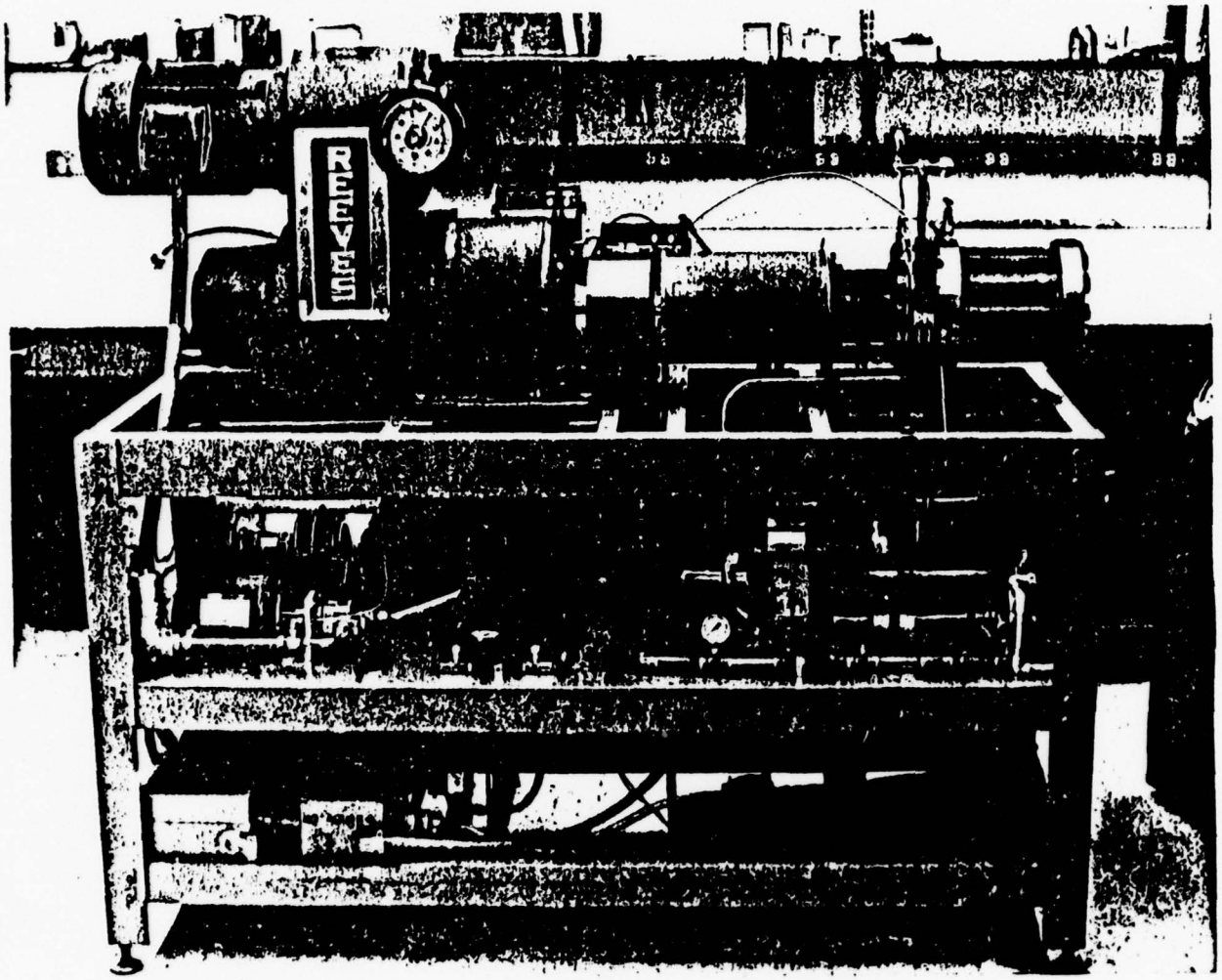

Figure 4-1. Mechanical Face Seal Test Apparatus

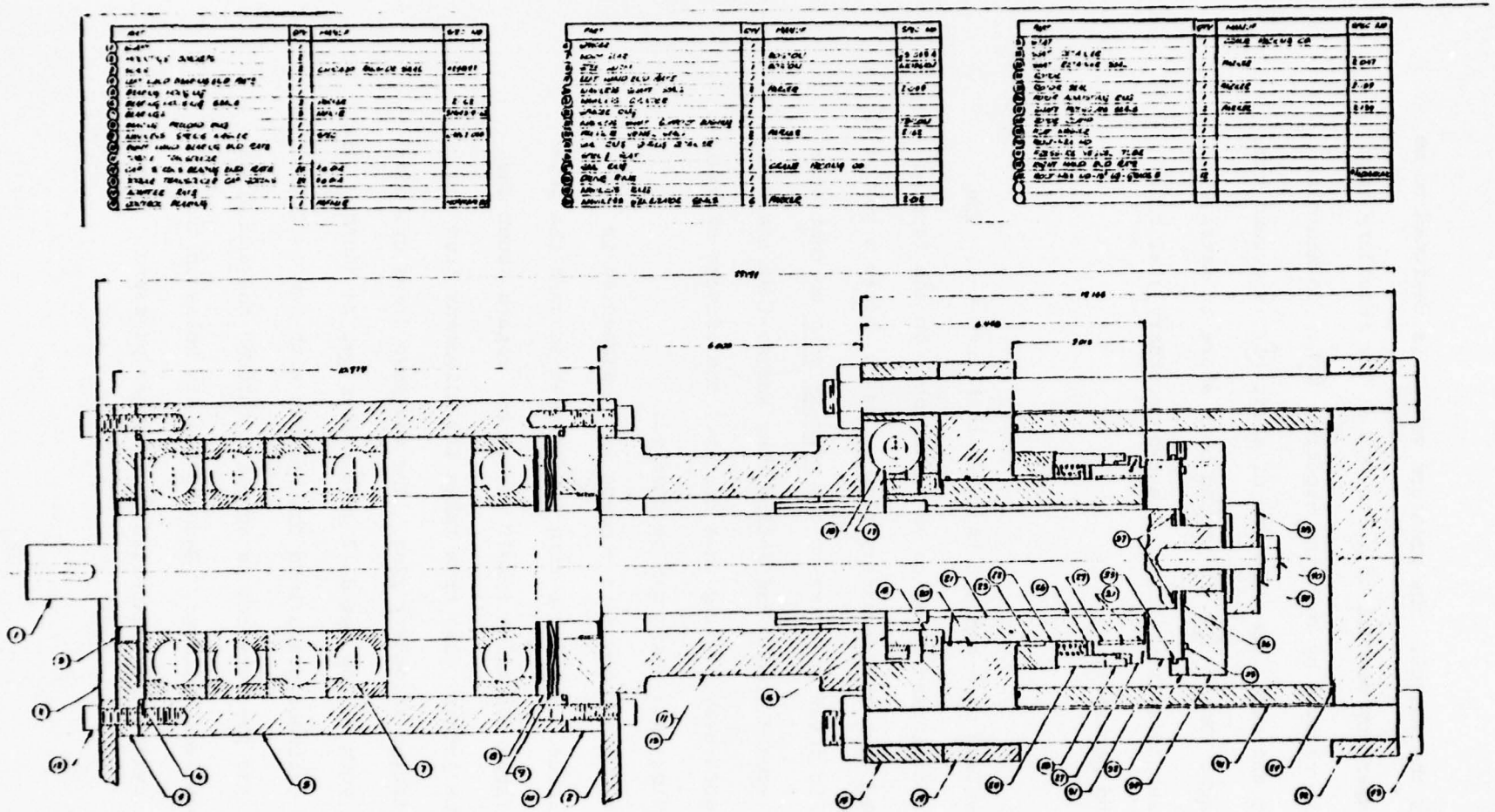

Figure 4-2. Seal Test Apparatus Assembly

the support for the vessel. The pressure vessel is designed to be readily taken apart by removal of bolts (43). The secondary ring support rotor is removed by removing capscrew (40). To minimize axial runout at the seal face, the end of shaft (1) is ground true with the bearings. Rotor (34) is ground both where it mates with the shaft and secondary seal ring. The two secondary seal ring faces are ground parallel.

Waviness Drive

The traveling wave concept is shown in Figure 4-3. The primary ring is distorted so as to cause waviness on the face of the rings when mated with the secondary ring or seat. After a period of time this wave is moved relative to the primary ring so that wear is distributed evenly around the entire ring and so that the wave is not simply worn away. Using this concept, the effects of waviness in contacting face seals can be studied.

Figure 4-4 shows how this concept was implemented in the seal test apparatus. The drive ring is designed so that the primary ring can float and align itself but cannot rotate about the shaft axis. The primary ring thus takes its alignment from the face of the rotating secondary ring. The waviness drive cylinder is driven by a worm at low speed (2 revolutions per 24 hours). The waviness drive cylinder seals into the housing with two O-rings designed so that gas pressure can be supplied through the end plate and into the waviness cylinder. Each of the six holes on the waviness drive cylinder is connected to this gas pressure. When

DISTORTED RING UNDER ZERO PRESSURE

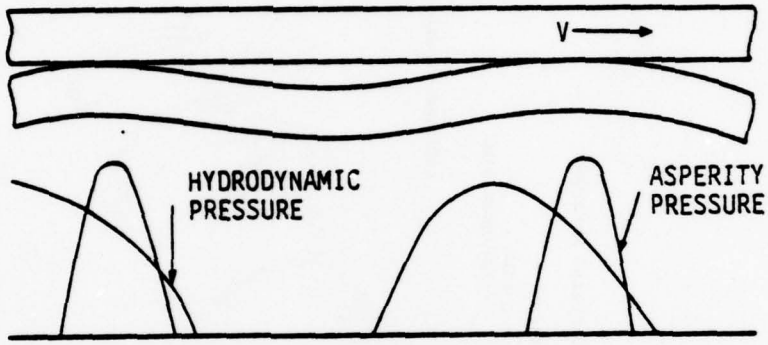

DISTORTED RING UNDER PRESSURE

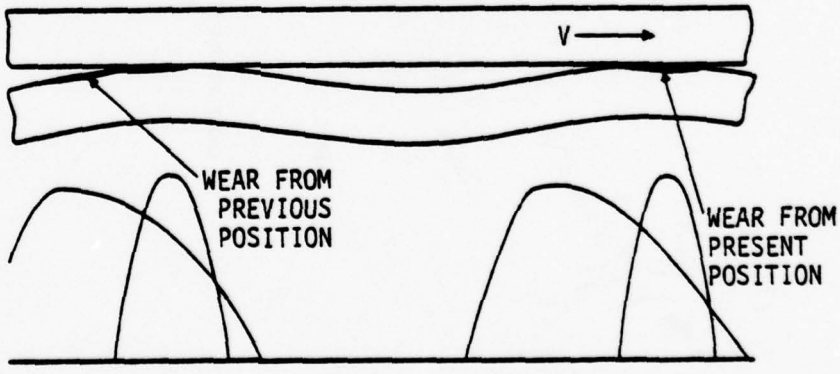

DISTORTED RING UNDER PRESSURE
AFTER WAVE HAS MOVED

Figure 4-3. Traveling Wave Concept

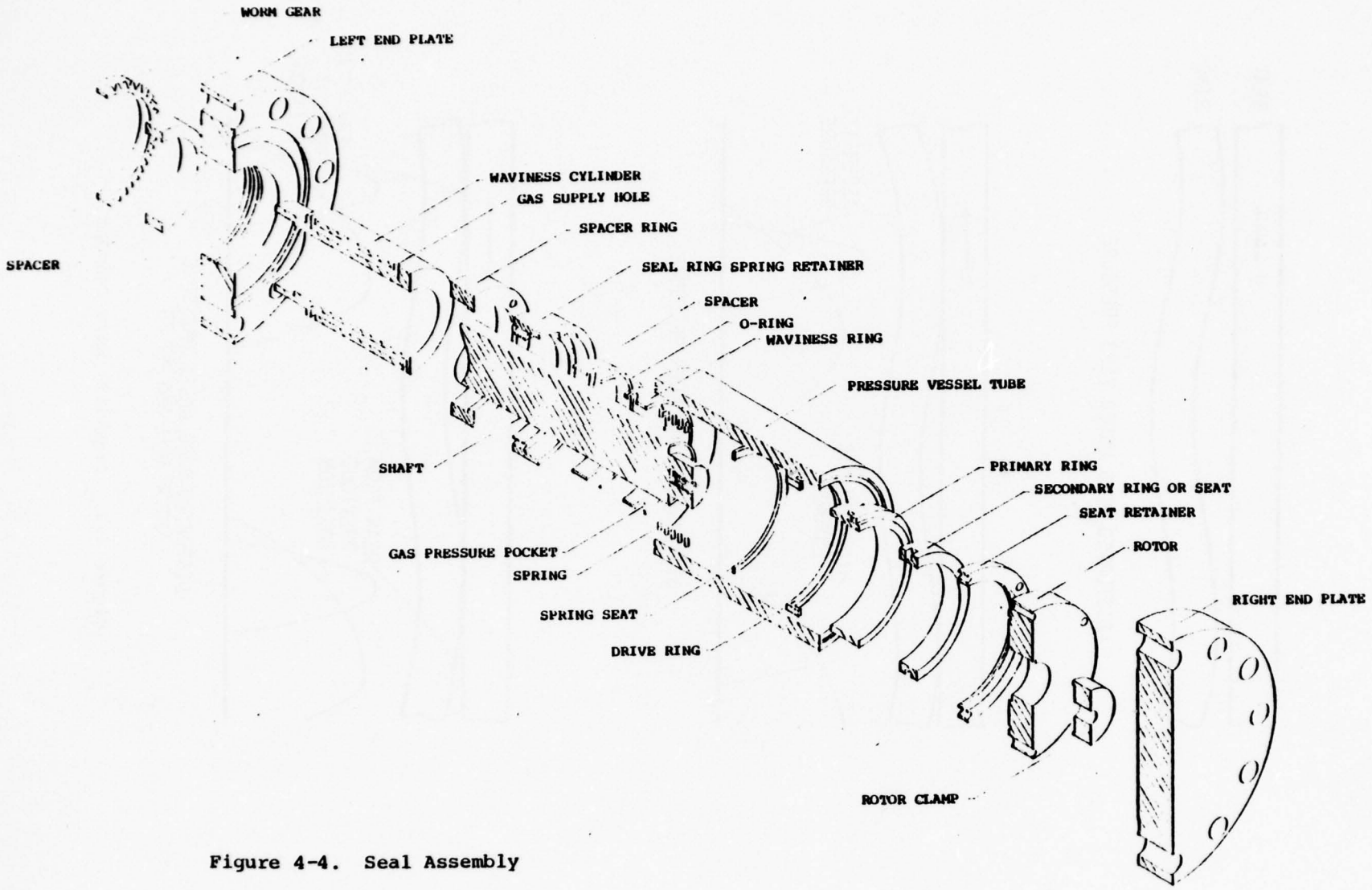

Figure 4-4. Seal Assembly

the primary ring is properly positioned over these six holes and sealed off by six O-rings, then the primary ring becomes subjected to six small regions of gas pressure on its inside. Waviness is caused by this gas pressure, because of the staggered location pattern of the six holes. As the waviness cylinder is turned by the worm, the waviness pattern moves relative to the seal primary ring. Figure 4-2 shows additional details of the waviness drive.

Also shown in Figure 4-4 is the secondary O-ring seal between the waviness cylinder and the primary ring. This O-ring seals off the gap between these two members while allowing the primary ring to float to align itself.

Primary Ring

The primary ring is shown in Figure 4-5. The material selected for initial tests is Pure Carbon P658RC. The unusual proportions of the ring result from adjusting the geometry so that no rotation about a circumferential axis is caused by pressure variation. The primary ring is driven by lugs which engage two notches. Two as opposed to a greater number of notches were used because this arrangement gives the primary ring maximum freedom to float radially. Second harmonic waviness is minimized by driving the ring through the centroid of its cross section. Any remaining second harmonic waviness produced by drive forces will be easily flattened compared to the third harmonic waviness forced into the ring, so is not considered important. The secondary seal is located at the left end on the inside diameter. The balance ratio for the design shown is unity. Springs to the left of the seal provide preload.

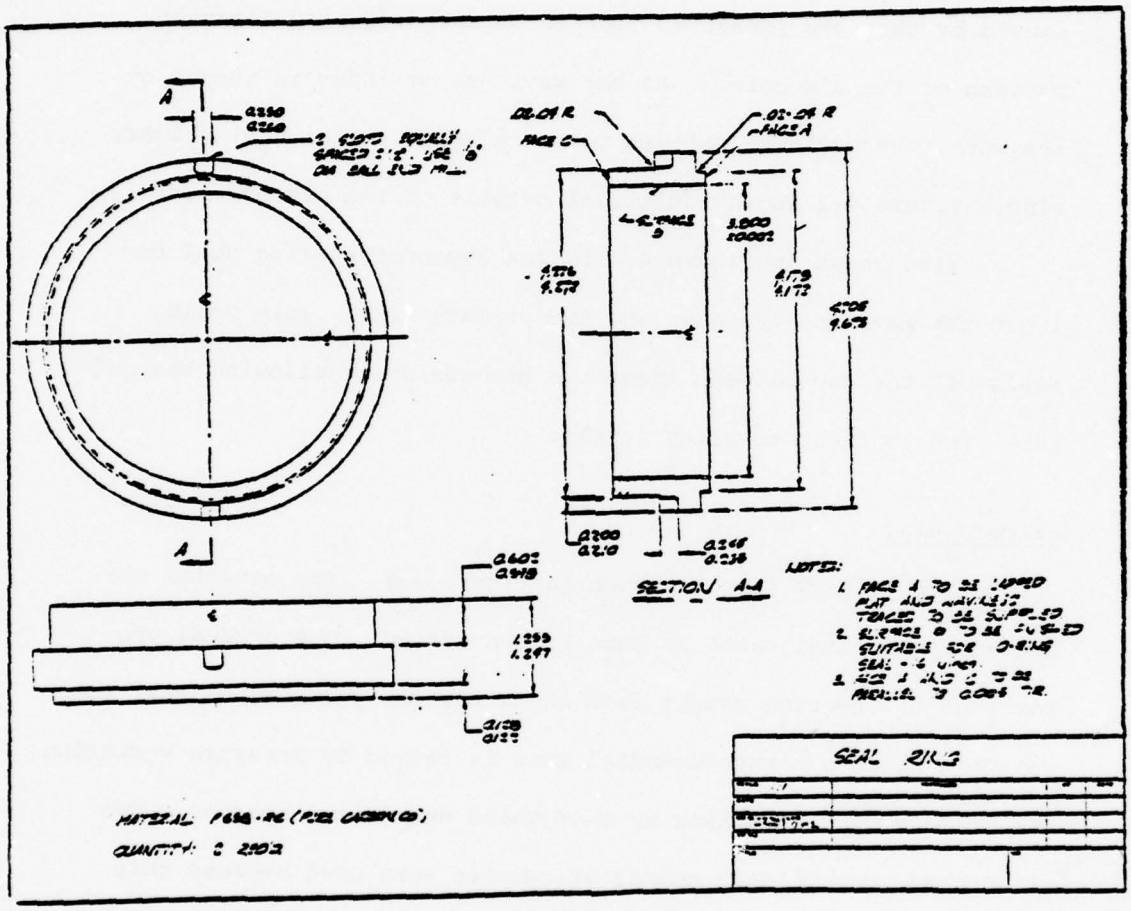

Figure 4-5. Primary Ring

Secondary Ring

The secondary seal ring is shown in Figure 4-6. Rings are fabricated from tungsten carbide and ceramic. This ring is also of a zero pressure moment design. An unusual feature of the particular design is that the mechanical force at the right hand side of the seal has been reduced to nearly zero by placing the O-ring seal on the right hand face as opposed to the outside diameter (see Figure 4-2). It is useful to minimize the axial force to reduce coning effects caused by friction at the load bearing point in conjunction with radial deformation due to pressure and temperature. The secondary seal ring is held in place by spring clips (not shown) which engage the notches shown in Figure 4-6.

Torque Transducer

The torque transducer is shown in Figure 4-7. The difficulty in designing such a torque transducer is that torque to be measured is small whereas the axial load due to the thrust of the seal is large. Several design concepts were developed. Figure 4-7 shows what appears to be the best compromise. The 0.120 × 1 inch members carry the axial load in tension. Due to their small moment of inertia about a radial axis, these members have in combination a low torsional stiffness. The torsion load is sensed by the two reduced section beams. Strain gages are attached to these members as shown. The axial load effect is isolated from these members by the cutout shown. The torque transducer does have some small amount of sensitivity to axial loads because the

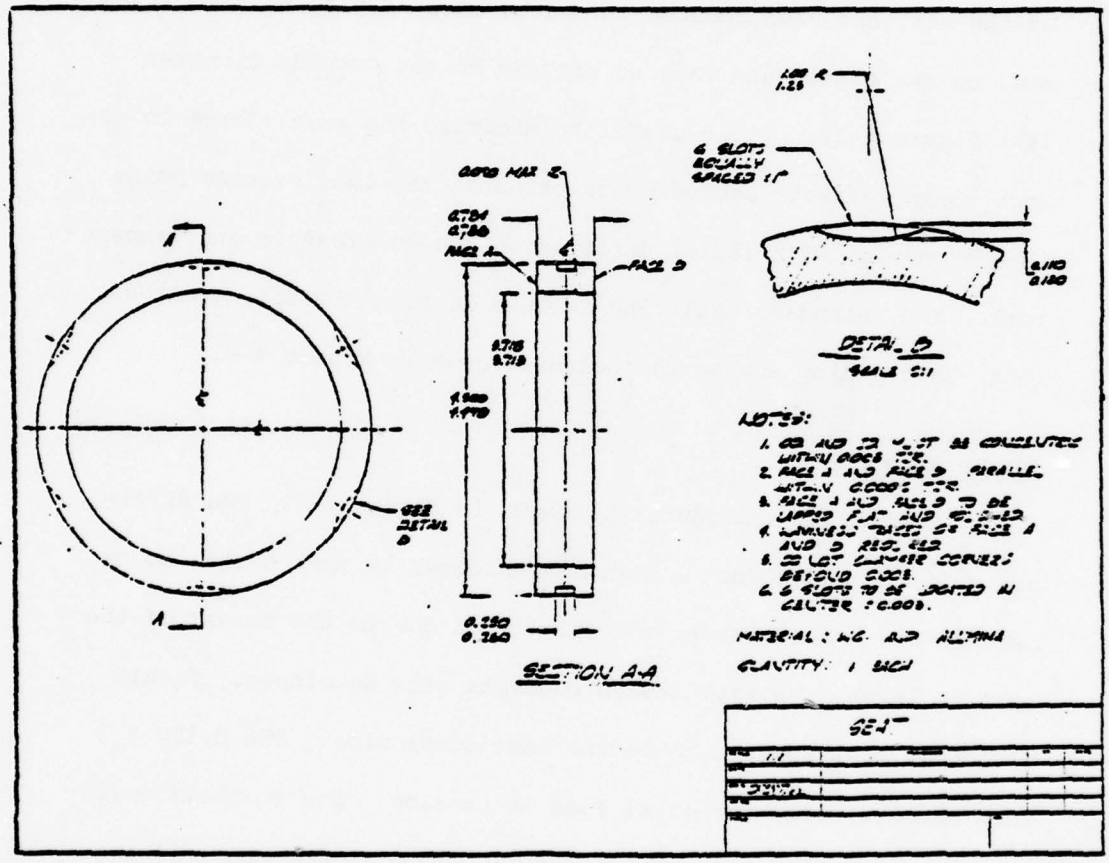

Figure 4-6. Secondary Ring

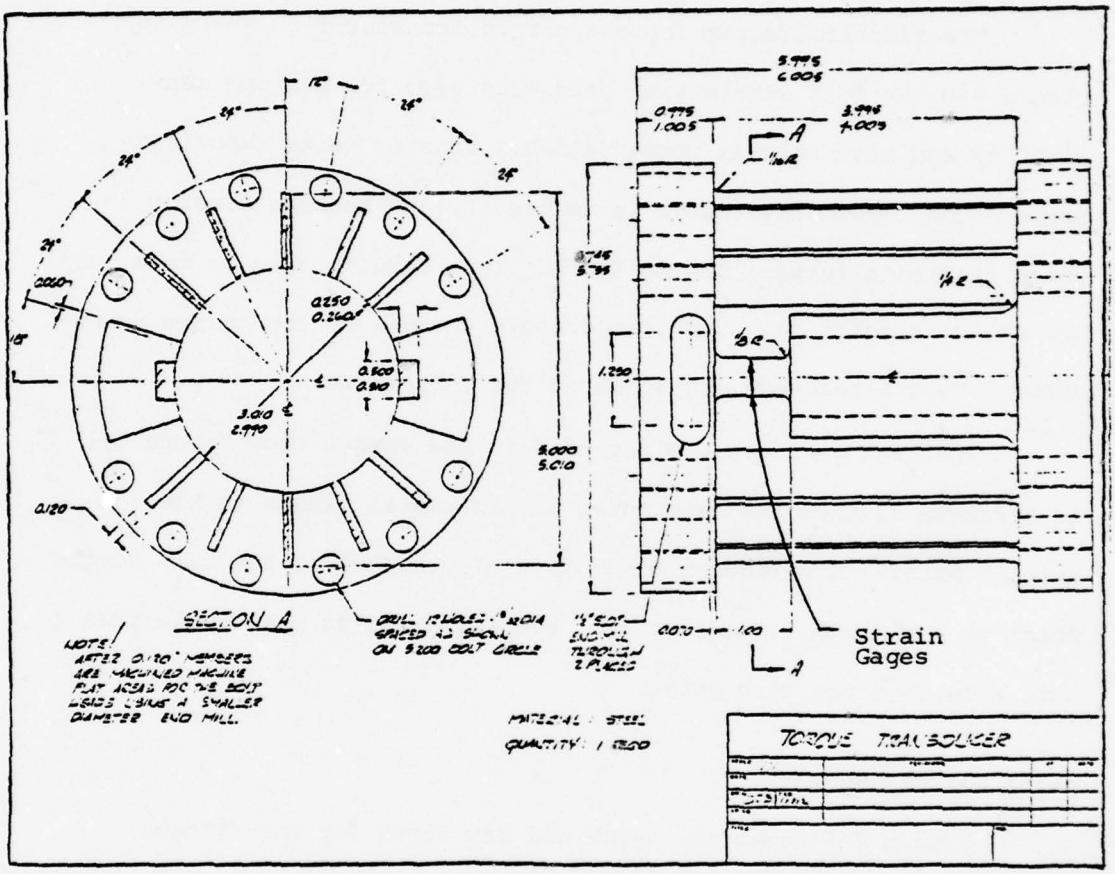

Figure 4-7. Torque Transducer

0.120 × 1 members do attempt to straighten (when twisted) due to the axial load. This effect is largely offset by the fact that the torque sensing beams have a very high torsional stiffness. Thus the actual torsional deformation of the unit is quite small.

The circuit diagram for the torque transducer is shown in Figure 4-8. A full strain gage bridge is used for maximum sensitivity and best thermal compensation. This is quite important because the torque transducer is mounted to the bearing housing which reaches a temperature of 150°F. Test results show up to a 7.5 in. lb. zero shift caused by temperature changes of the torque transducer. Torque readings are adjusted for this shift.

The high pressure cooling feed to the vessel (see Figure 4-1) is arranged so that the feed tubes are in radial planes to the machine axis. This reduces the effect of pressure on the zero torque point to a minimum. Tests so far have indicated no measurable pressure effect on the zero point.

Water and Gas Systems

Figure 4-9 shows the water and gas flows for the system. Entering water passes through valve V2. V2 is electrically controlled to shut off in the event of major leaks in the system. On the low pressure water side of the system, cooling water is regulated by servo valve MV1 and then passes through the low pressure side of heat exchanger HX1 and then returned to a drain.

On the high pressure water side, water is pressurized by air driven pump P1 which is controlled by electrically operated

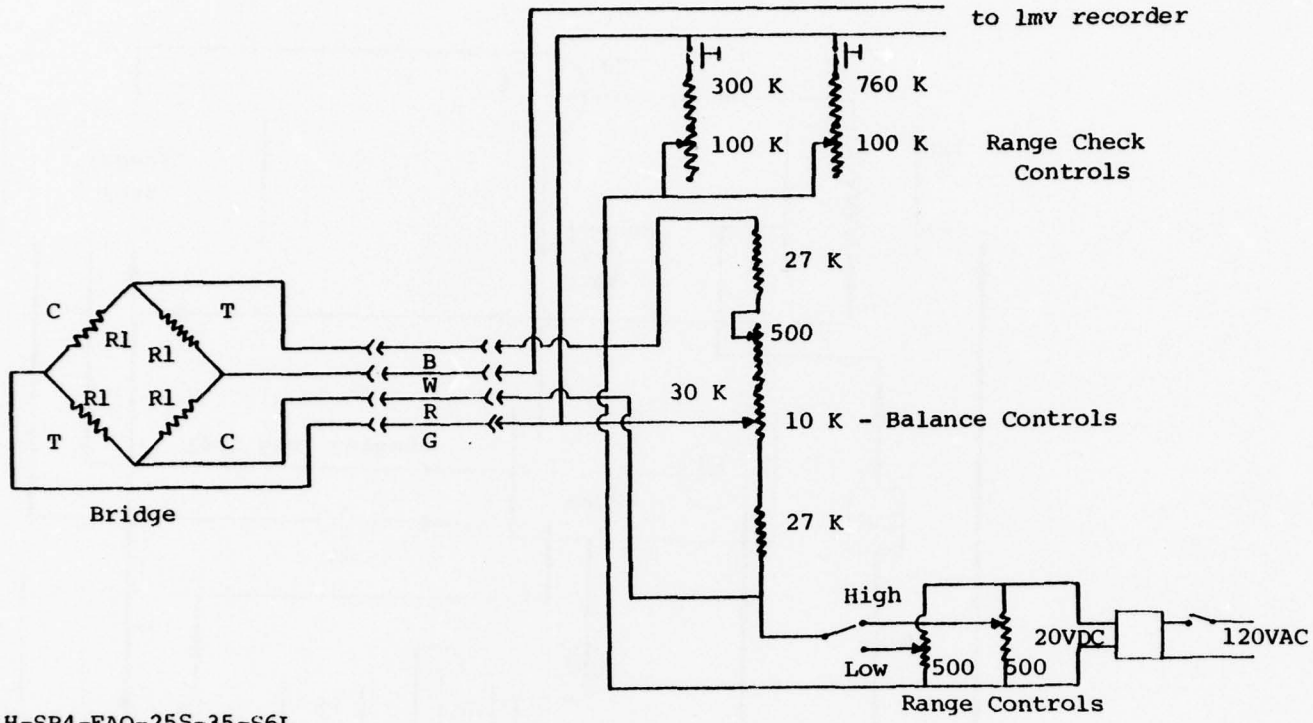

Rl = BLH-SR4-FAQ-25S-35-S6L
Strain gages

Figure 4-8. Torque Transducer Circuit

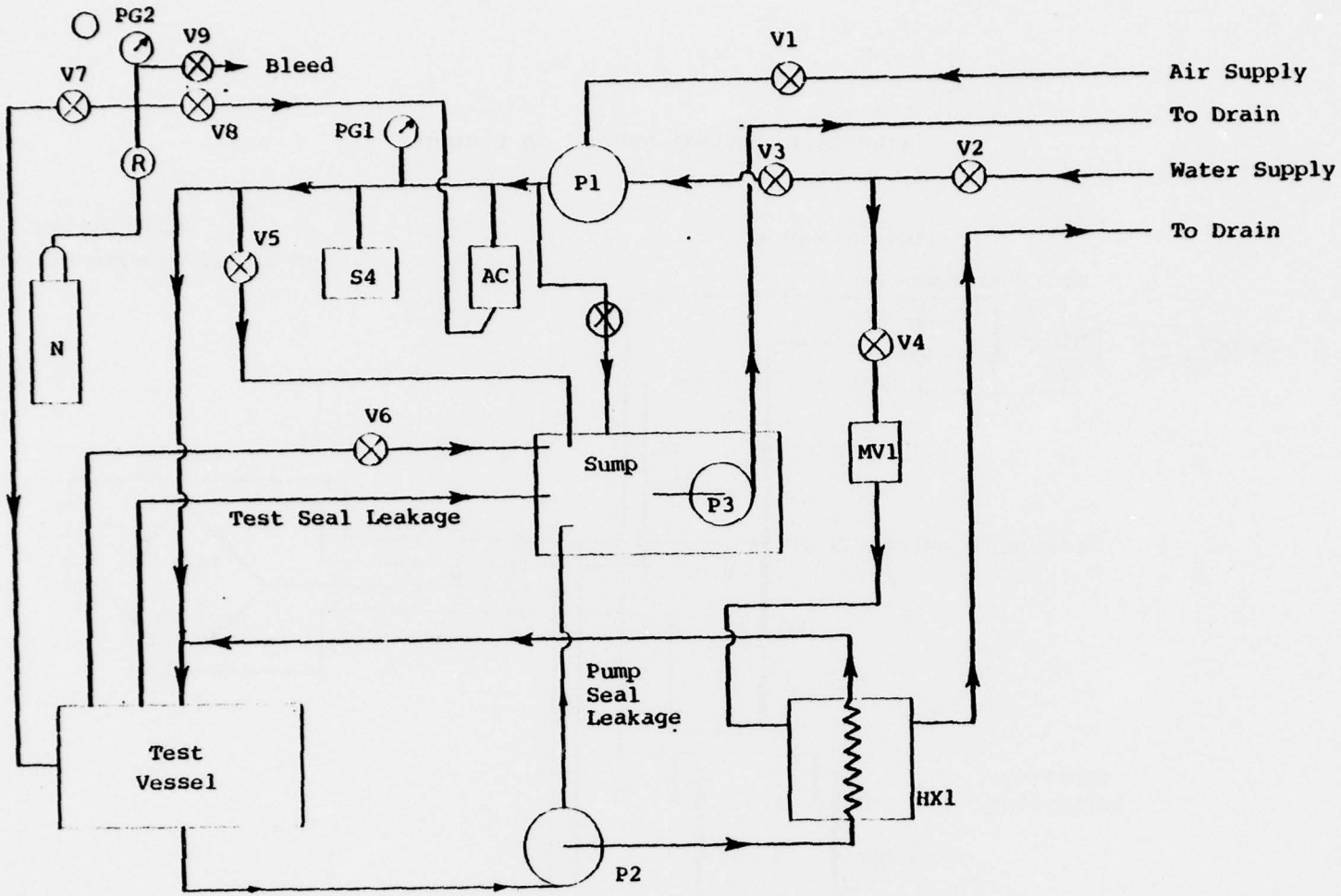

Figure 4-9. Water and Gas Systems

Figure 4-9 (continued) Water and Gas Systems

V1 - High Pressure Water Pump Electric Solenoid Air Valve, Dayton 6X080, 1/4"

V2 - Leak Detector Water Shutoff Solenoid Valve, Dayton 6X082, 1/2"

V3 - Water Supply Valve, 1/4" Gate

V4 - Water Supply Valve, 1/2" Gate

V5 - High Pressure Drain, 1/4", 3000 psi, Nupro Stainless

V6 - High Pressure Bleed, 1/4", 3000 psi, Nupro Stainless

V7 - Waviness Gas Supply, 1/4 Needle, Alkron

V8 - Accumulator Valve

V9 - Accumulator Bleed Valve, 1/4 Needle, Alkron

P1 - Air Pump - Hydraulic Engineering Co., SC10-500-16

P2 - Circulation Pump w/High Pressure Inlet Centrifugal type

P3 - Sump Pump Centrifugal Type AMXCO 1/60 HP

AC - Accumulator, Bladder Type Hydrill K 1/4-3000 w/K31 plastic coating

PG1 - 0-2000 psi Gage

PG2 - 0-2000 psi Gage

MV1 - Temperature Control Servo Valve Honeywell V5011A-1106 1/2"

HX1 - Heat Exchanger Heliflow 4-X6C-10 tube and shell type

R - Gas Regulator CGA580

N - Nitrogen Supply Bottle

SV1 - Blow Out Safety Valve Nupro 1200 psi diaphragm

S4 - High Pressure Controller, 100-1000 psi Honeywell P634A

air valve V1 which in turn is controlled by pressure controller S4. Accumulator AC is charged with nitrogen to 75% of operating pressure. This reduces pressure surges on the system. This high pressure supply system is required to only make up water that has been leaked out of the system by the pump seal or the test seal.

The high pressure water supply is connected to the cooling water circulation loop as shown. Cooling water passes through the tube side of HX1 and is circulated through the test vessel by circulation pump P2. Leakage and vessel drains are collected in a sump and pumped back to a drain.

SV1 is a burst diaphragm type of safety valve to protect the system from overpressure in the event of a control failure.

High pressure nitrogen gas is supplied by a bottle and regulator to either charge the accumulator or to pressurize the waviness cylinder.

High Pressure Circulation Pump

The high pressure circulation pump was designed and built especially for the project. This was done because of the unavailability of centrifugal pumps that can withstand a high inlet pressure. The distinctive feature of the circulation pump shown in Figure 4-10 is its heavy walled 316 stainless steel housing.

Oil System

Figure 4-11 shows the oil lubrication system which includes a pump, filter, air cooled heat exchanger, and tank. Switch S2 shuts down the entire test apparatus in the event of low oil pressure.

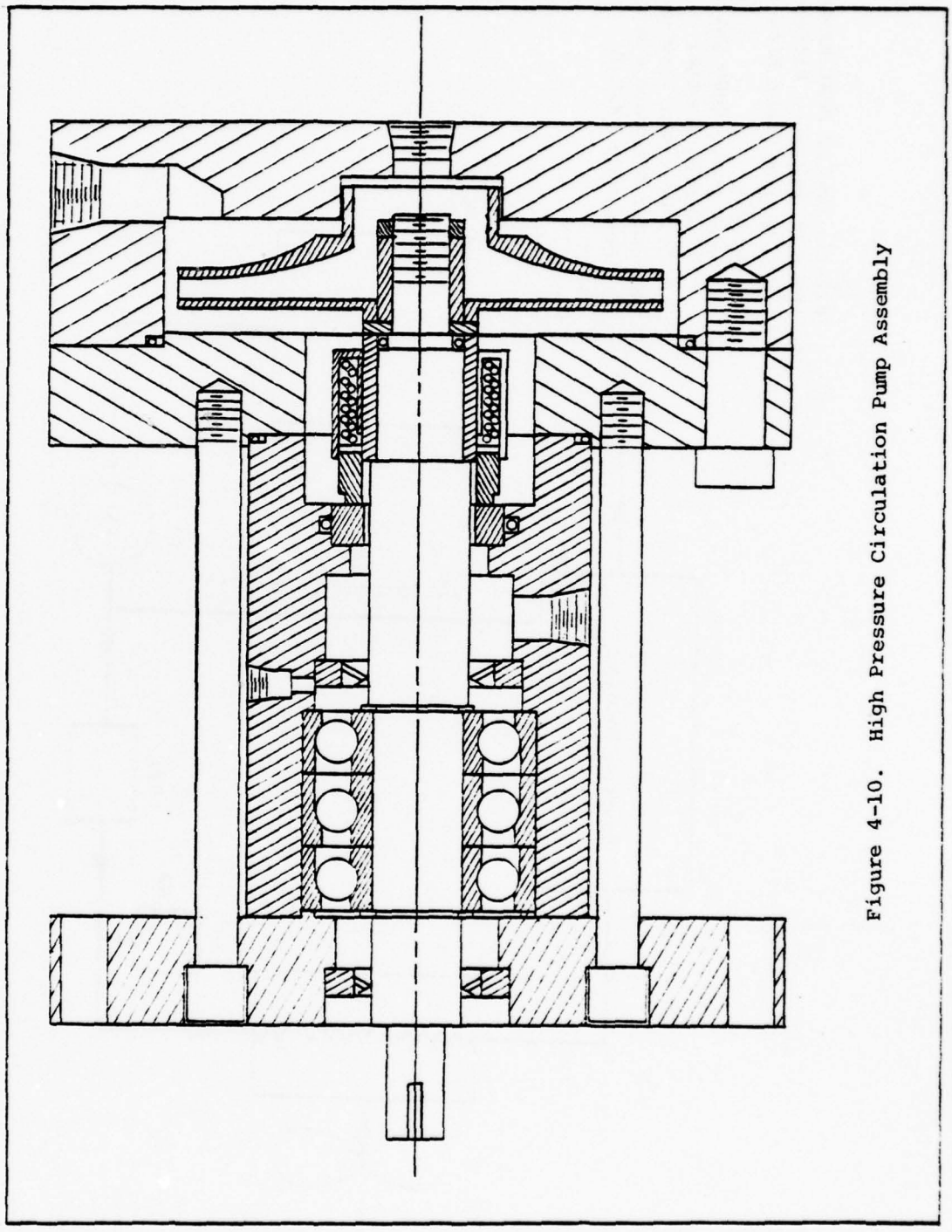

Figure 4-10. High Pressure Circulation Pump Assembly

HX2-Air Cooled Heat Exchanger
F1-High Pressure Filter-
5 Micron Paper Element,
Bendix
P4-Gear Pump, 2000 psi @
1750 RPM, Wooster
R1-Oil Reservoir - 8 gal.
S2-Under Pressure Control
Honeywell PA404B

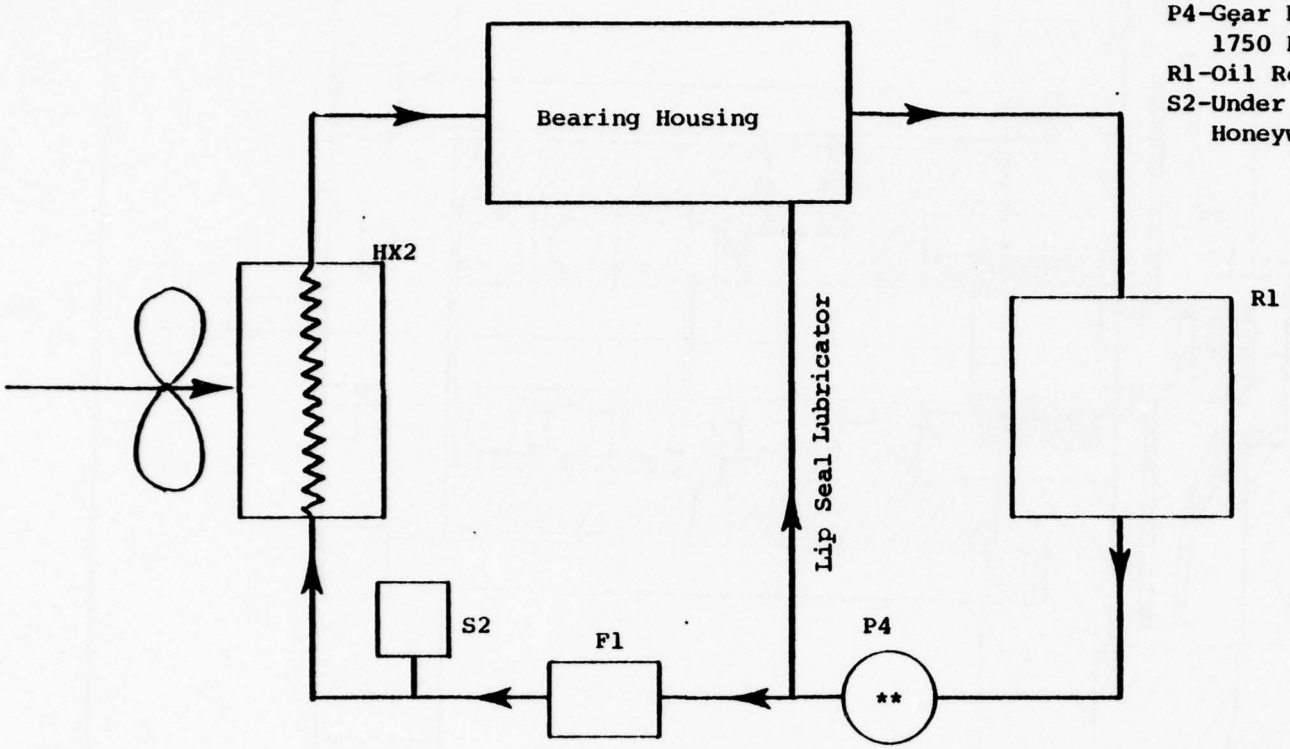

Figure 4-11. Oil Lubrication System

Control Cabinet

Figure 4-12 shows the circuitry designed for the remote control cabinet. Switches S6 through S10 actuate the various motors and pumps on the machine. The coil on REL3 is connected in series with several important safety devices. This coil is deenergized in the event of oil under pressure (Switch S2 on Figure 4-13), oil over temperature (CTL1), seal over temperature (CTL2), or a water leak (REL4). When REL3 is deenergized, all systems (all motors and pumps) are shut off. CTL3 is the controller for MV1 in Figure 4-9. Seal cooling water, seal face, and oil temperature are monitored by thermocouples connected to the three controllers. The coil of REL4 is connected to several salt soaked and dried probes placed around the machine. The probes become conductive when contacted with water, so the circuit shuts the machine down in the event of a major water leak.

Machine Electrical Circuit

Figure 4-13 shows the various electrical components which are mounted on the machine itself. The larger motors are operated through motor starters REL5, REL6, and REL7, which include overload protection.

SEAL TEST PROCEDURE

The following procedure for using the apparatus and testing a seal has been established.

1. Warm up torque transducer for about two hours. With secondary seal ring removed, the bolt-tightening bracket

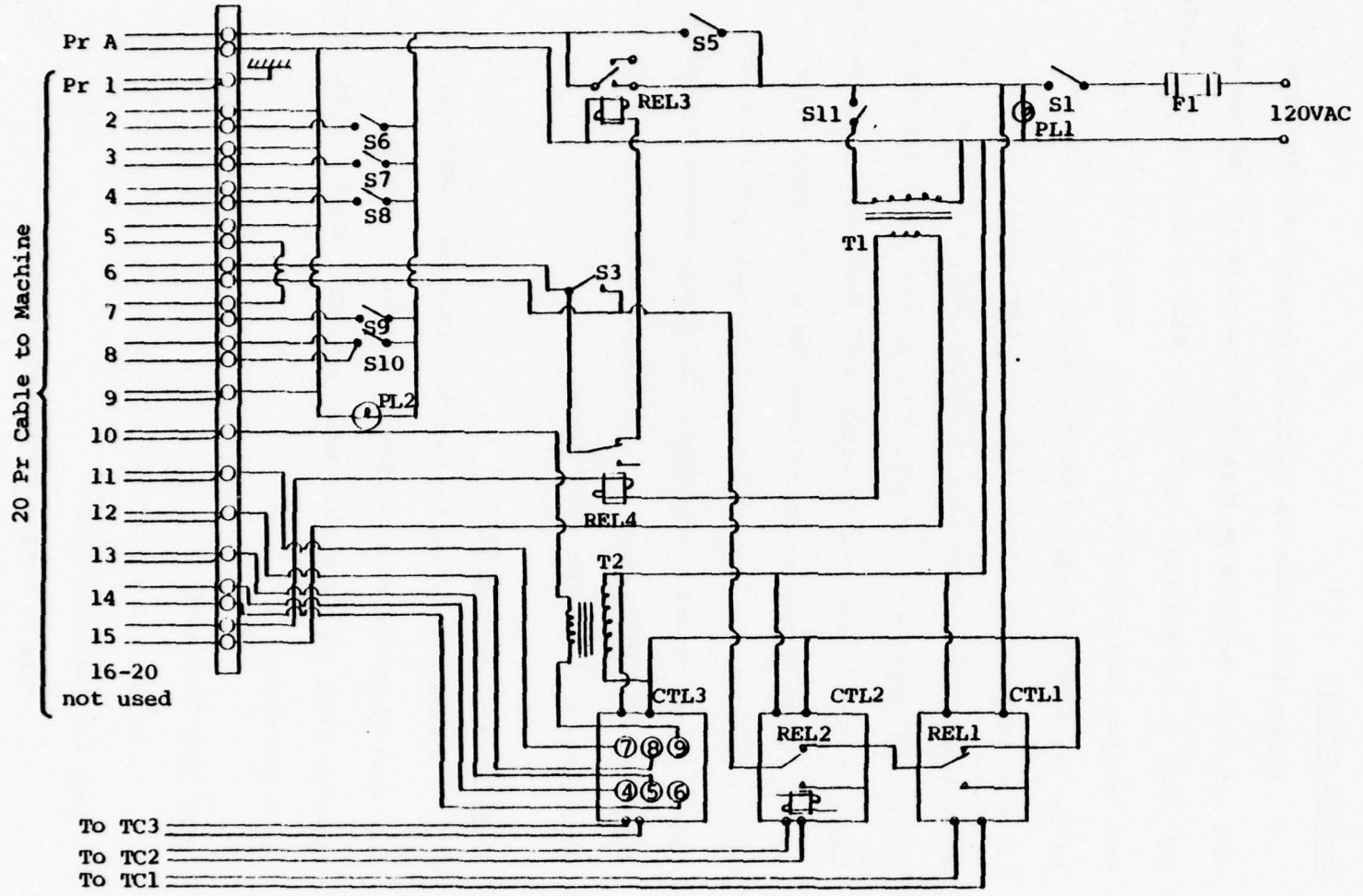

Figure 4-12 Control Cabinet Circuit

Figure 4-12 (continued) Control Cabinet Components

S1 - Main Switch, SPST key operated

S3 - Low Oil Pressure Override Switch - SPST spring toggle

S5 - Safety System Override Switch - SPST toggle

S6 - Drive Motor Switch - SPST toggle

S7 - Water Circulation Pump Switch - SPST toggle

S8 - Oil Circulation Pump Switch - SPST toggle

S9 - High Pressure Water Pump Switch - SPST toggle

S10 - Waviness Drive Switch - SPST toggle

S11 - Leak Detector Switch - SPST toggle

REL1 - SPDT Relay in CTL1

REL2 - SPDT Relay in CTL2

REL3 - Safety System Relay - SPDT 120 VAC

REL4 - Leak Detector Relay - SPDT 24 VAC

PL1 - Pilot Light

PL2 - Pilot Light

T1 - Leak Detector Transformer - 24 VAC

T2 - Cooling water servo transformer - 24 VAC

F1 - Fuse

CTL1 - Oil Overtemperature Control

West Model 10 0-300°F

CTL2 - Seal Face Overtemperature Control

West Model 10 0-500°F

CTL3 - Cooling Water Temperature Control - Honeywell

Dialatrol R7352

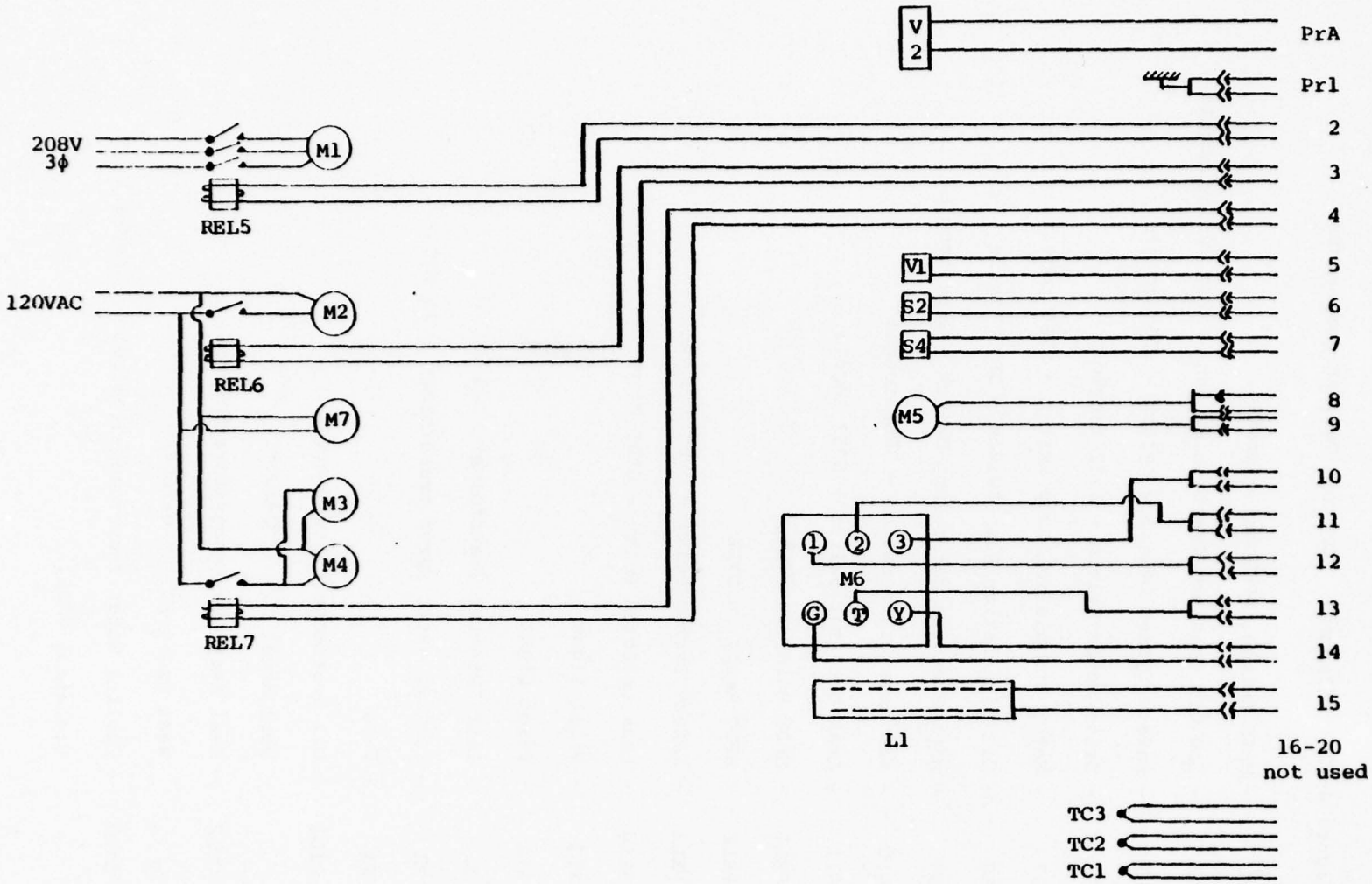

Figure 4-13. Machine Electrical Circuit

Figure 4-13 (continued) *Machine Electrical Circuit*

M1 - Drive Motor, Reeves Vari-speed Motodrive Model 400

M2 - Water Circulation Pump Motor, Emmerson JP540, 1 HP, 3450 RPM

M3 - Oil Pump Drive Motor, Dayton 1725 RPM, 1/6 HP

M4 - Cooling Fan Drive Motor, 1/40 HP, 1470 RPM

M5 - Waviness Drive Motor, Dayton Gear Motor 6K301, 1/15 HP, 30 RPM

M6 - Cooling Water Control Servo Motor, Honeywell M944B, Modutrol Motor

M7 - Sump Pump Drive Motor AMXCO, 1/60 HP, 3000 RPM

S2 - Oil Under Pressure Switch, Honeywell PA404B, 1023 2

S4 - Water Pressure Control Pressure Switch, Honeywell P634A

V1 - High Pressure Water Pump Electric Solenoid Air Valve, Dayton 6X080, 1/4"

V2 - Leak Detector Water Shutoff Solenoid Water Valve, Dayton, 6X082, 1/2"

L1 - Leak Detector. Electrodes insulated by dry salt soaked paper

REL5 - Drive Motor Starter, Dayton

REL6 - Water Pump Motor Starter, Dayton

REL7 - Oil Pump and Fan Motor Starter, Dayton

TC1 - Thermocouple in Oil Return Line - Type J, Omega

TC2 - Thermocouple Beneath Seal Face - Type J, Omega

TC3 - Thermocouple in Water inside Pressure Vessel, Type J, Omega

removed, and all plumbing and hoses hooked to test vessel, balance the bridge to find zero torque. Lock all settings. Using the calibration stand, check range calibration and lock all settings. The torque transducer is to be left on for the entire duration of the test.

2. Lap and polish the carbon and secondary ring faces. Check flatness using an optical flat. Flatness should be within one light band across the width of the face. Waviness should be within two light bands.
3. Make total roughness and CLA traces of the lapped and polished faces.
4. Mark six equal spaces around the carbon ring and number one through six. Using an appropriate diameter dowel pin, determine nose height to 0.0001" or better.
5. Install seal rings making certain that all O-rings are in place and greased. Wipe face of seal and adjacent area completely free of grease before final assembly. Make certain that proper shaft spacer is used to compensate for wear.
6. Install thermocouples making certain that they are clamped in position so as not to vibrate and wear.
7. With seal dry and spring load only, measure and record the friction torque using the hand crank to turn the machine.
8. Install bolt-tightening bracket. Install pressure vessel and tighten bolts to 100 ft. lb. Remove bolt-tightening brackets.

9. Charge accumulator to 75% of operating pressure and then close accumulator valve, being careful not to overtighten valve.
10. Turn on main central switch. Start oil pump. This will allow other equipment to be operated. Turn on all water valves. Water valve to high-pressure pump should only be cracked. All other valves should be full on. Set oil temperature trip to 160°F and seal temperature trip at 50°F above water temperature. Set water temperature.
11. Crack two bleed valves, one below and one above. Start water circulation pump. Allow water to flush system completely until all air is driven out. Turn off lower bleed drain valve and the upper bleed valve. System is now ready for pressure. Do not run water circulation pump dry.
12. Turn on high-pressure pump. System pressure will come up.
13. Using hand crank, measure and record seal torque.
14. Fill leak cavity with water using a small diameter flexible tube.
15. Apply waviness pressure if any.
16. Measure static leakage if any.
17. Start chart recorders, and check pens and paper supply.
18. Start drive motor, bring up to operating speed and check speed.
19. Mark time zero on charts and check leakage on graduated cylinder.

20. Observe that system temperature stabilizes.

21. Record leakage as necessary. Record steady state oil temperature to be used for torque zero shift corrections.

22. Run machine for given test duration

23. After test is completed, reduce drive speed to low and turn off all systems except torque transducer. Drain pressure vessel and system. Mount bolt-tightening bracket. Remove vessel and seal assembly. Note wear condition of seal.

24. Remove bolt-tightening bracket and note zero torque position. Compensate for temperature if any.

25. Using previously outlined technique, measure nose height of carbon seal ring. Measure wear on secondary ring by making several traces across entire width of face.

26. Make total roughness and CLA measurements in radial and tangential directions for both rings. Make traces diametrically across both rings.

27. Correct and average torque data. Compile all data for test.

EXPERIMENTS

Several different series of experiments have been planned using the test apparatus.

1. Verify the waviness model by experiment.

Using the seal test rig, experiments will be conducted to confirm the basic predictions made by the model. First, the effect

of waviness amplitude on friction and leakage will be determined. The effect of waviness on wear rate will be established by comparing the wear rate for a wavy seal to the wear rate for a flat faced seal. Hydrodynamic seal performance as a function of pressure and speed will also be established. The effect of surface roughness on hydrodynamic lubrication will be established by modifying the natural surface roughness of the mating faces. This can be achieved by introducing abrasives into the seal system. Surface characterization will be performed using a surface analyzer.

2. Demonstrate the traveling wave design concept.

In order to take advantage of waviness to reduce friction and wear, it is necessary to move the wave relative to the seal face. The test rig seal has this capability, so the results from (1.) will also serve to demonstrate the advantages and practicality of this concept.

3. Experimentally verify a hydrostatic seal model.

Reference [23] presents a mixed friction hydrostatic seal model which includes radial taper and wear. This model has been shown to theoretically predict important seal behavior on a qualitative basis. Thus, it is thought that this model will be very useful in predicting the performance of non wavy face seals. In order to become accepted as a useful tool, the model needs to be subjected to experimental testing.

The seal test rig will be modified so as to produce a controllable radial taper. This is easily accomplished, given the design of the test rig. With this feature it will be possible to

verify the basic features of the model in Reference [23]. In addition, tests will be run to determine the time dependent behavior of a radially tapered seal and to compare these results with the model of reference [23].

4. Conduct Experiments at High Seal Temperatures.

Reference [24] indicates that from the standpoint of reduced friction and wear, face seals perform better at operating temperatures near the boiling point of the sealed fluid than at lower temperatures. This behavior has been explored only on a limited experimental basis [25]. Given the possibility of improved seal life and reduced friction, the two phase seal model of reference [24] will be examined on an experimental basis. The test apparatus as designed has this capability, except that a heating loop may be required to maintain the higher temperatures.

MODIFICATIONS AND ADDITIONS

So far the test apparatus has operated as designed. No major operational difficulties have been encountered to date, so major changes in design are not anticipated. However, certain refinements and improvements are expected to be added in the future. These include the use of a data acquisition system based on the HP6940B multiprogrammer in conjunction with a HP9835 computer. Pressure control will be taken over by this system to provide a more accurate control. Leakage measurement will be made automatic using this system. Data will be stored on tape. The data can be immediately analyzed after a test run using the computer and then

be presented in graphical form or printed form for further interpretation.

The above data acquisition system will also be used to analyze the surface roughness data produced by the surface analyzer. Statistical characteristics of the surface are needed in conjunction with studies of the effect of roughness and questions related to roughness modeling.

CONCLUSIONS

Based upon the work presented in Chapter 2, the Christensen [20] and Tonder [21] model for isotropic roughness leads to conservative predictions of hydrodynamic load support. Thus, the results given in Reference [1], the previous annual report, theoretically underestimate the percent hydrodynamic load support, and can be considered quite useful for predicting a lower bound on hydrodynamic effects in the presence of roughness.

A truncated roughness model was studied. By making certain assumptions, this model avoids certain fundamental questions that have been raised, while still providing a theoretically sound model for roughness effects. Results based upon this model show a higher percentage of hydrodynamic load support than the previous model. However, experimental data is needed as to the proper truncation level to be used with this model. This data will be supplied by a testing program currently underway.

In Chapter 3 a design procedure for a contacting hydrodynamic face seal was developed. At lower numbers of waves it was shown that stability problems may be encountered, while at higher numbers of waves, these are limitations imposed due to the physical impossibility of imposing a large enough waviness. While this procedure is not final and will require modifications and further theoretical and experimental progress is made, the method clearly shows the details of how design parameter values are selected to produce the theoretical performance obtainable using the hydrodynamic contacting seal concept. In the example studied, a wear reduction of 17:1 compared to a flat face seal was shown possible.

One of the important questions remaining is whether or not sufficiently small operating surface roughness can be obtained to permit the type of hydrodynamic operation described. This question requires an experimental answer.

Finally in Chapter 4, the experimental test apparatus is described in detail. This apparatus will be used to study the hydrodynamic effects above as well as certain hydrostatic effects. The apparatus operates as designed and is currently being used in a test program to evaluate the effects of waviness on seal performance.

PUBLICATIONS

Several publications have resulted from this research program during the past three years. Two annual reports, references [1] and [5] were produced. Two papers, [26], [27] based upon the first one and one half year's work were presented and published. Based primarily upon work performed during the current contract year, two Master's theses [28], [29] have been completed. These results have been presented as parts of Chapters 2 and 3. A paper is being written based upon one of these theses [28]. A paper is also being written based upon the results in the second annual report [1].

During this writer's Sabbatical year, two papers [23], [24] were written and submitted on certain hydrostatic effects in face seals. Although the research for these papers was not performed as a part of this contract, the subject matter does stem from the contract research, and can be considered as a contribution to the total effort on seal research.

During September 1978 a presentation on seal theory was made at the NASA Lewis Seals Workshop.

REFERENCES

1. Lebeck, A. O., Teale, J. L., and Pierce, R. E., "Hydrodynamic Lubrication with Wear and Asperity Contact in Mechanical Face Seals," Annual Report ME-86(78)ONR-414-1, January 1978, Prepared for the Office of Naval Research under Contract No. ONRN-00014-76-C-0071.

2. Findlay, J. A., "Cavitation in Mechanical Face Seals," Transactions of the ASME, Journal of Lubrication Technology, April 1968, pp. 356-364.

3. Pape, J. G., "Fundamental Aspects of Radial Face Seals," Thesis WJHD-17, December 1969 (T. H. Delft, Netherlands), 172 pp.

4. Stanghan-Batch, B., and Iny, E. H., "A Hydrodynamic Theory of Radial Face Seals," Journal of Mechanical Engineering Science, Vol. 15, No. 1, 1973.

5. Lebeck, A. O., Teale, J. L., and Pierce, R. E., "Elastohydrodynamic Lubrication with Wear and Asperity Contact in Mechanical Face Seals," Annual Report ME-76(77)ONR-414-1, ONR Contract N-00014-76-C-0071, Bureau of Engineering Research, The University of New Mexico, Albuquerque, New Mexico, January 1977.

6. Cheng, H. S., and Patir, N., "An Average Flow Model for Determining Effects of Three-Dimensional Roughness on Partial Hydrodynamic Lubrication," Journal of Lubrication Technology, Trans. ASME, Series F, Vol. 100, January 1978, p. 2.

7. Tzeng, S. T., and Saibel, E., "Surface Roughness Effect on Slider Bearing Lubrication," ASLE Trans., Vol. 10, 1967, p. 334.

8. Christensen, H., "Stochastic Models for Hydrodynamic Lubrication of Rough Surfaces," Proc. Instn. Mech. Engrs., Tribology Group 184, Part 1, Vol. 55, 1969-70, p. 1013.

9. Christensen, H., "A Theory of Mixed Lubrication," Proc. Instn. Mech. Engrs., Tribology Group, Vol. 186, 1972, p. 421.

10. Ostvik, R., and Christensen, H., "Changes in Surface Topography with Running-In," Proc. Instn. Mech. Engrs., Vol. 183, Pt. 3P, 1968-69, p. 57.

11. Christensen, H., and Tonder, K., "The Hydrodynamic Lubrication of Rough Bearing Surfaces of Finite Width," Journal of Lubrication Technology, Trans. ASME Series F, Vol. 93, 1971, p. 324.

12. Elrod, H. G., "A Review of Theories for the Fluid Dynamic Effects of Roughness on Laminar Lubricating Films," presented at the 4th Leeds-Lyon Symposium on Lubrication, September 1977.

13. Elrod, H. G., "Thin-Film Lubrication Theory for Newtonian Fluids with Surfaces Possessing Striated Roughness or Grooving," Journal of Lubrication Technology, Trans. ASME, Series F, Vol. 95, No. 4, October 1973, p. 484.

14. Sun, D., and Chen, K., "First Effects of Stokes Roughness on Hydrodynamic Lubrication," Journal of Lubrication Technology, Trans. ASME, Series F, Vol. 99, January 1977, p. 2.

15. Godet, M., and Berthe, D., "A More General Form of Reynolds Equation--Application to Rough Surfaces," Wear, 27(1973), pp. 345-357.

16. Elrod, H. G., "A General Theory for Laminar Lubrication with Reynolds Roughness," Report for Department of Machine Design, Technical University of Denmark, 1977.

17. Peklenik, J., "New Developments in Surface Characterization and Measurement by Means of Random Process Analysis," Proc. Instn. Mech. Engrs., Vol. 182, Part 3K, 1967-68, p. 108.

18. Patir, N., "Effects of Surface Roughness on Partial Film Lubrication Using an Average Flow Model Based on Numerical Simulation," Dissertation at Northwestern University, Evanston, Illinois, June 1978.

19. Castelli, V., and Pirvics, J., "Review of Numerical Methods in Gas Bearing Film Analysis," Journal of Lubrication Technology, Trans. ASME, Vol. 90, October 1968, p. 777.

20. Christensen, H., "Some Aspects of the Functional Influence of Surface Roughness in Lubrication," Wear, 17 (1971), pp. 149-162.

21. Tonder, K., "Lubrication of Surfaces Having Area Distributed Isotropic Roughness," Journal of Lubrication Technology, July 1977, pp. 323-330.

22. Lebeck, A. O., "Causes and Effects of Waviness in Mechanical Face Seals," Final Report, Technical Report ME-68(76)NSF-271-1, The University of New Mexico, College of Engineering, Bureau of Engineering Research, Albuquerque, New Mexico, January 1976.

23. Lebeck, A. O., "A Mixed Friction Hydrostatic Face Seal Model with Thermal Rotation and Wear," Accepted for publication in ASLE Transactions.

24. Lebeck, A. O., "A Mixed Friction Hydrostatic Face Seal Model with Phase Change," Submitted to the ASME Journal of Lubrication Technology for Review.

25. Orcutt, F. K., "An Investigation of the Operation and Failure of Mechanical Face Seals," presented at the Fourth International Conference on Fluid Sealing Held in Conjunction with the 24th ASLE Annual Meeting in Philadelphia, May 5-9, 1969, FICFS Preprint No. 22.

26. Lebeck, A. O., Teale, J. L., and Pierce, R. E., "Hydrodynamic Lubrication and Wear in Wavy Contacting Face Seals," presented at the 1977 ASLE-ASME Lubrication Conference, Kansas City, October 3-5, 1977, ASME Paper No. 77-LUB-18.

27. Lebeck, A. O., "A Study of Mixed Lubrication in Contacting Mechanical Face Seals," presented at the 4th Leeds-Lyon Symposium on Lubrication, September 1977, Lyon.

28. Pierce, R. E., "A Design Study for a Wavy Hydrodynamic Mechanical Face Seal," Master's Thesis, The University of New Mexico, Albuquerque, New Mexico, May 1978.

29. Teale, J. L., "Surface Roughness Effects in Hydrodynamic Lubrication," Master's Thesis, The University of New Mexico, Albuquerque, New Mexico, August 1978.

DISTRIBUTION LIST

Recipient	Number of Copies
Office of Naval Research 800 N. Quincy Street Arlington, Virginia 22217 Attn: M. Keith Ellingsworth, Code 473	(3)
Defense Documentation Center Building 5 Cameron Station Alexandria, Virginia 22314	(12)
Naval Research Laboratory 4555 Overlook Avenue Washington, D. C. 20390 Attn: Technical Information Division Code 2627 Code 2629 Dr. Ravner, Code 6170	 (6) (6) (1)
U. S. Naval Postgraduate School Monterey, California 93940 Attn: Dept. of Mechanical Engineering	
U. S. Naval Academy Annapolis, Maryland 21402 Attn: Dept. of Mechanical Engineering	(1)
Naval Air Systems Command Jefferson Plaza Washington, D. C. 20360 Attn: B. Poppert, Code 240E	(1)
Naval Sea Systems Command Crystal City, National Center #3 Washington, D. C. 20360 Attn: Code 033	(1)
Naval Ships Engineering Center Prince George's Center Hyattsville, Md. 20782 Attn: J. F. Dray, Code 6148D	(1)
Naval Ships R&D Center Annapolis, Md. 21402 Attn: Friction and Wear Branch	(1)
Naval Air Engineering Center Lakehurst, New Jersey 08733 Attn: Mr. P. Senholzi	(1)

DISTRIBUTION LIST (continued)

	Number of Copies
Naval Air Propulsion Test Center Trenton, New Jersey 08628 Attn: Mr. R. Valori	(1)
Naval Air Development Center Warminster, Pa. 18974 Attn: Mr. A. Conte	(1)
National Science Foundation 1800 G. Street, N. W. Washington, D. C. 20550 Attn: Dr. C. J. Astill	(1)
National Bureau of Standards Washington, D. C. 20234 Attn: Dr. W. Ruff	(1)
NASA Lewis Research Center 21000 Brookpark Road Cleveland, Ohio 44135 Attn: R. L. Johnson	(1)
Air Force Office of Scientific Research Washington, D. C. 20333 Attn: Directorate of Engineering Sciences	(1)
Air Force Aeropropulsion Laboratory Wright-Patterson Air Force Base Ohio 45433 Attn: AFAPL/POD-1, Dick Quigley, J.r	(1)
Army Research Office Durham, North Carolina 27706 Attn: Dr. E. A. Saibel	(1)
Office of Naval Research Branch Office 1030 East Green Street Pasadena, California 91106	(1)
Assistant Chief for Technology Office of Naval Research, Code 200 Arlington, Virginia	(1)
Prof. H. S. Cheng Department of Mechanical Engineering Northwestern University Evanston, Illinois	(1)

DISTRIBUTION LIST (continued)

Number of Copies

Crane Packing Company (1)
6400 Oakton Street
Morton Grove, Illinois 60053
Attn: Art Zobens

Sealol Inc. (1)
Box 2158
Providence, RI 02905
Attn: H. F. Greiner

Pure Carbon Company (1)
St. Marys, Pa. 15857
Attn: R. R. Paxton